Investigation of a Bio-Inspired Range finding Algorithm (BIRA) for Ultrasonic Imaging Systems

By

Frédéric DEVAUD

In the fulfillment of the requirement
for the degree of Doctor of Philosophy

Centre for Ultrasonic Engineering
Department of Electrical and Electronic Engineering
University of Strathclyde

Copyright

Declaration

I declare that this Thesis embodies my own research work and that it was composed by myself. Where appropriate, I have made acknowledgements to the work of others.

Frédéric DEVAUD

"There is no such uncertainty as a sure thing"

Robert Burns(1759-1796)

Acknowledgements

I would like to thank Professor Gordon Hayward for his guidance and supervision during my research. I have learnt considerably thanks to his experience and technical expertise. I am also very grateful for all his support.

I would also like to thank Professor John J. Soraghan for the interesting discussions about signal processing and all his support.

I would like to thank Doctor Gareth Pierce for his help to write this thesis.

I would also like to thank all the members of the CUE for their support and kindness.

To the people that I met in Glasgow, thank you for all the good time that I shared with you. Thank you to the Strathclyde Harriers club for changing my vision of running. A Special thanks to Alex, Amelie, Arek, Carlos, Eva, Farid, Jessica, Santi, Stefan and Walter. Another very special thanks to Clotilde for her support to finish this thesis.

Finally, I would like to thank my loving family for their continuous support throughout my time in Glasgow.

To my parents,
A mes parents,

Abstract

This thesis presents the results of the analysis of the bat auditory system and covers various aspect of bat behaviour of interest to the field of ultrasonic imaging. These small mammals use complex acoustic calls to navigate, identify and catch small flying prey, with apparent performance surpassing any current man-made systems. Therefore, the study of such mammals can introduce new concepts for ultrasonic imaging.

This thesis presents a review of the classification of bats by their acoustic emissions. It gives a detailed description of their acoustic calls and also provides information on the underlying processes involved in the bat auditory system. An analysis of the possible applications of the techniques used by the bats is done, in comparison with current ultrasonic technology.

The work describes various approaches to reproduce bat behaviour by giving a detailed description of the concepts and the modelling techniques used. A biologically inspired algorithm, Bio Inspired Range finding Algorithm (BIRA), is developed to mimic the underlying processes involved in the bat auditory system, when forming a detailed acoustic image. This algorithm is inspired from the analysis of previous bat auditory models one developed by Saillant et al. in 1993 named Spectrogram Correlation And Transformation receiver (SCAT) and another one from Matsuo et al in 2004. To fulfill the purpose of this thesis, BIRA is designed as a new way of forming images for ultrasonic systems.

For evaluating the performance of the BIRA in an environment similar to any engineering applications, an ultrasonic ranging system has also been designed. This system simulates the interactions between the source/receiver device, the medium of propagation and the target structure. It is used to quantify the axial resolution achieved by the BIRA.

In a realistic environment, the BIRA appears to be limited in achieving the resolution of the bats. The results presented in the thesis indicate that the techniques inspired from the bat auditory system, as implemented in the BIRA, do not lead to an improvement in axial resolution in a practical environment. BIRA works well on ideal signals, subject to zero noise and where the signal bandwidth is not constrained by environmental or source/receiver limitations. However when air attenuation is considered, the discrimination techniques used in BIRA fail. Moreover, other well-established techniques, used to enhance the axial resolution, perform better than the BIRA when multiple echoes are considered.

The results presented in this thesis question the way bats form an acoustic image and more specifically, the formation of a detailed range-profile image. The

results support the assumption that bats may have a simpler detection method, either based on the detection of the first echo or on the detection of other acoustic effects created by a flying insect, such as the wing flutter.

Table of Contents

List of Tables

List of Figures

List of Acronyms

1D One Dimensional

2D Two Dimensional

3D Three Dimensional

AC Auditory Cortex

ANN Artificial Neural Networks

BIRA Bio-Inspired Range finding Algorithm

CF Constant Frequency

CF-CF Constant Frequency - Constant Frequency

CF-FM Constant Frequency - Frequency Modulation

CT CricoThyroid

CN Cochlear Nucleus

CW Continuous Wave

DSCF Doppler Shifted Constant Frequency

FBW Fractional BandWidth

FFT Fast Fourier Transform

FM Frequency Modulation

FM-FM Frequency Modulation - Frequency Modulation

HRTF Head-Related Transfer Function

IC Inferior Colliculus

IID Interaural Intensity Difference

IIR Infinite Impulse Response

ITD Interaural Time Difference

IR Impulse Response

LFM Linear Frequency Modulation

LPM Linear Period Modulation

LSO Lateral Superior Olive

MGB Medial Geniculate Body

PW Pulsed Wave

WPS Wiener Pulse Shaping

TSW Two-Sided Wiener

LSO Lateral Superior Olive

NDE Non Destructive Evaluation

NDT Non Destructive Testing

RA Range Accuracy

SA Synthetic Aperture

SCAT Spectrogram Correlation And Transformation receiver

SONAR SOund NAvigation and Ranging

SNR Signal-to-Noise Ratio

SPL Sound Pressure Level

TA ThyroAryteroid

VLSI Very Large Scale Integration

WA Wavelength Accuracy

Chapter 1

Introduction

1.1 Biologically inspired system

The inspiration of new ideas can come from studies of the animal kingdom. The way they navigate, communicate and the analysis of their anatomy can provide relevant information to contribute to the knowledge of engineering. There are studies being done on animals such ants [Hickling and Brown, 2002], mice [Heffner and Koay, 2001], dolphins [Au, 2004] and bats [Popper and Fay, 1995]. Biologist, neurologists and engineers analyse their behaviour to improve current knowledge in their respective field [Dawson, 1991] [Fenton, 1984] [Suga, 1990] [Streicher et al., 2003].

The ultrasonic domain has a great interest in the study of animals that broadcast acoustic waves to accomplish their daily tasks, such as communicating or hunting for their prey. There is a wide range of animals that use acoustic waves, such as Dolphins for fish hunting [Dubrovsky, 2004], rats as a love-song [Holy and Guo, 2005], birds to communicate [Kroodsma, 1983] or bats to hunt for insects [Moss and Surlykke, 2001]. The characteristics of their acoustic signals vary largely, depending on the animal and the purpose of what they are trying to achieve. The performance that some of them can achieve, such as bats, for identifying their prey is often far above any current man-made acoustic system [Simmons et al., 1998]. The way bats perform such tasks is often unclear and constitutes the source of extensive research. The problem can be split in two main issues; the first one consists of understanding what they may use to accomplish their tasks, what type of information is available to them and what is valuable to them. The second issue for potential engineering applications relies on how to model their biological processing system and how relevant it is to the animal itself. This subject has been covered by a large range of scientists such as biologists, neurologists, signal processing, communications, etc... where each of them have their own approach of the problem to achieve a specific goal.

Focusing on the bat, biologists have analysed the evolution of bat signals in over 900 different species that emit different acoustic signals sometimes to accomplish the same task, i.e. catch an insect. Some other bats are fruit eaters. The insect hunter bats use ultrasound to detect and track the insects whereas the fruit eaters primarily use vision to recognise their food. The study of the bat auditory system has been done to understand how bats are processing the acoustic waves and what the role of each physical element plays in the bat auditory system, such as the cochlear, basilar membrane and the neural organisation. Despiste bats being studied for over two hundred years, it is still not clearly understood how their echolocation system works and how to design a bio-inspired bat. The challenge of this research project was to create and alternative imaging technique inspired from the study of bats.

1.2 Motivation

Mammals such as bats use ultrasonic signals to hunt for small flying insects with performances that no current man-made systems have been able to reproduce [Simmons et al., 1998]. By synchronising their flying path with their sound emissions, they can catch small flying prey in a cluttered environment, in a fast and accurate way.

The objective of the research presented in this thesis is to analyse the current knowledge of the bat echolocation system in order to understand the relationship between their acoustic emissions and the task that they achieve.

The goal is to harness the underlying processes occurring in the bat auditory system and to develop imaging techniques that would lead to an improvement in ultrasonic image quality. Various aspects of bat performance are of interest such as resolution, speed of processing or classification methods [Simmons et al., 1998] [Simmons, 1989] [Grunwald et al., 2005]. By using bat inspired techniques, the

goal is to improve the performance of current ultrasonic systems in terms of axial resolution, lateral resolution and robustness to noise.

The work focuses on developing an algorithm inspired from the underlying bat auditory processes to improve the axial resolution of current ultrasonic imaging system. The performance is then evaluated under conditions encountered in practical engineering applications and then compared to well-established processing techniques.

1.3 Original contributions of the thesis

A novel contribution of this work is in the creation of a bat inspired algorithm for enhancement of axial resolution. The Bio-Inspired Range finding Algorithm (BIRA) has been developed from knowledge of the bat auditory system, to improve the axial resolution and this has been demonstratred successfully on simulated, ideal data.

Secondly, the behaviour of the Bio-Inspired Range finding Algorithm (BIRA) has been evaluated under conditions typical of practical engineering applications. An ultrasonic ranging system has been designed to incorporate the influence of air attenuation, of the restriction in the bandwidth of the ultrasonic device and of the structure of the target. The influences of ultrasonic wave attenuation in air and the bandwidth limitation of the emitting/receiving transducer device have been quantified with regard to the performance of the algorithm. Limitations of the BIRA are then identified.

Finally and importantly, the underlying processes inspired from the bat auditory system that are implemented in the Bio-Inspired Range finding Algorithm (BIRA) are questioned to achieve the fine resolution of the bats. The simulations and results of this work provide information relating to the manner in which bats actually identify objects in their surroundings. Therefore the ability of bats to

form a fine detailed image is questioned, as the results presented in this thesis contradict that commonly held assumption.

1.4 Organisation of the thesis

Chapter 2 presents the different type of bats known in the animal kingdom. It provides information about their acoustic signals and the type of prey they hunt. Their echolocation methods are reviewed in detail and the brain structure is presented, along with the underlying processes. A parallel between the known processing involved in the bat auditory system and current techniques used in a large range of applications is also presented.

Chapter 3 introduces different types of computational models that have been developed to reproduce the task accomplished by bats in open-field conditions. It presents the contribution to the knowledge of the field and is the source of inspiration of this work. The Chapter then focuses on two models designed to enhance image resolution.

Chapter 4 includes the BIRA that has been developed to enhance image resolution. A detailed description of the algorithm is provided, with a parallel to the bat auditory system. Well-established techniques to improve image resolution are also presented.

Chapter 5 resumes the analysis of the BIRA when set to an environment relevant to engineering applications by evaluating robustness under idealistic operating conditions.

Chapter 6 describes an ultrasonic ranging system developed to evaluate the performance of the algorithm. It is a relevant system to one occurring in practical applications. The performance of the algorithm is also quantified.

Finally, Chapter 7 presents the conclusion of this work with recommendations for future work in the same field.

1.5 List of publications

During the course of the PhD degree, the following research papers have been published:

- Devaud, F.; Soraghan, J.J.; Hayward, G., *Evaluation of a "Bat Inspired" Ultrasonic Imaging System,* Presented at Workshop on Science, Technical Innovation and Applications in Bioacoustics, May 2004.

- Devaud, F.; Soraghan, J.J.; Hayward, G., *A bat inspired ultrasounds imaging to enhance axial resolution,* Proceedings of Institute for Communications and Signal Processing (ICSP) Colloquium, June 2004.

- Devaud, F.; Hayward, G.; Soraghan, J.J., *The use of chirp overlapping properties for improved target resolution in an ultrasonic ranging system,* Ultrasonics Symposium, 2004 IEEE, 23-27 August 2004, vol.3, pp. 2041-2044.

- Devaud, F.; Soraghan, J.J.; Hayward, G., *A comparison of non-adaptive deconvolution techniques for range resolution enhancement based on a model of a bat's auditory system,* Proceedings of Institute for Communications and Signal Processing (ICSP) Colloquium, October 2005.

- Devaud, F.; Hayward, G.; Soraghan, J.J., *Evaluation of a Bio Inspired Range finding Algorithm(BIRA),* Ultrasonics Symposium, 2006 IEEE , 3-6 October 2006.

- Devaud, F.; Hayward, G.; Soraghan, J.J., *Bio Inspired Range finding Algorithm (BIRA): Analysis, Requirement and Applicability,* Fourth International Conference on Bio-Acoutics, Institute of Acoustics, Loughborough University, 10-12 April 2007.

- Devaud, F.; Hayward, G.; Soraghan, J.J., *Investigation of a Bio Inspired Range finding Algorithm (BIRA),* IEEE Transactions on Ultrasonics, Ferroelectrics and Frequency Control, In Press.

Chapter 2

Acoustic properties of bats

2.1 Introduction

The ability of bats to orientate in the dark by employing complex sonic emissions has long held the fascination of scientists. In the absence of conventional interrogation, analysis of their echolocation system and the structure of their sonic emission may provide relevant information to understand the underlying processes that have evolved in this sophisticated creature. If properly harnessed, those underlying processes may benefit imaging systems such as static imaging (Non Destructive Testing (NDT), SOund NAvigation and Ranging (SONAR)) and biomedicine where the main image quality criteria are lateral and azimuthal resolution. It could also be of benefit to moving object imaging systems for detection purposes, or Doppler shift measurement systems.

This Chapter presents a description of the bat echolocation system. Firstly, a general introduction of the bat biological classification is performed. Then a description of the structure of their acoustic emissions is presented, alongside the echolocation techniques employed to catch their prey. Finally, a description of the auditory system organisation is presented with the objectives of describing the underlying processes to analyse the echoes.

2.2 Overview of bats

Bats are the second largest mammalian order, with over nine hundred species. There is a large variety, from the smallest, the bumblebee bat of Thailand, to the Giant flying foxes that live in Indonesia. Interest in these mammals started more than 200 years ago. The first experiments on bats were completed by *Lazaro Spallanzani* in 1793, who noticed the ability of a bat to orientate in the dark whereas a captive owl was helpless. This Italian scientist then created a set of experiments to understand why the bats were able to move in the dark. He demonstrated that bats with their eyes covered were still able to avoid obstacles.

However, if their ears were blocked, their orientation was seriously impaired. At this period of time, the bats were thought to be mute and insufficient technology left the problem unsolved. It was only in 1938 that Professor Griffin measured with state of the art instrumentation, the first bat's sonic emission [Griffin, 1958]. It was discovered that bats emit ultrasonic frequency sound waves and analyse the echoes to learn about their environment. The sonic emissions are used to build up a detailed image and identify the structure of the objects in their surroundings. Using those sonic emissions, they hunt for different types of food depending, on their geographical location, as bats are present in all the continents except Antarctica. The large family of bats has been classified into two main groups as presented in the following Section.

2.3 Classification of bats

Biologists have classified the mammal in the Chiroptera (meaning hand-wing) order. From this order, two sub-orders can be formed, the Megachiroptera (mega-bats) and the Microchiroptera (microbats) [Altringham, 1996] [Fenton, 1995]. Each order represents bats with similar morphology and type of food they eat.

2.3.1 Megachiroptera

They feed exclusively on fruit, flowers, nectar and pollen. Their morphology is generally larger than the microbats. For example, the *Pteropus giganteus* bat weights up to 1.5 kg and has a wingspan of nearly two metres. With some exceptions, those bats do not echolocate but rather use their large eyes for their orientation. Moreover, their small ears do not render them suitable for echolocation.

2.3.2 Microchiroptera

Microbats are usually of smaller constitution than megabats. They commonly posses large and complex ears that are dedicated to sound location. They are mostly insect eaters and use complex sonic emissions to catch their prey. The sonic emissions that they use to catch insects vary significantly from one species to another. Despite those differences, they all have a sophisticated processing capability. Their sound sensitivity even enables some of them to locate their prey by passive listening [Anderson and Racey, 1993]. The Microchiroptera, with their echolocation capabilities, represent an interesting source for the purpose of this research. Accordingly, a deeper description of this order is now presented.

2.4 Classification of bats by their acoustic emissions

The term echolocation is used when sound is emitted and the received echoes are interpreted to determine the direction and distance of an object. Bats emit a wide range of modulated signals that they use to echolocate. They have evolved in different geographical locations and their acoustic emissions are different. Microbats are classified in two major groups: Frequency Modulation (FM) and Constant Frequency - Frequency Modulation (CF-FM) bats.

2.4.1 FM bats

FM bats broadcast pulses composed of frequency modulated acoustic waves. The structure between each species can differ but they commonly use a sweep of frequency that is a variation of the instantaneous frequency over time. Bats transmit a downward frequency sweep, which is characterised by the highest frequency being broadcasted first, going down to the lowest frequency. Figure 2.1

illustrates the spectrogram of four different types of chirp signals emitted by FM bats (The recorded bat calls have been obtained from the Biosonar laboratory in the University of Bristol, UK). The chirps cover a frequency range from about 20 kHz up to 150 kHz with the presence of harmonic components. The nature of the chirp can vary from one species to another but it generally matches a "hyperbolic" shape in time. However Figure 2.1 (d) is closer to a "linear" shape. The use of a "hyperbolic" shaped signal was demonstrated to offer Doppler tolerance properties that suggested a hunting strategy for the bats [Masters et al., 1991] [Altes and Titlebaum, 1970]. By using chirp signals, bats have the advantages of sending more energy spread over the time and also covering a wider range of frequency. The maximum sound pressure of the bat's emission has been measured at 110 dB Sound Pressure Level (SPL) at a distance of 10 cm, which is equivalent to almost twice the human normal talking level at a 1 m distance (40-60 dB). The high level of energy is suitable to compensate for the high attenuation in air and the wide range of frequency can provide more information about the target. Even if the structure of the broadcasted signal is well-known, it is still not well understood how they process it. Furthermore, the duration of the pulses and the frequency content are changed depending on the distance to the prey. The signal is optimised to increase the probability of a successful catch. An interesting characteristic about FM bats is the evidence that they do not use the Doppler Effect to detect an insect but only measurement of range [Boonman et al., 2003]. The process by which they accomplish such a task is still unclear.

2.4.2 CF-FM bats

The second type of bat is the CF-FM. Those bats do not use a modulated sweep of frequency to orientate and hunt for insects in air, but instead they use a Constant Frequency (CF) signal combined with a short duration FM signal. Figure 2.2 illustrates the spectrogram of a CF-FM bat.

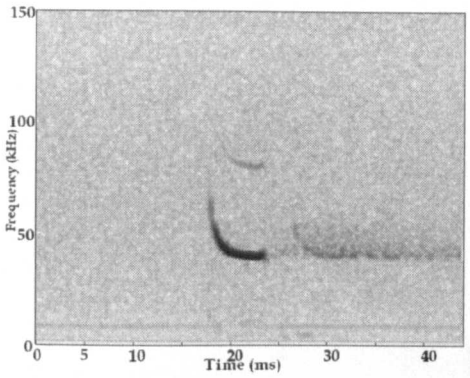

(a) *Pipistrellus pipistrellus*

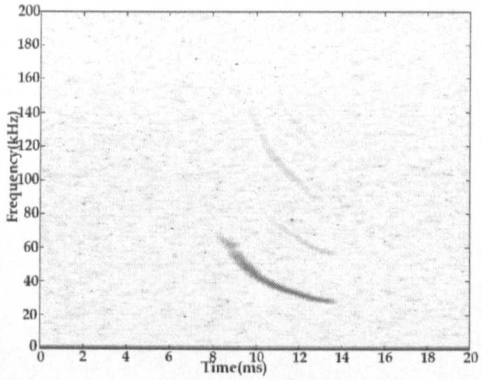

(b) *Eptesicus serotinus*

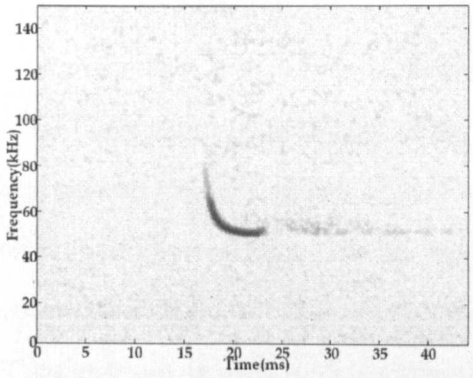

(c) *Pipistrellus nathusii*

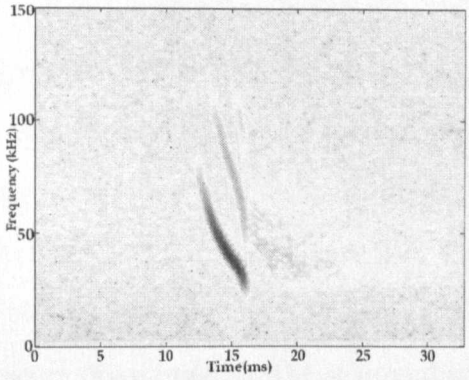

(d) *Myotis daubentonii*

Figure 2.1: Four spectrograms of FM bats.

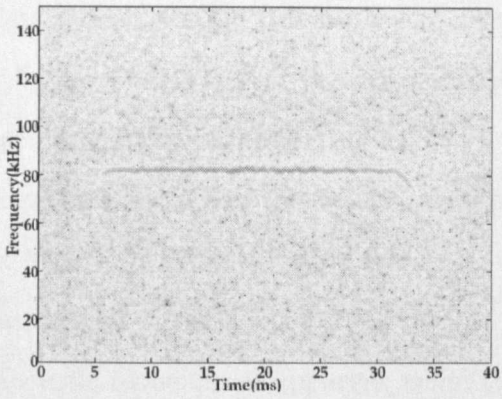

Figure 2.2: Spectrogram of *Rhinolophus ferrumequinum* CF bat.

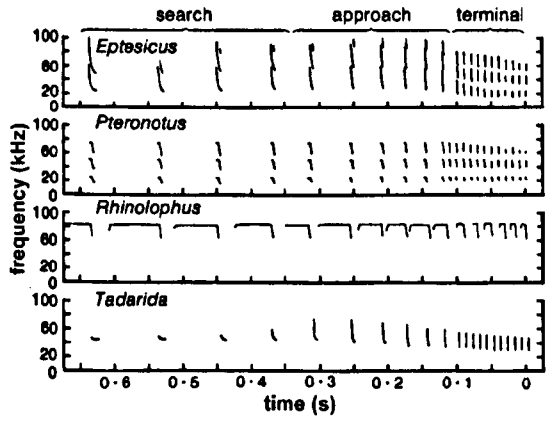

Figure 2.3: Illustrations of various echolocation signals of FM and CF-FM bats [Hill and Smith, 1984].

The constant frequency component is around 80 kHz with duration of almost 30 ms. The constant frequency of the CF bats can vary among the species, typically between 60 kHz and 80 kHz. The broadcasted signal also contains harmonic components however they do not appear on the illustration on Figure 2.2. The broadcasted signal also contains a short FM sweep at the end of the emission. The CF component is used to determine the presence of an insect in the surroundings whereas when the bat gets closer the period of the CF signal is reduced and the FM is used to determine the precise location of the prey. The CF component offers the advantage of concentrating the energy around a single frequency. This concentration of energy enables the bat to make use of the Doppler Effect in opposition to the FM bat. In fact, the bat has evolved to detect the Doppler Effect created by the wing flutter of the insect, their processing system has a really accurate Doppler measurement [Suga, 1990].

As for the FM bats, the structure of the emissions changes depending on the distance to the target. Figure 2.3 illustrates signals from four bats and the changes in the structure of the emitted pulse.

Variation of the acoustic emissions is apparent while the bat manoeuvres to intercept an insect and it can be analysed to understand their strategy of hunting.

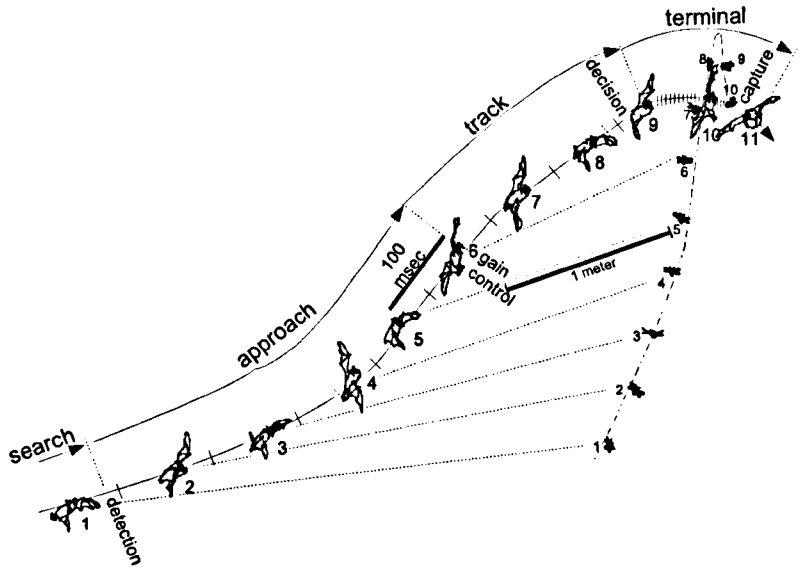

Figure 2.4: Interception manoeuvre by an echolocation bat [Simmons, 1989].

2.5 Temporal structure of the echolocation signals

FM bats make use of broadband frequency modulated signals to "form" an acoustic image. They regulate the rate of emission of their sonar according to the progressively declining distance to the target. Bats also change the characteristics of the signal that consequently modifies their perceived image. The adaptation of the signal is made to match the task to be achieved by the bats. When hunting, bats keep their head pointed at the target as it approaches, indicating that they are aware of the target's location [Simmons, 1989]. Figure 2.4 illustrates the path to catch the insect and shows the interception manoeuvre realised by a echolocation bat (*Epticiscus fuscus*) when aiming for a flying insect. It illustrates successive positions of the bat and the relative position of the flying insect. The position of the insect and the bat are indicated by the numbers. Figure 2.4 also shows the separation between the various steps in the hunting method of the bat. Figure

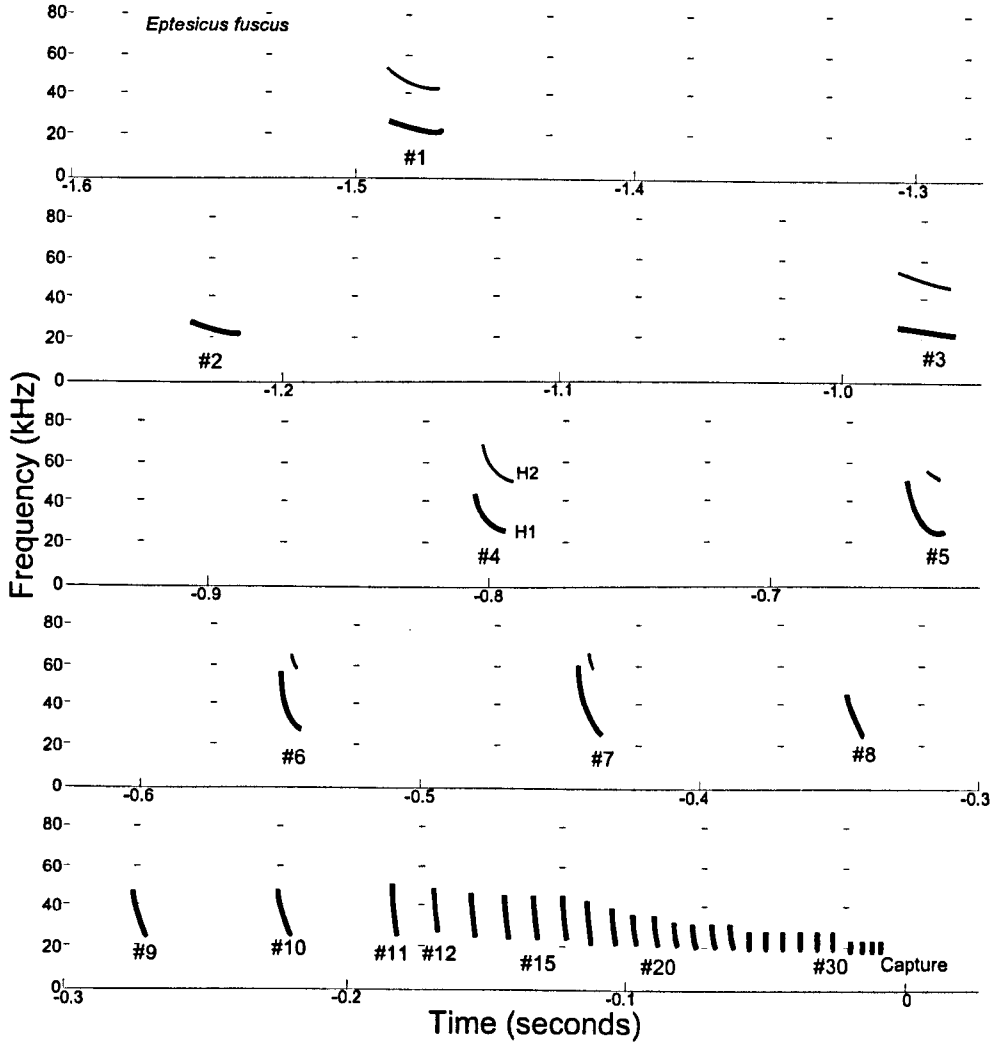

Figure 2.5: Spectrogram of sonar sounds emitted by the big brown bat, *Eptesicus fuscus* [Simmons, 1989].

2.5 shows the 34 numbered sounds corresponding to the FM bat recorded over a period of one and a half seconds. The time of emission of each sound is indicated by a tick along the path line of the flying bat in Figure 2.4. The emissions comprise a downward frequency sweep that are relatively brief and cover a frequency range from 20 kHz to over 60 kHz. The signals also contain harmonic components. The higher frequency components in Figure 2.5 are attenuated due to absorption in air. Figure 2.1 shows a better illustration of harmonic components in the bat signals. The stages in the bat sonar signature can be divided in four steps: search, approach, track and terminal. The characteristics of the signals differ in each step.

Firstly, the bat determines the presence of an insect. It is represented by the first three emissions in Figure 2.5. The signal is composed of a fundamental, sweeping from 28 kHz to 22 kHz and a harmonic sweeping from 56 kHz to 44 kHz. The rate of emission is roughly 5 to 10 repetitions per second. The distance from which a bat first reacts to a flying insect is a few meters.

After the bat has detected a target then the pursuit session starts. It is indicated by a significant change in the acoustic emissions, on Figure 2.5 it occurs between the emission numbers 3 and 4. In this step the bandwidths of the signals broaden considerably. The fundamental sweeps from 60 kHz down to 25 kHz and the harmonic from 100 kHz down to 50 kHz. By producing a wider range of frequencies, it is thought that bats receive richer information on the target as the emissions contain multiple wavelengths. When increasing the range of frequencies, bats can detect details of the target, in the case of the insect, the size of the insect and the wing beat [Kober and Schintzler, 1990]. Now the attention of the bat is focused on the target as the repetition rate of the sonar emission is progressively increased to a very fast rate, reaching up to 200/s when the bat is close to the target (Beginning with emission 11). The acoustic emission is shorter and the frequency bandwidth is increased. Finally, the bat reaches out at the last moment to size the insect in its wings or tail membrane. From multiple-flash

photographs, the bat appears to know the Three Dimensional (3D) position of the insect with an accuracy of about 1 to 2 cm. It is emphasised by the catch manoeuvre realised by the bat, consisting of surrounding the insect with its wings and tail membrane. The bat does not appear to require a greater accuracy to catch the isolated insect [Simmons, 1989].

The structure of the acoustic emissions of the bats is relatively well known. Then in order to understand how bats process the received echoes from their environment, studies of the bat auditory system have been conducted.

2.6 The bat auditory system

The bat auditory system is the heart of the bat signal processing machine. The acoustic waves returned back from the insect are successively transformed, to be interpreted by the bats. Firstly, the bats have to determine the location of the insect in 3D space. Therefore, principles of sound location will be introduced. Then, using experimental data on bats, the role of the ear and other key biological parts in the auditory system are presented. Finally, the pathway that arises in the auditory cortex is described along with the underlying processes involved.

2.6.1 Production of acoustic sounds

Echolocating bats, like other mammals, produce vocalizations with their larynx. The bat larynx is specialized to produce ultrasonic vocalizations for hunting small insects. Figure 2.6 illustrates the vocal organs of a bat. Those vocal organs are located at the cranial end of the trachea. The CricoThyroid (CT) muscle envelops the larynx, surrounded by the Thyroid and Cricoids cartilages. The vocal membranes are located on the vocal folds.

Ultrasound is produced by vibration of the vocal membranes in an expiratory air stream [Griffin, 1958]. The CT and the ThyroAryteroid (TA) control the

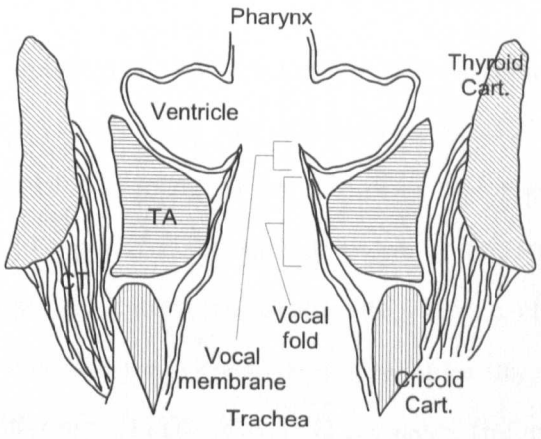

Figure 2.6: Schematic illustration of the anatomy of the vocal membrane [Mergell et al., 1999].

oscillations of the vocal membranes as they do not have internal muscles. They vibrate with the force exerted by the muscles. The vocal membranes can vary their angle of attachment to the rest of the vocal fold during phonation, acting as an independent oscillator. Their position and shape facilitate the production of non-linear phenomena such as harmonics [Mergell et al., 1999].

During vocalization, the CT determines the fundamental frequency and spectral properties of the sound by controlling the tension of the oscillating vocal membranes. The muscle control must be precisely coordinated with the timing of airflow through the vocal organ to generate appropriate sounds. The coordination has to be fast enough to generate the sound at a repetition rate up to around 200 Hz, as has been measured on some bats. For the broadcast of a sonar pulse, the CT tension is high at the beginning and declines during the course of the vocalization, to generate a downward frequency sweep [Suthers, 2004]. This cycle is repeated for each vocalisation fast enough to match the duration of the sound and keeping it in synchronisation with the air flow.

2.6.2 Binaural sound location and duplex theory

Sound location consists of determining the three dimensional location of an object, using the echo returned by the reflective object. Humans, bats and other mammals make use of two receivers to determine the coordinates of a source object, whereas bats use an adaptive, active source to determine the position of an object. Assuming a pure tone signal, the location of the sound source is provided by the use of two main cues: Interaural Intensity Difference (IID) and Interaural Time Difference (ITD). The ITD indicates the azimuthal position, in the horizontal plan of the bat, of the sound source by the difference in the time of arrival of the acoustic wave between the two receivers.

For a pure tone, the acoustic wave is perceived closer to the receiver at which it arrives first. The lateral coordinate is determined by the difference in phase between the two receivers. However, ITD has ambiguity when the wavelength of the tone is smaller than the distance between the two receivers. The phase difference is no longer only related to one wavelength but to multiples of the wavelength. In this case, the ITD does not correspond to a unique azimuth, as the auditory system may perceive a shorter ITD due to aliasing problems. Therefore the location of the sound source does not correspond to a unique spatial location. To avoid ambiguity, the location of the object is also determined by the IID as the difference in intensity is related to the distance to the object.

The relationship of perceived location does not vary linearly with IID alone, as there is a strong dependence on frequency in this case. However, for a given frequency, perceived azimuth does vary approximately linearly with the logarithm of the IID. By combining the use of ITD and IID, the azimuthal coordinate of an object can be determined. Evidence that bats use such cues has been validated in the bat auditory cortex as it possess neurons that are sensitive to ITD and IID [Simmons and Chen, 1989] [Matsuo et al., 2001].

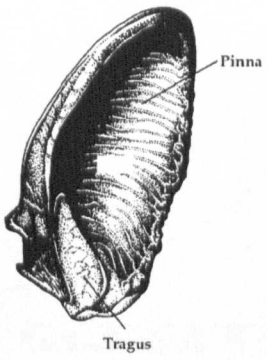

Figure 2.7: Illustration of the outer ear of a bat [Hill and Smith, 1984].

While the azimuthal coordinate is given by the ITD and IID, the elevation coordinate is indirectly determined by the shape of the external ear. The external ear can be interpreted as a filtering process dependent on the angle of incidence of the acoustic waves. The frequency content of the external ear varies with the elevation angle of the target [Wotton and Simmons, 2000]. Similarity with the human ear can be extrapolated, where the shape of the ear modifies the incident acoustic waves. The Tragus, which is the part in front of the ear opening as shown on Figure 2.7, has a crucial rule in the determination of the vertical location of a sound source. The external ear's transfer function varies within a restricted frequency range, from approximately 30 kHz for elevations of 40° below the horizontal to above 50 kHz for elevations around 40° above the horizontal. This transfer function combines the role of the tragus and other reflective parts in the external ear [Wotton et al., 1995]. In the frequency domain, the frequency spectrum has a frequency bin with a null magnitude. This specific frequency is named the notch frequency. Figure 2.8 illustrates the position of the notch frequency, i.e. where the magnitude is null, in relation to elevation angle.

The bat elevation resolution has been measured with experiments on the big brown bat *Eptesicus fuscus*. It was established that it was able to locate a sound source with a resolution of 1.5° in the azimuthal direction and about 3° in the

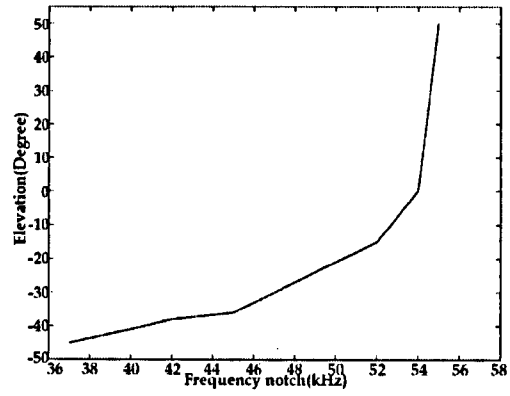

Figure 2.8: Notch frequency related to the elevation [Wotton et al., 1995].

elevation direction [Wotton et al., 1995]. After reaching the ear, the acoustic waves continue to progress in the bat auditory system. The acoustic waves altered by the ear transfer function travel in the ear canal to reach the inner ear and the cochlea where further processing takes place.

2.6.3 Cochlea

The cochlea is a spiral-like shell structure contained in the inner ear. It is the hearing sensor, transforming the acoustic waves to "electrical" signals. Those electrical signals can then be interpreted by higher levels in the auditory cortex. The cochlea is composed of a tissue membrane named the basilar membrane. It is a long membrane with the frequency sensitivity differing from one end to the other. This basilar membrane defines the frequency range sensitivity of the bat. Figure 2.9 illustrates the inner-ear.

2.6.4 Bat audiogram

The successive processes involved in the bat auditory system define the bat auditory sensitivity. Even if bats use broadband sound, they do not hear the frequency components with the same sensitivity. The Big Brown bat, *Eptisicus fuscus*, can not perceive frequencies above 100 kHz and below 4 kHz. The bat

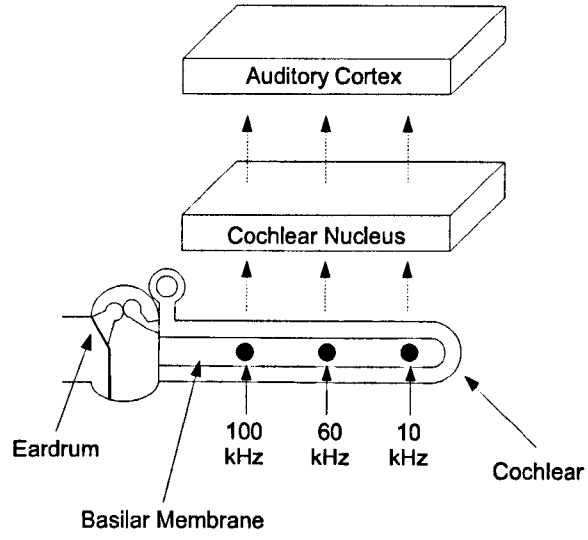

Figure 2.9: Illustration of the inner ear with the cochlea, basilar membrane and schematic of underlying processes [Suga, 1990].

appears to have the highest sensitivity at a frequency of 20 kHz. Figure 2.10 illustrates the audiogram of a FM bat *Eptisucus fuscus*. It shows the smallest wave pressure that the bat can perceive [Koay et al., 1997].

The audiogram shows that the bat has a non-constant auditory sensitivity. It is of interest when it is compared to the performance achieved by the bats in discrimination characteristics, where the bat appears to perform well with a limited auditory capability.

2.6.5 Pathways to the auditory cortex

The underlying processes involved in the bat auditory system can be analysed to understand how bats process the received echoes. The brain organisation of a CF-FM bat is presented in this Section. It describes the successive processing steps in the auditory system. The brain of the CF-FM bat has been extensively studied and the processes involved are better understood than for the FM bats. The way FM and CF-FM bats hunt for insects is significantly different. However

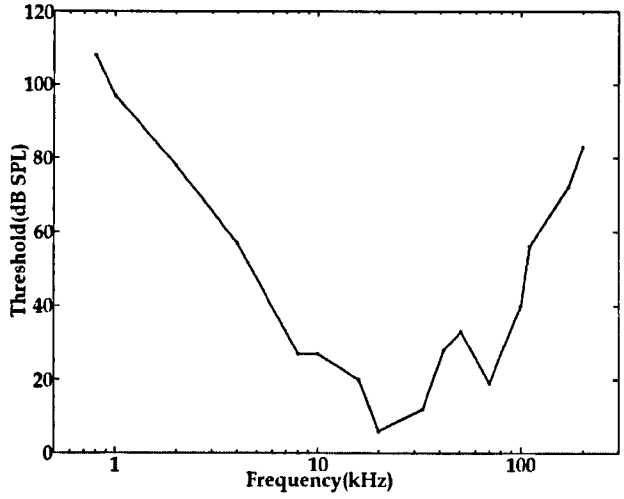

Figure 2.10: Audiogram of the Big Brown bat, *Eptisicus fuscus.*

there is similarity in the way they process the FM part of the echo.

The CF-FM bats use constant frequency sound to track for their prey. The constant frequency is appropriate to measure the Doppler Effect, as the energy is concentrated around a particular frequency. The detection method used by the CF-FM bat is based on the determination of the Doppler Effect. The returned echo from a flying insect is composed of a primary Doppler Effect due to the overall movement and a secondary Doppler Effect created by the wing flutter. The CF-FM bats have evolved to detect tiny Doppler frequency shifts created by the wing flutter.

The bat auditory system is specialised in processing the information contained in the acoustic waves that is progressively transformed from a pressure to electrical signals in the brain. For the bat to catch the insects, the vital information has to be preserved, such as the properties of the acoustic signal, i.e. amplitude, time and frequency, to increase the success of a catch.

The information presented next has been measured from a mustached bat, *Pteronotus parnellii.* That is, a CF-FM bat emitting long CF pulses lasting up to 30 ms followed by a short FM sweep lasting between 2 to 3 ms. The mustached

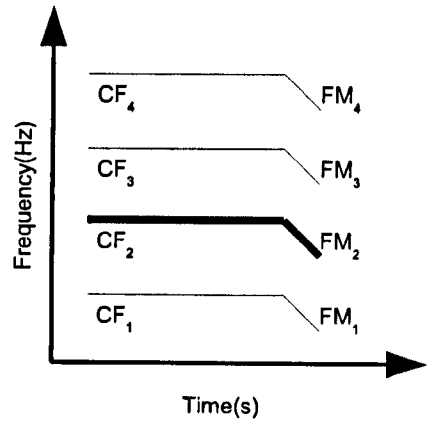

Figure 2.11: CF-FM bat acoustic emission.

bat broadcasts signals composed of four constant frequencies: CF_1, CF_2, CF_3 and CF_4 with a brief FM sweeps at the end FM_1, FM_2, FM_3 and FM_4. The frequency of the constant components are $CF_1 = 30$ kHz, $CF_2 = 59$ kHz, $CF_3 = 92$ kHz and $CF_4 = 122$ kHz. The main component of the bat emission is the CF_2 part as it is the strongest sound. Figure 2.11 illustrates the CF-FM acoustic emission spectra.

The steps in the decomposition of the acoustic waves in the bat auditory system can be divided as shown in Figure 2.12. The first neural signals are produced at the level of the cochlea. Then the first site of neuronal processing is done in the Cochlear Nucleus (CN) where it is structured to separate out components of the received echo. This one is composed of multiple harmonic components that are separated in the CN by amplitude and frequency selectivity. Then, the next step involves the Inferior Colliculus (IC), this part of the brain is split in two parts. One Section of the IC is dedicated to encode the FM signal-echo delay where neurons are frequency tuned to determine the delay time of the received echo. The second part of the IC is designed to encode the CF Doppler Effect where it is dedicated to the determination of the tiny Doppler Effect due to the wing beat. Next, the Medial Geniculate Body (MGB) is populated by Frequency Modulation

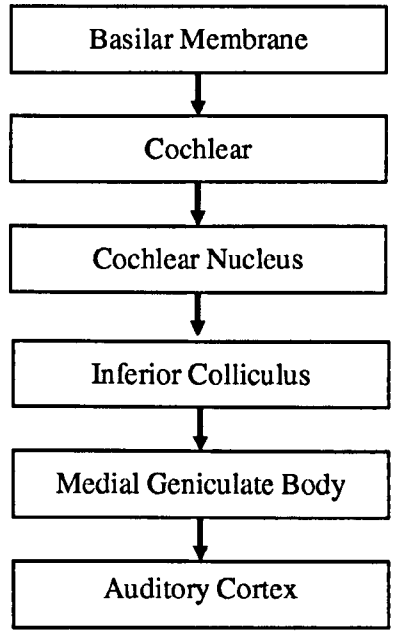

Figure 2.12: Auditory path.

- Frequency Modulation (FM-FM) neurons. These neurons are dedicated to determine the delay time of the received echo by using coincidence neurons between the broadcasted signal and the delayed return echo. The process can be modelled by a delay line on which a neuron fires when coincidence between the returned echo and the delayed bat emission occurs. The coincidence between the returned echo and the broadcasted emission is done with the use of the frequency tuned neurons from the IC. Figure 2.13 shows the brain organisation and the location of each part.

The mustached bat uses a long duration pulsed signal that overlaps with the returned echo. When the broadcasted sound hits a moving target, the returned echo is shifted in frequency. The bat detects the shift in frequency by comparison with its own emission. When a Doppler shift is detected, the bat compensates for the overall Doppler shift by lowering or increasing the frequency of its acoustic emission. The aim of it is to cancel out the overall Doppler Effect to determine tiny Doppler shifts due to the wing flutter, as those characterise an insect. The bat

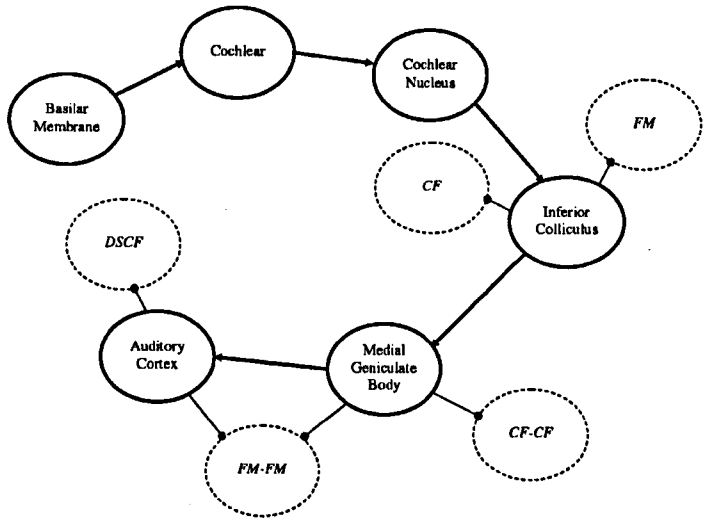

Figure 2.13: Auditory path and location of each processing unit.

aims to keep the returned echo in a range where it has best frequency sensitivity: its acoustic fovea (61 kHz to 61.5 kHz). The mustached bat has a dedicated system to process the acoustic waves around CF_2. It has been observed that the basilar membrane is more sensitive to frequencies between 61 and 61.5 kHz and it is designed to detect the tiny Doppler shift. Furthermore, there are much more neurons in a range between 61 kHz to 61.5 kHz. Those neurons are sharply tuned as they can detect frequency shifts as small as 0.01 % in this range (5 Hz) [Suga, 1990].

Measurements on a bat brain have shown that the different processing tasks are parcelled out among the several anatomically distinct areas of the auditory cortex. The major processing is realised in the Auditory Cortex (AC). It is composed of three major regions: Doppler Shifted Constant Frequency (DSCF), Constant Frequency - Constant Frequency (CF-CF) and FM-FM. Figures 2.14 and 2.15 show the regions for the bat's brain. The neurons in the DSCF are sharply tuned to a specific frequency and amplitude. It is dedicated to determine the frequency around CF_2 of the returned echo with a precision required to evaluate the tiny Doppler frequency shift from the wing flutter. This personalised region of the

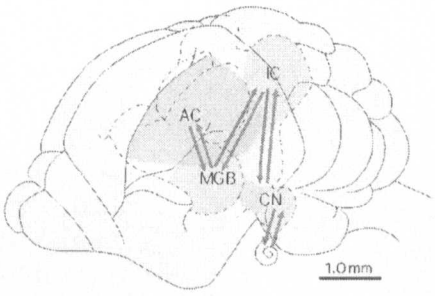

Figure 2.14: Brain of the bat [Suga and Ma, 2003].

brain represents a narrow frequency band from 60 to 62 kHz but it occupies 30 percent of the primary auditory cortex. This part is critical for the bat to catch its prey, if this region is altered the bat can not hunt for a flying prey. The sharply tuned frequency neuron response is obtained by a process called lateral inhibition, a mechanism in the sensory system by which inhibitory signals from adjacent neurons enhance the selectivity of a neuron to a particular stimulus. Figure 2.15 shows the location of the DSCF region in the brain. The neurons in the DSCF region are organised such that the frequency increases from the centre to the outer along a circular pathway: all the neurons equidistant to the centre respond to the same frequency. Then, the amplitude sensitivity varies along a perimeter of the same frequency. It is a frequency-amplitude representation of the received signal. The frequency range represented in the DSCF starts from 60.6 kHz up to 62.3 kHz. This range corresponds for a $CF_2 = 59$ kHz at speed varying from 4.2 m/s to 9.2 m/s. However it is known that CF-FM bats do compensate for the Doppler shift due to the overall movement of the prey. Assuming they fully compensate for the overall Doppler, the represented speeds can be shifted in a range from 0 m/s up to 5 m/s. As the frequency discrimination is of up to 5 Hz in the range between 61 kHz to 61.5 kHz, it corresponds to a precision in the speed measurement of 0.0414 m/s. The Doppler shift generated by the wing flutter, with a simplified model, has been calculated to be between 0.049 m/s and 0.196 m/s. The inherent precision that bats possess is sufficient to measure such a small Doppler Effect.

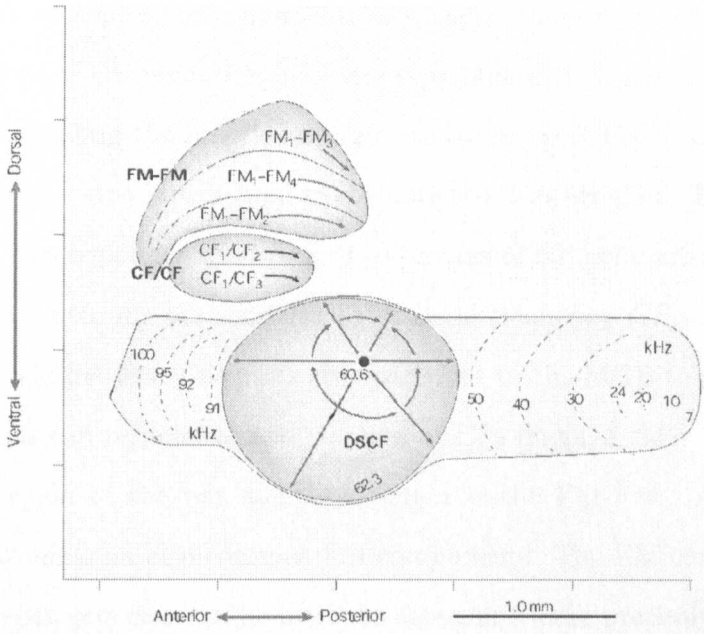

Figure 2.15: Organisation of the brain [Suga and Ma, 2003].

The performance of this wing flutter detection task is dependent on the way bats perform the overall Doppler compensation.

The region that compensates for the Doppler shift created by the overall bat movement is named the CF-CF area. This region analyses the frequency relation between the emitted signal and the received echo. Bats detect their own acoustic emission CF_1 and use it as a reference. When the bat receives an echo, it compares this reference with higher harmonics. As the broadcasted signal contains constant frequencies CF_2 and CF_3, there are two evaluations being done. The CF-CF is composed of two zones responding to different couples of CF: $CF_1 - CF_2$ and $CF_1 - CF_3$. There is no evidence of sensitivity to CF_4. Each neuron responds to a defined couple of CF. When only a CF tone is present, those neurons do not respond strongly, whereas if a pair of CF sounds is present, the neurons respond strongly - more than 6000 times stronger than for a single tone. The determination of the Doppler frequency shift is done by comparing the frequency shift introduced in the echo. There is a neuron dedicated for each frequency shift. Therefore each

frequency shift or neuron corresponds to a specific velocity. It was determined that within the CF-CF area, velocities are represented in a range from -2 m/s to $+9$ m/s. Regarding the functional organisation of the CF-CF area, it can be concluded that this area is dedicated to evaluate the Doppler shift. Those neurons are located in two regions in the brain. The process of CF comparison first arises in the IC where neurons are sensitive to a single frequency CF_1, CF_2 or CF_3. Then those single frequency neurons are connected to the MGB to be integrated so other neurons can respond to combination of CFs [Suga, 1984].

The last region of the bat auditory system is the FM-FM. As previously stated, the bat emission also contains FM components. The FM components are used when the bat gets close to the insect to determine more precisely its position. Similarly with the CF-CF region, those neurons are more sensitive to a pair of FM echoes than a single FM. FM-FM neurons compare the emitted pulse FM_1 with the delayed echo FM_2, FM_3 and FM_4. Each comparison of a couple is done in a distinctive region of the brain. The neurons are also tuned to a particular echo delay and echo amplitude. The organisation of the FM-FM region is designed for delay or range measurement. To determine the delay of the echo, when the bat hears its own emitted pulse FM_1, the neural response of it, is delayed as it travels toward the MGB. However, the returning echo is not delayed. The delayed response and the returning echo arrive at a particular neuron in the MGB and the coincidence of arrival causes the neuron to fire. The delay tune neurons are organised in a form of multiple delay lines forming an array of neurons. The majority of the delay line neurons are located in the IC with some in the MGB [Suga and Ma, 2003]. Figure 2.16 illustrates the principle of the delay line neurons in the MGB.

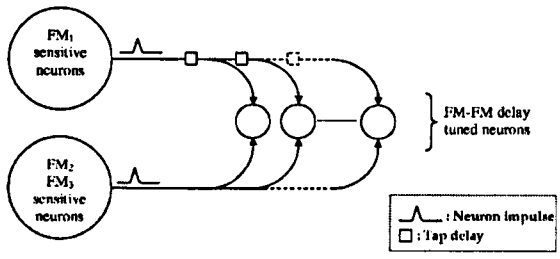

Figure 2.16: FM-FM delay sensitive neurons mechanism.

2.7 Resolution capabilities of bats

The resolution capabilities of the bats can be classified in three categories:

- Resolution using Doppler Effect.
- Resolution using the wing flutter.
- Resolution using the discrimination capabilities.

2.7.1 Doppler effect

It has been stated that CF bats can detect small Doppler changes contained in the backscatter echo. [Suga, 1990] realised a set of experiments on bats to quantify the smallest Doppler shift that a bat could perceive. It has been measured to be of 0.01 % of 500 Hz corresponding to a 5 Hz frequency shift. The complexity of the task consists of measuring such a small frequency shift when the emitter, i.e. the bat, is moving.

2.7.2 Wing flutter

The other aspects about the bats concern their ability to detect the flutter of the wings that are produced by a flying insect. They correspond to tiny changes in the returned echoes and may be used by bats to identify their prey. [Grossetete and Moss, 1998] realised a set of experiments to quantify the accuracy at which

the bats can determine the rate of the flutter of wings. The results show that bats can identify a wing rate of 50 Hz within ± 14 Hz and a 30 Hz wing rate within ± 9 Hz.

2.7.3 Discrimination capability

Another aspect about the bats resolution concern their ability to separate closely spaced overlapping echoes within a separation delay time smaller than any current man-made system. This resolution has been measured by experiments on *Epticiscus fuscus* conducted by [Simmons, 1989]. It shows that bats can discriminate echoes with a resolution of 2 μs in air. This time resolution corresponds to a resolution of 0.7 mm in space. When considering the shortest emitted wavelength this resolution corresponds to around $0.2 \times \lambda$.

2.8 Current system and links to bat behaviour

2.8.1 Doppler ultrasound

The bat properties mentioned previously could inspire new forms of acoustic imaging system. The first one concerns imaging of moving objects for detection or Doppler measurement. In medical imaging, Doppler ultrasound is used to image blow flow velocity. The conventional techniques used to measure the blood velocity are know as the Continuous Wave (CW) systems and the Pulsed Wave (PW) systems. The CW system consists of using a continuous wave and two receivers to measure changes in the wave related to velocity. Those types of system are limited in the Doppler frequency shift they can measure. It is often not possible to measure Doppler frequency shift with organs close to each other with different velocities such as arteries and veins [Krautkramer and Krautkramer, 1990]. In comparison with the CF bats, the adaptive system used to separate the overall

movement of the insect and the tiny movement due to the wings may offer an interest for measurement of Doppler Effect with CW systems. The bats are also of interest in Doppler ultrasound systems, the measurement are usually conducted with a fixed probe whereas the bats realise the same task in movement and they perform much better than any current systems.

The Doppler Effect can also be measured using a PW system. The approach consists of periodically broadcasting a short acoustic signal. The Doppler is measured by comparing the differences in successive emissions. The difference in phase provides information on the Doppler shift. The PW system is similar with the way FM bats hunt for insects in open air, as they periodically broadcast chirp signals. The FM bats extract, from successive broadcasts, information about the insect such as the size, the wing flutter and probably also the Doppler frequency shift. FM bats can discriminate insects with different wingbeat frequencies and patterns [Kober and Schintzler, 1990]. Bats might have to integrate such information across multiple, sequential echoes as the broadcasted pulses are too short to register the period of the wingbeat of most insects [Feng et al., 1994] [Bell and Fenton, 1984] [Anderson and Racey, 1993]. The processes by which they achieve such a task is not clearly understood and could have applications in evaluation of Doppler shift by detecting small differences in phase.

2.8.2 Bio-Medical Imaging Applications

The quality of imaging by ultrasound in some applications is highly dependent on the structure and nature of the organs or objects being imaged. An improvement in the image quality may be obtained with a prior knowledge of the structure being imaged. In medical imaging, such as skin imaging, the structure of the skin is composed of tissue with almost similar acoustic properties. Separating the different tissues is not straightforward as the variations in the returned echo are small. FM bats have been thought to form detailed images of their sur-

roundings [Simmons, 1989][Simmons, 1973]. An insect is a complex object that returns an echo composed of closely spaced elements with almost similar signal strength. If it is possible to harness how bats accomplish such a process, it may have applications in any systems where it is required to separate closely located elements. Moreover, the imaging techniques are more complex when the scattering dimension of the object being analysed is smaller than the wavelength.

2.8.3 NDT Applications

NDT is used in a wide range of applications, for detecting defects in objects and structures, in food monitoring or evaluation of particle concentrations. In the case of material inspections, current NDT techniques are difficult to use on rough or irregular shapes. Almost all NDT techniques work better to detect defects in homogeneous material [Krautkramer and Krautkramer, 1990].

Bats can identify objects in their surroundings by using their acoustic emissions. The object is commonly characterised by its Impulse Response (IR). The extraordinary object-recognition capabilities of bats has been demonstrated by experiments [Grunwald et al., 2005]. They can recognise an object by its roughness and discriminate between a leaf, a tree or an insect. To succeed in their hunt, bats may only require information about the shape of the object and not a detailed image. The shape has then to be recognised when different objects are located around it. Bats have developed a object-recognition system that could lead to improvement in fields of research such as object classification. Other applications could be in the domain of imaging with surface imaging to evaluate roughness of a material [Dror et al., 1995] [Schmidt, 1992].

The FM bats broadcast a frequency modulated signal, usually termed a chirp. The structure such as the period, the frequency bandwidth and the shape change over the time depending on the task to be achieved. Understanding why they use this type of signal could lead to alternative techniques for imaging. For example,

some FM bats use non-linear chirp signals that may have a Doppler tolerance property. Applications where Doppler Effect has to be avoided could use similar chirp signals. The Doppler tolerance property of the bat's non-linear chirp signal consists of a more accurate determination of the range of an object when considering a moving target. When using a Linear Frequency Modulation (LFM) chirp signal to measure the range of a moving target, the measured range is biased by a factor related to the speed of the object. However when using bat's non-linear chirp signal, the bias in the range measurement is less important, indicating more accurately the actual range of the object. Mathematical models of frequency modulated chirp signals have been designed to match the one measured on bats [Boonman et al., 2003].

Finally, the FM bats broadcast several sounds before catching the prey. It can be speculated that they combine the successive broadcasts to increase the probability of success. Understanding what information the bat is identifying between the successive sounds could improve imaging quality in techniques such as Synthetic Aperture (SA) processing.

2.9 Conclusion

Bats represent a large order of mammals that have significant physical differences. They eat a wide range of food from fruits to insects. Some of the bats use vision to hunt for food whereas others employ complex ultrasonic emissions. The bat auditory system has evolved to interpret acoustic waves required by a bat to hunt for an insect. The adaptive Doppler compensation method used by the bat, combined with the accurate Doppler measurement, enable the bat to track a flying insect. By combining the use of CF and FM, those bats use a complex dual system where each system is used for its best purpose, i.e. CF for Doppler shift and FM for range and final catch.

This Chapter has shown the organisation of the bat auditory system by listing the processes involved and the organisation between each dedicated region. The auditory system is organised in a sequential structure with, some distributed tasks along each region. Even if the acoustic characteristics and some of the processing are known, the problem remains complex. The aim of this research is to understand the underlying processes in order to achieve similar performance in engineering applications.

Chapter 3

Computational bat auditory models

3.1 Introduction

Reproducing the tasks achieved by bats has been approached with computational models of the bat auditory system, where each model reproduces a specific task of the bat observed in the field or in a laboratory.

This Chapter presents a review of the computational bat auditory models, discussing the purpose of their development. Firstly a general review of the models is done. Then, the Chapter focuses on two computational models designed to enhance axial resolution, including a detailed description of the underlying processes.

3.2 Bat modelling

Modelling the underlying processes of the bat has been the focus of previous research work . Computational models aim to analyse the processes involved when the bats catch a flying prey. Usually each model considers a simplified context to reduce the computation cost but still keeps relevant parameters to validate the process being evaluated. The models presented have been classified in four categories as illustrated in Figure 3.1. The first group represents the sensorimotor models where the aim is to reproduce the flying path of the bat in the task of catching an insect. Then the neuromorphic approach consists of modelling the neuron processes in the bat auditory system with programmable electronic components to form bat-like acoustic image. The following group contains the design of the underlying processes involved in the bat auditory system. Finally the last group concerns models where the aim is to reproduce the processes of the bat to identify its target by separating multiple closely spaced echoes.

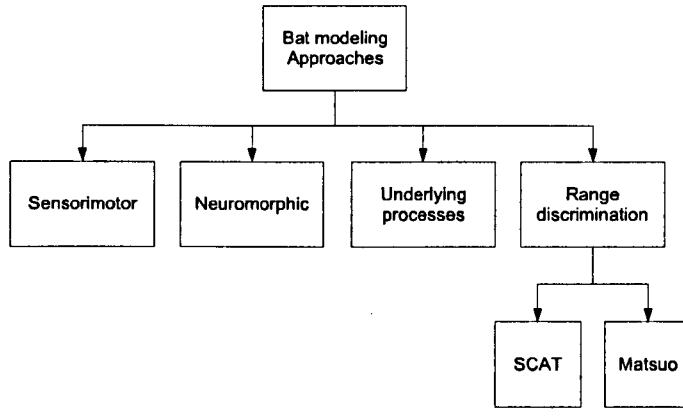

Figure 3.1: Classification of bat modeling approaches.

3.2.1 Sensorimotor

Sensorimotor models are designed to model the bat movement in hunting for small flying insects. The models presented in this Section incorporate acoustics, signal processing and control theory to illustrate the fundamental issues in accomplishing prey capture with echolocation.

The first model was developed by [Kuc, 1994] to better understand the sensorimotor processes in prey capture by echolocating bats. He simulated a call consisting of a 25 kHz fundamental and a single 50 kHz overtone and used a straight forward model of the beam pattern in conjunction with a model of the effect of the bat's ear and head. The model did not perform complete localization as only azimuth and elevation were determined. The control of the bat flight path was incorporated by using a simple homing strategy. Localisation of the target was achieved by measuring the difference between the return intensities in the fundamental tone at the two ears. For the elevation the difference in intensity of the overtone was used. Aerodynamics were simplified, with the model bat flying at a constant speed, without banking, and with an unlimited turn rate.

Kuc's model bat captured targets using simple homing based on azimuth and elevation, and he showed that simple intensity difference and frequency differ-

ence measurements in each ear at 25 and 50 kHz were sufficient to support this. His model was successful for slow moving targets, but his assumptions did not reproduce the more complex manoeuvres observed in natural insect capture on echolocating bats. The bat sensorimotor model describes the acoustic cues that are useful for prey capture and proposed a memoryless strategy employing only the fundamental and overtone components. This model looked at the basic elements in sonar using only first-order model, possibly employed by primitive bats. However, this was somewhat offset regarding the complexity of the objects being imaged by the bats and comparing it to the diversity and number of neurons that process auditory information. Bats have probably evolved with an echo processor that compensates for absorption, Doppler and prey reflection characteristics, suggesting that a simple hunting strategy was sufficient and that the key to the bat's performance is in all of these compensation techniques.

Following the work of *Kuc*, *Erwin* [Erwin et al., 2001] developed a more advanced sensorimotor model. The aim was to produce model trajectories replicating those observed in behavioural insect capture trials. The model was designed to determine the 3D localization of a flying insect. The range was evaluated from the echo delay, the azimuth on the relative intensity of the echo at the two ears, and the elevation on the spectral pattern of the sonar return in a match/mismatch process. The match/mismatch process consisted of comparing the received echo with a set of predetermined patterns recorded at known elevation. The set was compared with the returned echo to find the best match and the corresponding elevation. This model incorporated the propagation of acoustic waves using the sonar equation [Erwin et al., 2001]. These equations were used to determine the attenuation due to the medium in the frequency range of the bat signal. They also incorporated the noise influence and influence of the directivity of the pinna, the major element of the bat's ear that affects the acoustic wave. The model also added biological realism by restricting the bat angle of turn with the one observed

on the bat. The speed of flight was not considered as constant but varied with the strategy adopted to catch the insect. Two planning processes were considered, one with an anticipatory internal simulation and one with simple homing. The strategy used to catch an insect started with simple homing. Then, if the target was missed, the model tightened its turn by slowing. If this succeeded in setting up a capture, then the bat would follow a tight circle around the insect. In the final approach, if again the capture failed by circling around the insect, then the bat model moved away and started the whole strategy all over again.

Introducing a more advanced aerodynamic model provides information of the rule of aerodynamic constraints in defining target capture behaviour. This model showed that the direct homing capture strategy does not appear to be the preferred strategy and they also suggest a memory strategy that was not present in [Kuc, 1993]. The predictive strategy creates a flight path closer to the one observed in bats, as bats turn around the target even if the purpose of such manoeuvre remains unclear. It was suggested that it could be linked to target identification, aerodynamics (the bat can not turn fast enough or slow down fast enough) or reaction time.

Those computational models were designed to get a better understanding of the bat processes to hunt for an insect as a whole. They suggested some processing and control methods that may be used by bats to track for a flying insect.

3.2.2 Neuromorphic

Mimicking the behaviour of the bat neuro-processing system was also approached using neuromorphic modelling, based on Very Large Scale Integration (VLSI) [Horiuchi, 2005]. The underlying processes involved in the bat auditory system have been modelled with analogue and digital circuits that mirror neural algorithms in both signal representation and morphology. The massively parallel signal processing known to occur in neural structures like the cochlea, the au-

ditory midbrain, the cortex and other sensorimotor structures are modelled in order to be perform on a single chip, with all of the tasks having to be achieved in real time. The challenge in these models is to build devices with useful neural modelling tools with the speed of computation and the small physical size met in the bat auditory system. The VLSI models the inverse Head-Related Transfer Function (HRTF) of the bat, corresponding to the acoustic changes occuring in the ear, but also various types of neurons such as Lateral Superior Olive (LSO) neurons for sound strength and sound direction and range-tuned neurons. Those neurons' responses are then combined to create a Two Dimensional (2D) image [Horiuchi and Hynna, 2001] [Cheely and Horiuchi, 2003] [Shi and Horiuchi, 2004] [Shi and Horiuchi, 2005]. By using biologically inspired techniques, they have developed algorithms used for controlling robots to navigate and avoid obstacles. A "batmobile" has been designed that make use of this technologies to navigate in a forest of cardboard tubes without slowing down.

3.2.3 Bat underlying processes

Modelling the signal used by the bats can also enhance the information perceived about the surroundings. With a bat like chirp signal and a dual receiver system, it was shown that chirp signal is more suitable for the detection of small obstacles [Ifukube et al., 1991]. Other uses of bat inspired methods lead to innovative technologies to detect and classify mines in sonar systems [Reese and Kenney, 1994] that overcome the environment limits. Most of the biological models reproduce some function of the bat auditory system. The cross-correlation process supposedly done by the neurons of the bat [Lin et al., 1991] has been modelled by using a neural network. It was shown to be capable of determining the time of arrival of an echo and its strength. Other models utilise delay tuned neurons as identified in the bat auditory system, combining a wideband transducer and neural network to determine the time of arrival of echoes [Fiorillo and D'Angelo,

2002]. Analysing the rule of the processing of the inner ear and the way of modelling it in order to understand the rule of the different filtering processes was studed by [Chittajallu et al., 1994]. More complex models of operation were also developed to mimic other elements in the ear, such as the cochlea, by the use of Artificial Neural Networks (ANN), to provide a measurement of Doppler effect or reducing the perturbation introduced by the movement of the object [Inoue et al., 1999] [Carmena and Hallam, 2000]. Finally, other research focusses on modelling the effect of the ear transfer function [Kuc, 1993] [Kuc, 1997] [Peremans et al., 1998] [Horiuchi and Hynna, 2001] [Muller, 2001] [Peremans and Muller, 2003].

3.2.4 Range discrimination

The models presented in this Section are centred on the enhancement of axial or range resolution that the bat appears to possess. The model developed by [Saillant et al., 1993], named Spectrogram Correlation And Transformation receiver (SCAT), was designed to reproduce jitter experiments done on bats to measure the range resolution [Simmons et al., 1998]. The jitter experiment consists of an object moving back and forward along the range axis. The design is based on knowledge of the bat auditory system and reproduces the known underlying processes. The model input is a sum of overlapping chirp signals and is processed to determine the time of arrival of each individual chirp. It shows how the range resolution measured on bats can be achieved with the use of signal processing tools. The core of the model is based on parallel pathways, inspired from the cochlear decomposition occurring in the ear. It combines temporal and spectral information to analyse the signal to form detailed images.

Matsuo et al have designed a number of computational models, some for object localisation [Matsuo et al., 2001] [Matsuo and Yano, 2004] and others for discrimination of multiple objects [Matsuo et al., 2004]. It is also based on parallel pathways to combine temporal and frequency information, to form detailed

images as thought to be implemented in bats. It proposes alternative ways to separate multiple echoes when compare to standard techniques.

This Chapter presents later the computational models from [Saillant et al., 1993] and [Matsuo et al., 2004], as they represent the most interesting computational models for the purpose of this thesis. The techniques employed in these models are described in detail with the methods leading to enhanced resolution capability.

3.3 Models for axial resolution enhancement

The purpose of this Section is to provide a thorough analysis of the models that have been developed to reproduce the enhanced discrimination abilities of bats. The purpose is to extract the techniques that lead to the improvement in resolution. Firstly, the model developed by [Saillant et al., 1993] is presented with a detailed description. It is then followed by the model from [Matsuo et al., 2004].

3.3.1 SCAT model

The SCAT models the sonar receiver in the big brown bat (*Eptesicus fuscus*). Experimental results show that bats have a great ability to measure time delay difference between multiple overlapping echoes with a precision of down to 2 μs [Simmons et al., 1998]. This corresponds to approximately 0.7 mm in air. When considering the shortest wavelength in the chirp signal, it corresponds to a resolution of around 0.2λ. In favourable conditions, the bats can perceive a time-delay difference of up to 10 nanoseconds [Simmons, 1989]. The returned signal of a small prey species to the bat is composed of the sum of close overlapping echoes containing relevant information about the shape and size of the insect. The target shape can be described by the location of the reflecting points and surfaces, or glints, along the axis distance [Miller and Pedersen, 1988]. The fundamental

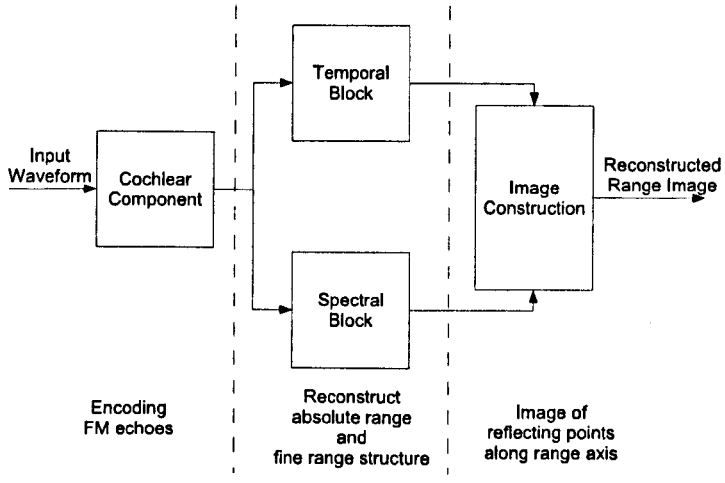

Figure 3.2: Diagram of the SCAT model.

technique is based on overlapping echoes that interfere with each other, reinforcing or cancelling amplitudes at different time and frequencies. The SCAT model proposes a receiver that combines time and frequency domain information. Those two domains of information are then combined to construct a fine image in the time domain.

3.3.1.1 Organisation of the model

The SCAT model is made up of three blocks: Cochlear, Temporal block and Spectral block. The Cochlear block processes the signal in parallel frequency channels as a first approximation of the biological cochlea. It is composed of a bank of filters that model the basilar membrane, followed by a neuron processing step. The Temporal block derives an estimate of the time of arrival of a group of overlapping echoes from the timing information returned by the Cochlear block. Finally, the Spectral block derives the time of arrival of each following echo. The final signal representation is built up by combining the Temporal and Spectral block timing information. Figure 3.2 illustrates the organisation of the model.

3.3.1.2 The Cochlear block

This block encodes the signal in a spectrogram like representation as it is done in the inner ear of the bat. It is composed of a filterbank (81 bandpass filters), a set of half-wave rectifiers and a low-pass filtering stage. The bandpass filters are tenth order Butterworth Infinite Impulse Response (IIR), with a constant 4 kHz bandwidth (3dB bandwidth). The filters have a centre frequency ranging from 20 to 100 kHz following a Linear Period Modulation (LPM) scale, i.e. the centre periods of the bandpass filters are linearly spaced, similar to the spacing of neurons in the bat's brain. The integration time of each filter is 350 μs in the range of the one measured on the bat *Eptesicus fuscus* (300 to 350 μs [Simmons and Chen, 1989]). In the SCAT model, the use of constant filter bandwidth distributes the quality factor from Q = 5 at 20 kHz up to Q = 20 at 100 kHz, that corresponds also to the range measured on bats. Then, the outputs of the filters are half-wave rectified and low-pass filtered. The low-pass filters are first order Butterworth IIR with a 3 kHz cut-off frequency and is equivalent of an envelope-smoothing process.

The biological parallel with the bat's ear is made with the filterbank as it models the basilar membrane in the inner-ear of the bat. The half-wave rectifier and the low-pass filters model processes performed by the excitation of hair cells and primary auditory neurons. Figure 3.3 shows a diagram of the Cochlear block. Figure 3.4 illustrates the signals at the different steps in the processing. Figure 3.4(a) illustrates an output of the filterbank. Figure 3.4(b) is the half-wave rectified signal. The signal obtained from the low-pass filter is also in Figure 3.4(c).

The last transformation in the Cochlear block is realised from the outputs of the low-pass filters. They are used to trigger "events" in each frequency channel, corresponding to discharges evoked in the auditory system. In mammals,

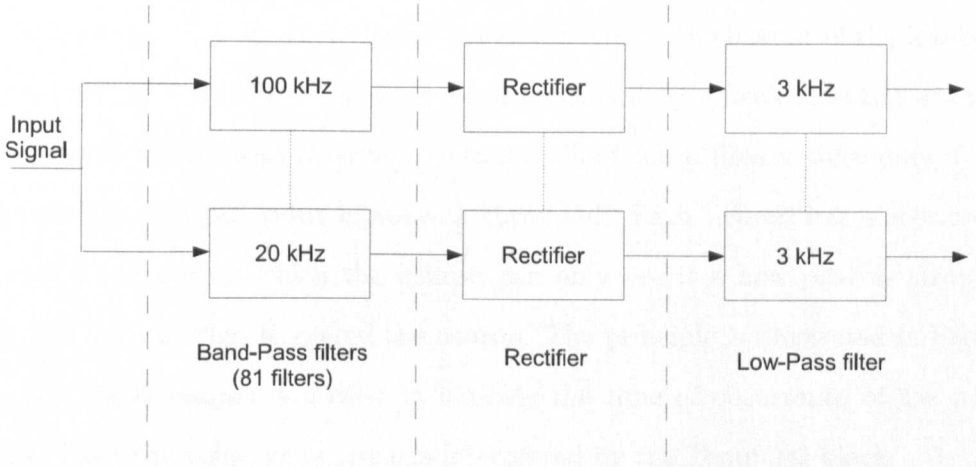

Figure 3.3: Diagram of the Cochlear block.

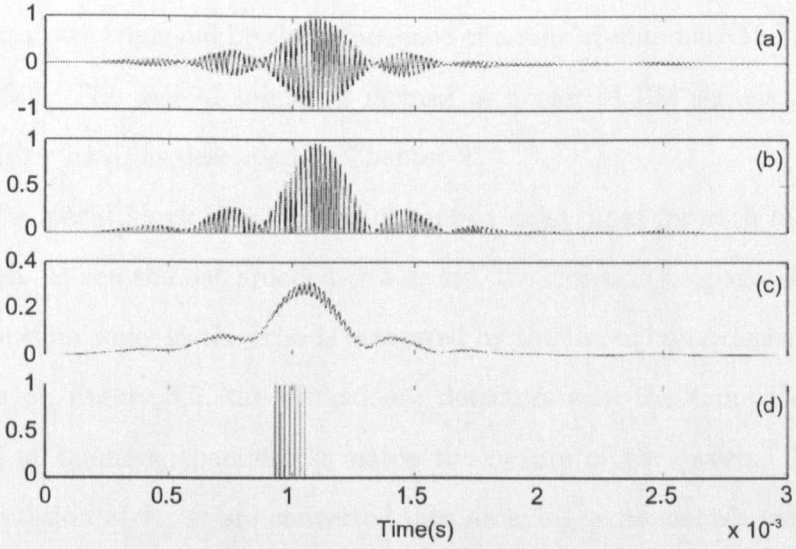

Figure 3.4: The outputs of different points in the Cochlear block. **(a):** Filter-bank outputs. **(b):** Half-wave rectifier. **(c):** Low-pass filter. **(d):** Peak-Neuron detection signal.

auditory-nerve discharges are pulses that convey information from the inner ear to higher levels in the auditory system. To represent theses discharges, the SCAT model employs 1 μs duration digital pulses converting the output of the low-pass filters into pulse patterns. The conversion is realised by a peak-detection conversion process named *peak-detection* neurons. The neuron fires a pulse only if the low-pass filter output value is above a threshold. Each neuron has a refractory time of 1 ms during which the neuron can only fire if a new peak is stronger than the last one that triggered the neuron. The principle is illustrated in Figure 3.4(d). These neurons are used to indicate the time of occurrence of the peak value. Then the volley of neurons is interpreted by the Temporal block.

3.3.1.3 The Temporal block

The Temporal block measures the time that elapses between the sonar emission and the echoes from the pulses generated by the outputs of the Cochlear block. The physiological basis of this block is the existence in the bat's auditory system of neurons that are triggered by the occurrence of a pair of sounds: FM-FM neurons [Suga, 1990]. The pair of sounds is defined as a pair of FM signals, e.g. FM_1, FM_2, FM_3 or FM_4, as described in Chapter 2.

The Temporal block is composed of tapped delay lines for each output from the cochlea. When the bat broadcasts a sound, the emission propagates along the lines. The time delay to the echo is measured by the use of coincidence detectors. As shown on Figure 3.5, the coincidence detectors sum the tapped delay lines occurring at different channels to match the nature of the sweep. The neural pulses (duration of 1 μs) are converted into decaying exponentials with variable time constant before the summation is performed. This is to reproduce a signal similar to the one measured on the bat neurons. Then, the neural activities are summed and compared to a threshold. If the sum of both the transmission channel and the echo channel exceed a threshold, then the neuron fires to indicate the time

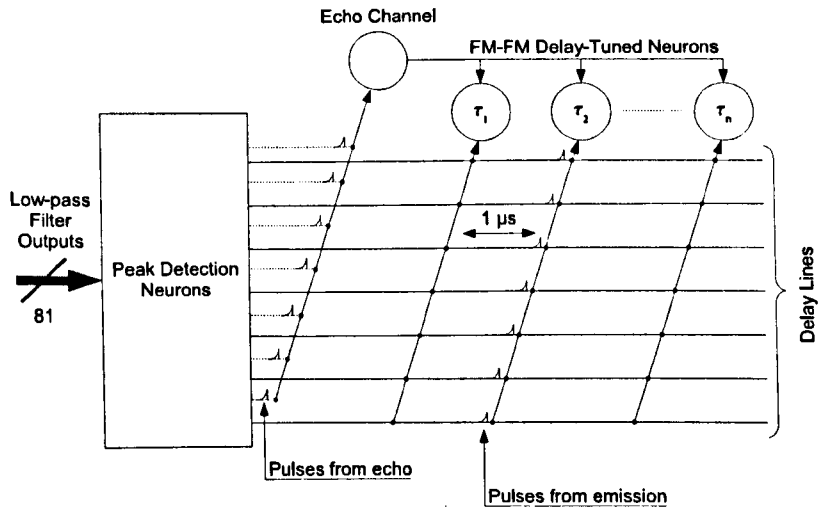

Figure 3.5: Architecture of the Temporal block.

delay. Figure 3.5 shows the structure of the Temporal block.

Figure 3.6(b) illustrates the volley of neurons generated by the peak neuron detectors. It shows the peak neurons firing when excited by a single chirp signal. Each frequency channel indicates an estimate of the time of occurrence of the frequencies contained in the chirp signal. The result from the sum of the neurons is shown on Figure 3.6(c).

3.3.1.4 The Spectral block

The temporal resolution is limited by the time of integration of the filters (350 μs). Therefore a fine resolution is obtained with the Spectral block. While the Temporal block determine the time of arrival of the first element in the input signal, the Spectral block is designed to detect the delay of any following sequences. To achieve the fine delay resolution, the Spectral block uses the presence of peaks and notches in the frequency spectrum. It is believed that bats use a "similar" voting mechanism to reconstruct the target's shape [Saillant et al., 1993]. The time of arrival determined by the Spectral block is then added to the time of the

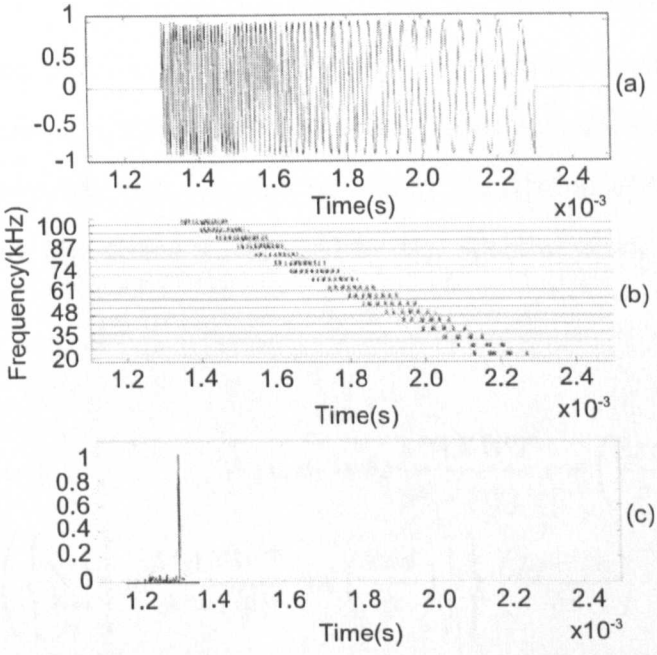

Figure 3.6: **(a):** Chirp signal. **(b):** Volley of pulses in each frequency channel for a chirp signal. **(c):** Sum of the neuron activities.

Temporal block to quantify the time of arrival of the second echo.

The peaks and notches are transformed with the use of a voting mechanism where each frequency channel votes for or against a *fine delay*. The vote is done by using a cosine wave for each frequency channel, where the frequency of the cosine wave corresponds to the frequency of the filter channel. The positive region of the cosine wave corresponds with delay values favoured by the frequency channel whereas the negative regions represent delay it disagrees with. All the cosine waves start at the time of arrival of the first echo, as determined by the Temporal block. Moreover, the cosine waves are scaled in relation to the strength of the echoes. The scaling coefficient is calculated on the energy contained in the filter output at the time of arrival. Finally, the *fine delay* is determined by summing along the time axis the voting patterns (cosine waves) where the delay of the second echo is identified by the position of the maximum value. The voting patterns (cosine waves) are set up in order to have the sum of the basis vectors to be null for

every delay except the one corresponding to the *fine delay*. When a single echo is presented to the SCAT model, the Spectral block responds with flat responses because of the use of wrapped cosine waves. Moreover, the cosine waves are weighted to compensate the non uniform energy repartition of the LPM chirp. Equation 3.1 show the cosine waves used by the Spectral block [Saillant et al., 1993].

$$W(p,d) = \delta p \frac{MAXWT}{p^2 - \left(\frac{\delta p}{2}\right)^2} \cos\left(\frac{2\pi d}{p}\right) - \left(\left\{\sum_{p_j}\left[\delta p \frac{MAXWT}{p^2 - (\frac{\delta p}{2})^2}\cos\left(\frac{2\pi d}{p}\right)\right]\right\}\left(\frac{p_f - p_i}{\delta p}\right)^{-1}\right) \tag{3.1}$$

where $MAXWT$ is an arbitrary scaling constant which determines the maximum magnitude of the weighting pattern, d is the echo delay and p the centre period of each filter. The weighted cosines waves are applied to determine the *fine delay* with Equation 3.2 to normalise it to the energy contained in the emission over the period of integration [Saillant et al., 1993].

$$F(p,t) = \sum_{p_j} \frac{\int_{t-\frac{\delta t}{2}}^{t+\frac{\delta t}{2}} R\left[p, \lambda + f\left(p\right)\right] d\lambda}{\int_0^{\delta t} T\left[p, \lambda + f\left(p\right)\right] d\lambda} W\left(p,d\right) \tag{3.2}$$

where R is the spectrogram of the received signal and T is the spectrogram of the transmitted signal. δt is the period of integration of the filters defined in the Temporal block and $f(p)$ corresponds to the temporal offset required to align the frequency channel neuron responses due to the nature of the chirp signal. Figure 3.7 illustrates the principle of the voting mechanism (cosine waves) to determine the fine delay. f_1 to f_n have a cosine wave starting at τ_n determined by the Temporal block. T_1 corresponds to the time of arrival of the first echo and T_2 the time when all the cosine waves are having their maximum value. This time corresponds to the time of arrival of the following echo.

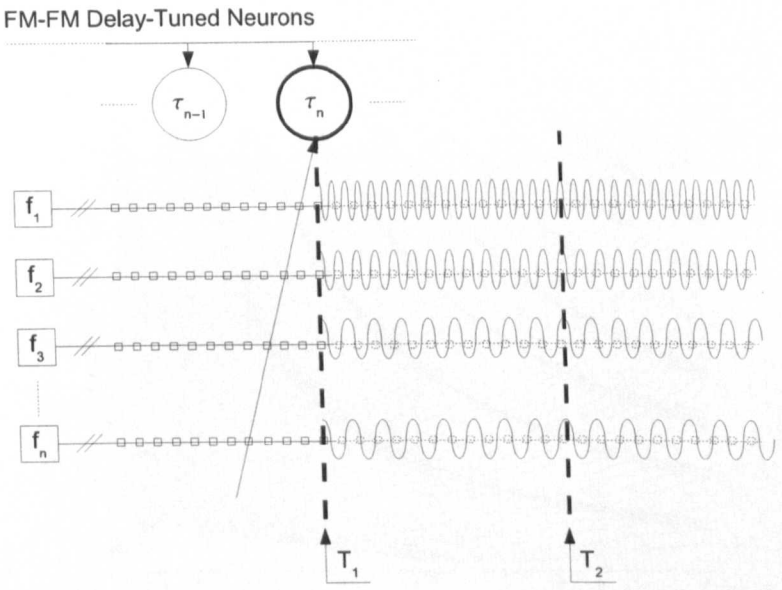

Figure 3.7: Voting mechanism of the Spectral block.

Figure 3.8 shows the weighted cosines with an amplitude value at time $t = 0$ null. With such weighted cosines, the sum along the time axis will create a signal with a zero value at the starting time. The final output from the Spectral block is illustrated on Figure 3.9 for a sum of two chirp signals separated by 50 μs. It also shows the cosine waves weighted by the energy in each filter output.

3.3.1.5 Output signals with the SCAT model

The signal from the SCAT model is formed by combining the response returned from the Temporal block and the Spectral block. The time of arrival of the first echo, T_1, is determined by the position of the maximum in the sum of the filter outputs. This maximum is replaced in the final SCAT signal by a short pulse. Then the signal returned by the Spectral block is concatenated. Figure 3.10 and 3.11 illustrate the signal formed by the SCAT bat model when two LPM overlapping chirp signals are presented. The chirp signal used for the simulation was a LPM chirp sweeping from 110 kHz down to 15 kHz on a period of 2 ms.

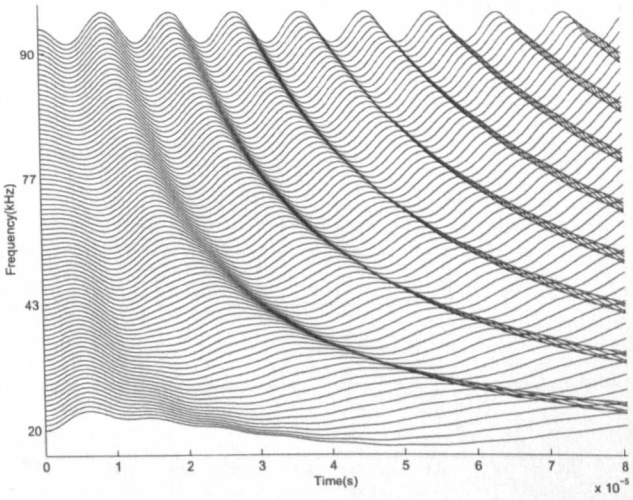

Figure 3.8: Warped cosine waves used to cancel sidelobes.

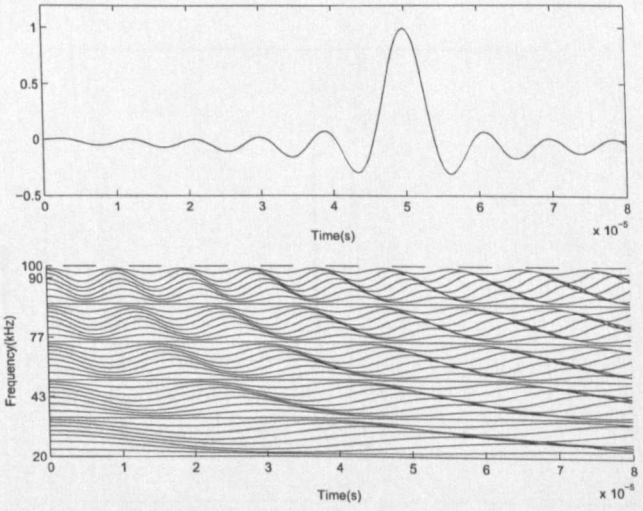

Figure 3.9: Illustration of the output of the Spectral block from time separation of 50 μs.

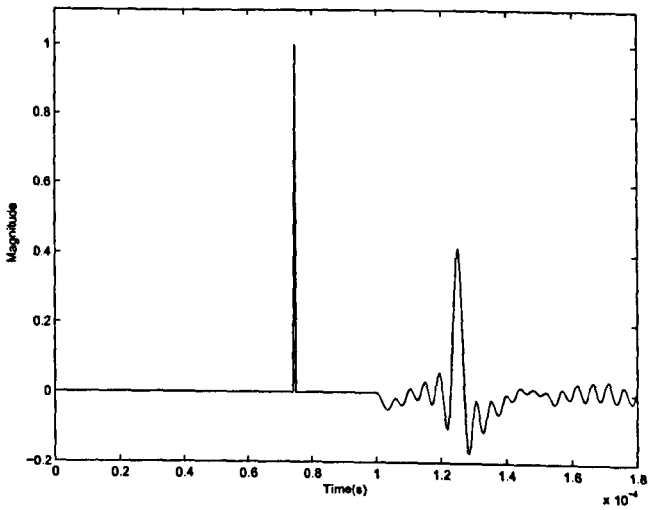

Figure 3.10: SCAT output signal for two LPM chirps located at 75 μs and 125 μs.

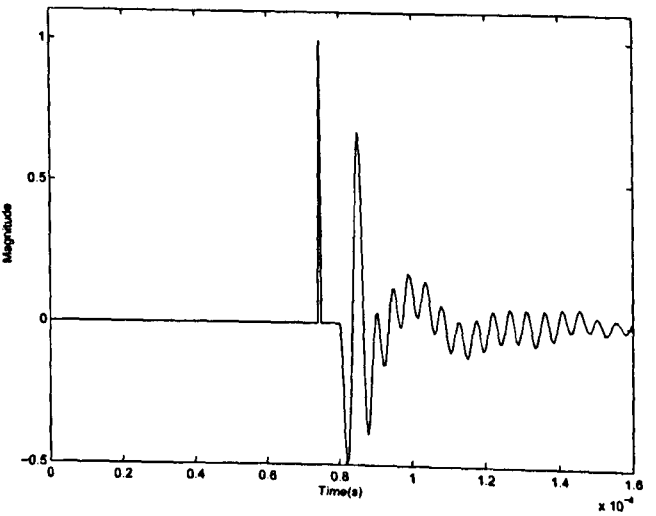

Figure 3.11: SCAT output signal for two LPM chirps located at 75 μs and 85 μs.

3.3.1.6 Discussions

The SCAT model was designed to reproduce range resolution measured on the bat from the current knowledge of the auditory system. The jitter esperiment as described by [Simmons et al., 1998], aimed to quantify by a simple set-up the range resolution of a bat *Eptesicus fuscus*. Those experiments showed the *Eptifuscus fuscus* bat separates echoes by as little as 2 μs to 10 μs. The SCAT model achieves a separation capability of 6 μs by combining temporal and spectral information. The model provides evidence that such mechanisms may be used by bats to increase the resolution with regard to a higher time of integration (350 μs). The model overcomes this limitation with the use of frequency interference patterns, where proper interpretation of these patterns lead to a *fine delay*.

The model brings the parallel processing involved in the bat auditory system and the underlying processing that suggest a way to reconstruct the range image with fine structure. In fact, the model involves a series of transforms equivalent to simultaneous, parallel forward and inverse transforms on echoes to approximate the impulse responses of targets.

However, the SCAT model does not achieve the apparent resolution of the bat (2 μs). Moreover, the performance of the model was only evaluated on idealistic simulated echoes. The performance may be questioned with in the field recorded echoes or more realistic simulated echoes. Influence of the attenuation due to air, filter processes involved in the bat's ear, more complex echo structure, beam profile, sound directionality and frequency attenuation dependence are some parameters that may influence the performance of the model. These aspects are discussed in Chapter 5.

3.3.2 MATSUO model

The second model presented here was developed by [Matsuo et al., 2004] to determine the range of multiple closely spaced objects. The purpose of this model is to reproduce the way bats form detailed range acoustic images. Similar to the SCAT model, it combines frequency and time domains to determine the range of individual echoes in a sum of multiple closely spaced echoes.

3.3.2.1 Organisation of the model

The first processing block is based on a Gaussian chirplet bank to decompose the signal into subbands as is similarly done in the cochlea. This block is used to determine the time of arrival of the overall group of echoes. The chirplet is a finite time chirp signal matching the sweep and frequency range of the main chirp signal. Then, the discrimination of following echoes is done with the use of a process named *the reflected intensity distribution.* This second technique can be viewed as layer peeling, consisting of using an approximation of the frequency spectrum of the previously determined delays to cancel out its effect and retains only information about following elements.

Figure 3.12 shows the organisation of the bat auditory model. An overview of the steps in the model starts by transforming the signal $x(t)$ with a Gaussian chirplet bank. Then the 101 outputs are shifted to align the time of occurrence to the starting of the chirp signal. The first step consists of determining T_1, the time of arrival of the first echo, with a technique described in the following Section. From T_1, the recursive algorithm starts. The next time delay is found by the use of the value of the Cepstrum. The existence of a following echo is determined with the ratio $\frac{C_{peak}}{C_0}$ where C_{peak} is the value of the peak in the Cepstrum and C_0 the value at time $t = 0$. If this ratio is over a threshold then there is another echo. The following time of arrival is determined by the use of the Cepstrum indicated by the

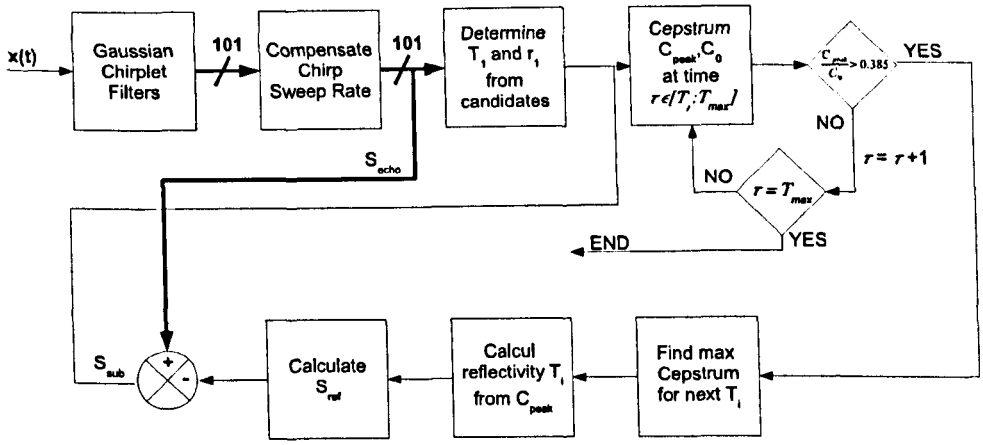

Figure 3.12: Diagram of Matsuo bat auditory model.

time of the maximum value and the reflectivity from the value of C_{peak}. Then an approximation of the frequency response from the current known echoes named S_{ref}, is calculated. This approximation is subtracted from S_{echo} to cancel the influence of the echoes already determined, where S_{echo} corresponds to the outputs from the Chirplet bank. Finally the algorithm is repeated again to determine if there is another echo in the signal and again calculates an approximation until the last echo. The steps of the algorithm are described in the following Sections.

3.3.2.2 Gaussian chirplet bank

The waveform is processed into a spectrogram like representation. The transformation is realised with a set of Gaussian filters. The process is similar to the one done in the SCAT model but rather than using a CF for the filter, it uses a chirplet signal. The chirplet filter is described in the Equation 3.3:

$$F(f_j, t) = \exp(-\frac{t^2}{\alpha}) \exp(2\pi(f_j t + \frac{1}{2} s t^2)) \tag{3.3}$$

where f_j is the starting frequency for the j^{th} chirplet filter, s is the sweep rate of the emitted wave and α is a parameter for the width of the window function. The

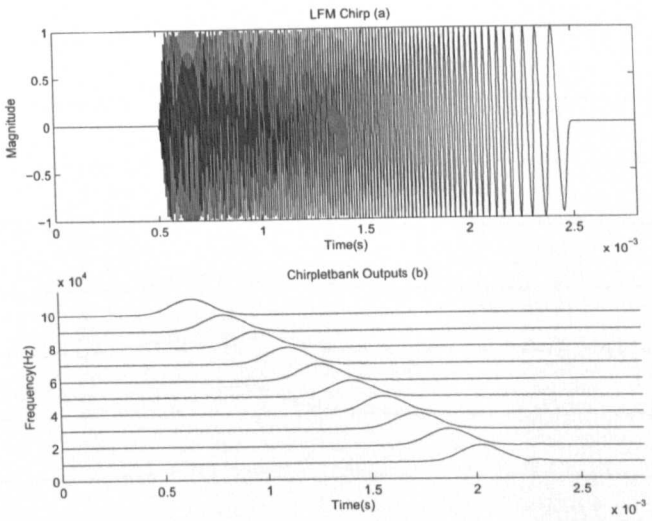

Figure 3.13: **(a)**: Linear Frequency Modulated (LFM) chirp signal. **(b)**: Magnitude of ten Gaussian filterbank outputs.

Matsuo et al model used a filterbank of 101 filters with a centre frequency starting from 20 to 120 kHz. At 50 % of peak height, the width of the window function for all the filters was 160 μs. The waveform is transformed by the Gaussian filter bank into a frequency-time representation named S_{echo}. Figure 3.13 illustrates the output of the Gaussian chirplet bank. The model was using a single emission of an LFM chirp signal sweeping from 135 kHz down to 5 kHz on a period of 2 ms. This chirplet filter offers an advantage by extracting more temporal changes compared to the CF carrier. Moreover, the sweeprate rate of the chirplet bank can be matched that of the chirp signal under investigation. Figure 3.14 shows two outputs, generated by the chirplet approach and the CF chosen in the SCAT model. When two chirps are processed, the SCAT, solid line on Figure 3.14 does not indicate the variations whereas the Chirplet transform indicates the temporal changes by mutiple changes in the temporal signal.

3.3.2.3 Reflected intensity distribution

The reflected intensity distribution was introduced by *Matsuo et al* to approximate the frequency patterns that occur when chirps are overlapping. The

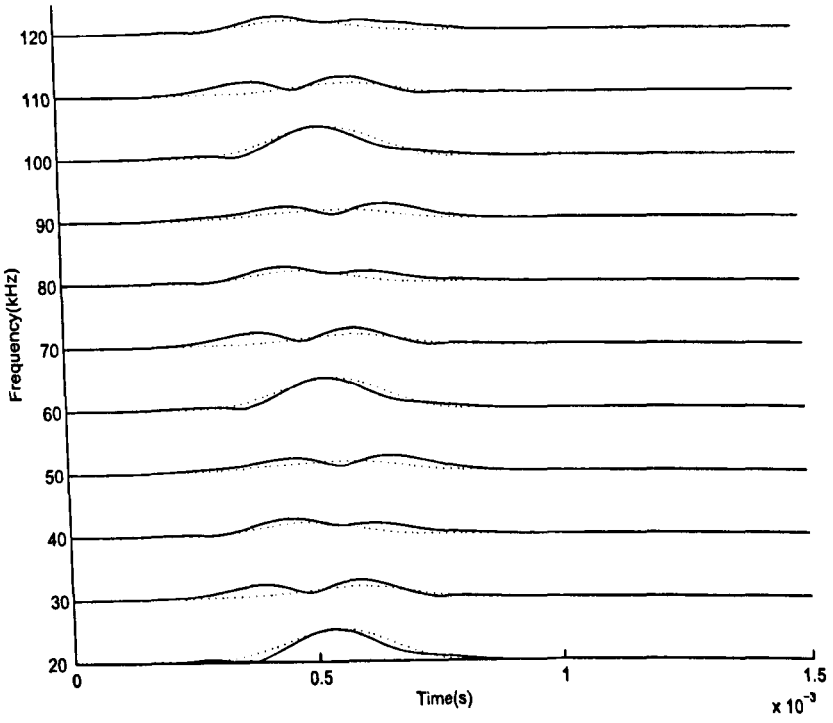

Figure 3.14: The solid line shows the outputs from Matsuo model whereas the dotted line shows the outputs from the filter used with the SCAT.

reflected intensity distribution is created by multiplying the temporal emission pattern W_{emi}, with a representation of the delay time of the echoes, by a short pulse. W_{emi} represents the magnitude of the Gaussian chirplet time response as shown on Figure 3.15. Figure 3.16 illustrates the principle of the windowed reflected intensity distribution with two objects at 4100 μs and 4150 μs. The results from the products of difference T are shown on Figure 3.17. These range-frequency patterns are named $R(f, \tau)$. When the sum of overlapping chirp signals with the same time of arrival is processed by the Gaussian filterbank, the resultant range-frequency patterns, named $S_{echo}(f, \tau)$, is similar to the one produced by Fourier transformation of the reflected intensity distribution $S_{ref}(f, \tau)$. Figure 3.18 shows the frequency responses from the Gaussian chirplet transform, $S_{echo}(f, \tau)$, to compare with Figure 3.19 showing $S_{ref}(f, \tau)$.

From Matsuo et al, the determination of the time of arrival of multiple echoes

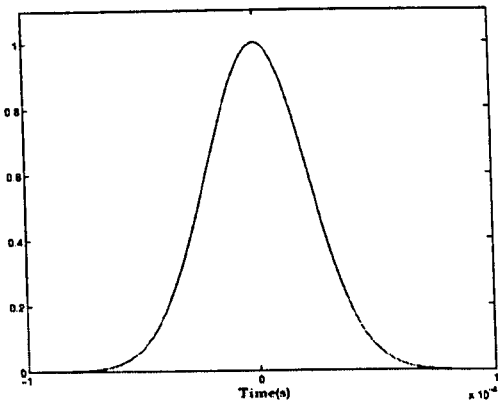

Figure 3.15: Emission pattern W_{emi}.

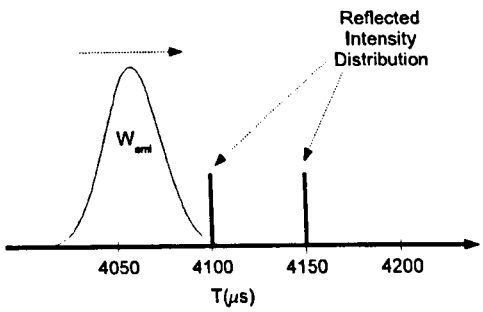

Figure 3.16: W_{emi} and the two reflected intensity distribution of objects.

is highly dependent on the determination of the time of arrival of the first echo T_1. Therefore *Matsuo et al* introduced a method based on using successive outputs from the Gaussian filter bank.

3.3.2.4 Candidate technique for first time of arrival estimation

The method can be illustrated in the case of a single object where the filter outputs are identical to Figure 3.15. Stating the fact that the echo spectra around the onset delay (τ_{on}) is mainly dependent on the first delay, T_1, S_{echo} is used at two successives times τ_{on} and $\tau_{on} + 10\ \mu s$. τ_{on} corresponds to the time when the Chirplet filter starts to respond to a signal. Considering an object located at time $T_1 = 4100\ \mu s$ with reflectivity r_1. At the time around τ_{on}, the product of W_{emi} and the reflected intensity of the object is as illustrated on Figure 3.20 where

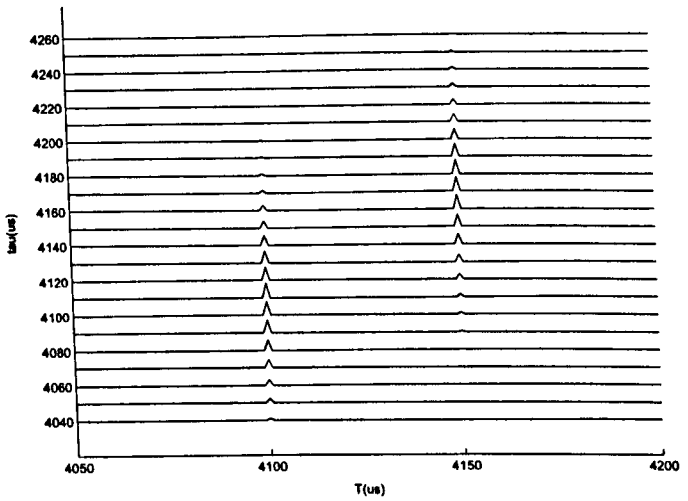

Figure 3.17: Windowed reflected intensity distribution $R(f, \tau)$. The time of arrival of the objects are 4100 μs and 4150 μs.

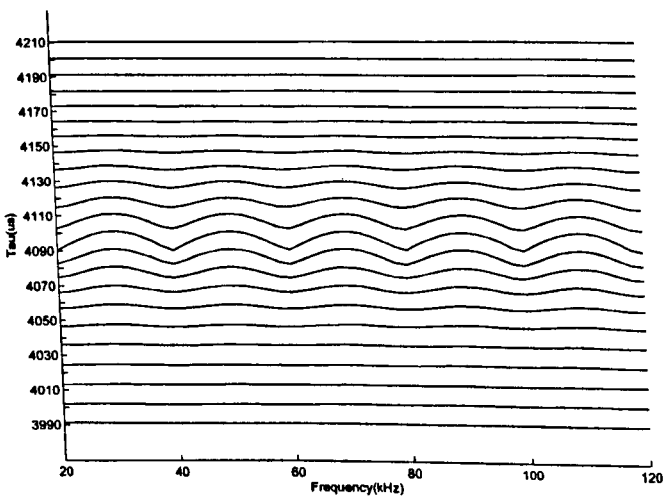

Figure 3.18: $S_{ref}(f, \tau)$: Fourier transform of the windowed reflected intensity distribution.

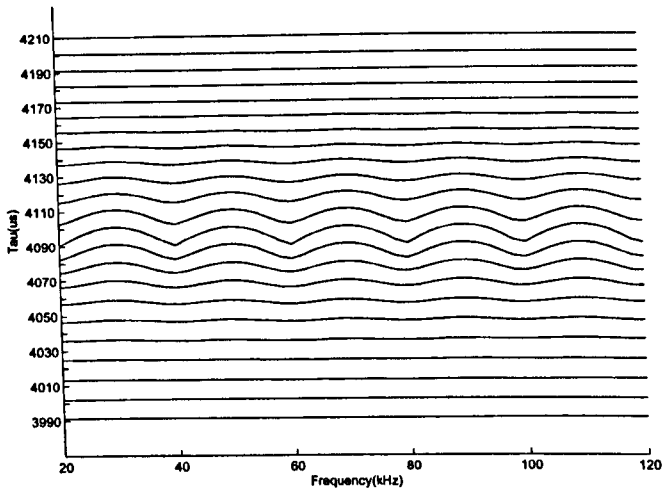

Figure 3.19: $S_{echo}(f, \tau)$: Outputs from the Gaussian filters.

it shows two products at τ_{on} and $\tau_{on} + 10\ \mu s$. The results of the products are composed of the magnitude of W_{emi} at the time τ_{on}, named g_1 and the reflectivity value of the object. The product at the time $\tau_{on} + 10\ \mu s$ is equal to $g_2 * r_1$ where g_2 corresponds to the magnitude of W_{emi} 10 μs later. Those products correspond to the windowed reflected intensity distribution as shown on Figure 3.17. From this two products, the candidates at τ_{on} and $\tau_{on} + 10\ \mu s$ are calculated by dividing each product by the pattern W_{emi} resulting in the candidates shown in Figure 3.21. Each of the value correspond to a possible time of arrival for an object. The proper candidate between the two sets is the one with the same amplitude value, in that case at the time $T_1 = 4100\ \mu s$. The values of the two successive products $(g_1 * r_1,\ g_2 * r_1)$ is extracted from the frequency-patterns S_{echo} at time τ_{on} and $\tau_{on} + 10\ \mu s$.

3.3.2.5 Determination of delay times of closely spaced objects

After the time of arrival of the first T_1 has been determined, the subsequent time delays are calculated with the use of the Cepstrum, which is similar to an inverse Fourier transform. The Cepstrum is computed with the basis functions defined in Equation 3.4 and Equation 3.5:

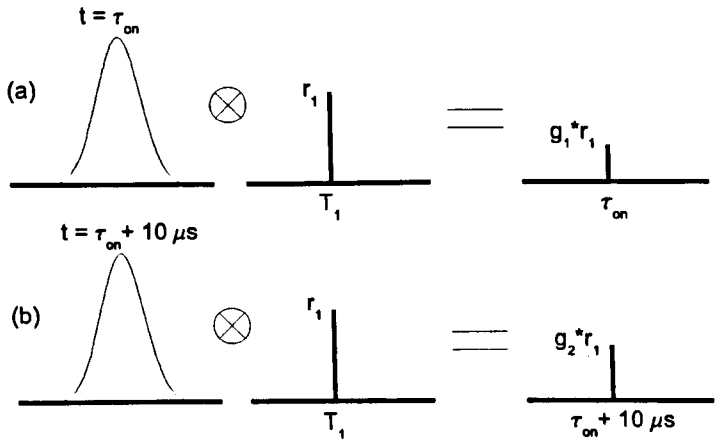

Figure 3.20: Products of W_{emi} with reflected intensity distribution of an object. **(a)**:Product of the magnitude g_1 of W_{emi} at the time τ_{on} with the object reflectivity r_1. **(b)**:Product of the magnitude g_2 of W_{emi} at the time $\tau_{on} + 10$ μs with the object reflectivity r_1.

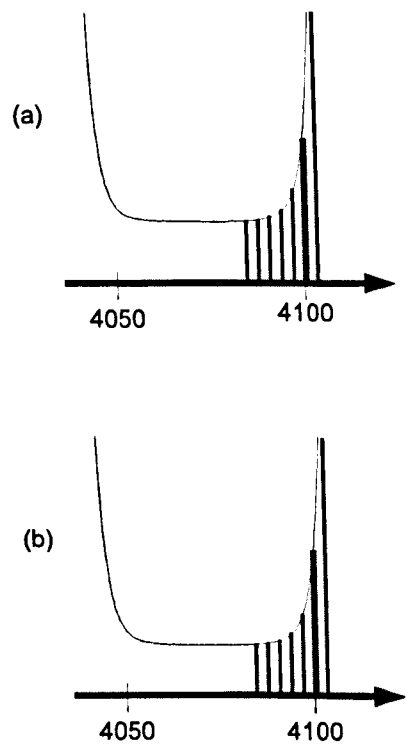

Figure 3.21: Two sets of candidates for T_1. **(a)**: Candidates at the time τ_{on} when dividing $g_1 * r_1$ by W_{emi}. **(b)**: Candidates at the time $\tau_{on} + 10$ μs when dividing $g_2 * r_1$ by W_{emi}.

$$W_{cos}(f_n, t) = \cos(2\pi t f_n) - \left\{ \sum_j \frac{\cos 2\pi t f}{N} \right\} \tag{3.4}$$

$$W_{sin}(f_n, t) = \sin(2\pi t f_n) - \left\{ \sum_j \frac{\sin 2\pi t f}{N} \right\} \tag{3.5}$$

where f_n is the starting frequency of the Gaussian filter and N is the number of filters. The bases are then used to form two cepstras combined with the values of the Gaussian filter outputs. Equations 3.6 and Equation 3.7 show the two cepstras formed:

$$C_{cos}(t, \tau) = |Ssub(f_n)|^2 W_{cos}(f_n, t) \tag{3.6}$$

$$C_{sin}(t, \tau) = |Ssub(f_n)|^2 W_{sin}(f_n, t) \tag{3.7}$$

The final Cepstrum is formed as in Equation 3.8:

$$C(t, \tau) = \sqrt{(C_{cos}(t, \tau))^2 + (C_{sin}(t, \tau))^2} \tag{3.8}$$

This final Cepstrum in Equation 3.8 is used to inverse transform the range-frequency patterns. When there is more than one object, the Cepstrum will contain a peak value at the time-delay separation between overlapping echoes. Firstly, to determine if there is more than one object, *Matsuo et al* also introduced a method based on evaluating the amplitude of oscillations in the spectra. The ratio $\frac{C_{peak}}{C_0}$ where C_{peak} is the value of the peak in the Cepstrum and C_0 the value at time $t = 0$ is the criteria of evaluation as C_{peak} and C_0 are related to the magnitude of oscillations in the spectra. If this ratio is higher than the threshold 0.385 then it is considered that the signal contained more than one element and therefore the Cepstrum could be applied to determine the time of arrival of the

following echo. This value of 0.385 was set by experiments as suitable to evaluate the presence of oscillations in the spectra.

Difficulties occur when there are more than two elements as the Cepstrum indicates all the delay separation between the echoes, e.g. for three elements, delay between T_1, T_3 and T_2, T_3. The algorithm determines all the other possible time delays with their associated reflectivity. The selection of the proper time delay is done by comparing the Fourier transform of the original signal, S_{echo}, with the approximation computed from the reflected intensity distribution, S_{ref}.

When the proper delay is determined, S_{ref} is calculated for all the current known delay times. A new frequency-pattern is computed $S_{sub} = S_{echo} - S_{ref}$ and the analysis process starting from the Cepstrum is repeated. The recursive analysis stops when there are no more reflected objects, as determined by the Cepstrum when no more oscillations are present.

3.3.2.6 Output signals with Matsuo model

Figure 3.22 and Figure 3.23 illustrate the results returned by the model from *Matsuo et al.* Both images shown the delay times determined for the case of three overlapping chirp signals.

Figure 3.22 shows three overlapping chirps at 4100 μs, 4150 μs and 4225 μs with each of them with a reflectivity of 1. The model determines properly the three time delays but with a respective reflectivity of 1, 1.01 and 0.98.

Figure 3.23 shows three overlapping chirps at 4100 μs, 4120 μs and 4130 μs with again a respective reflectivity of 1. The model determined the three time delays as 4101 μs, 4122 μs and 4130 μs with a respective reflectivity of 1.1, 0.98 and 0.85.

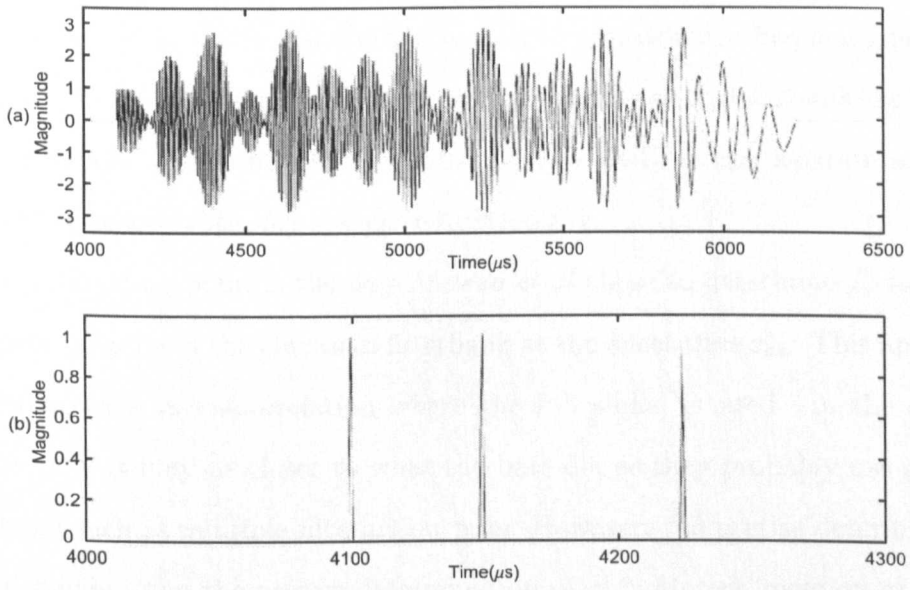

Figure 3.22: **(a)**: Sum of three overlapping chirp signals. **(b)**: Output signal of Matsuo bat auditory model.

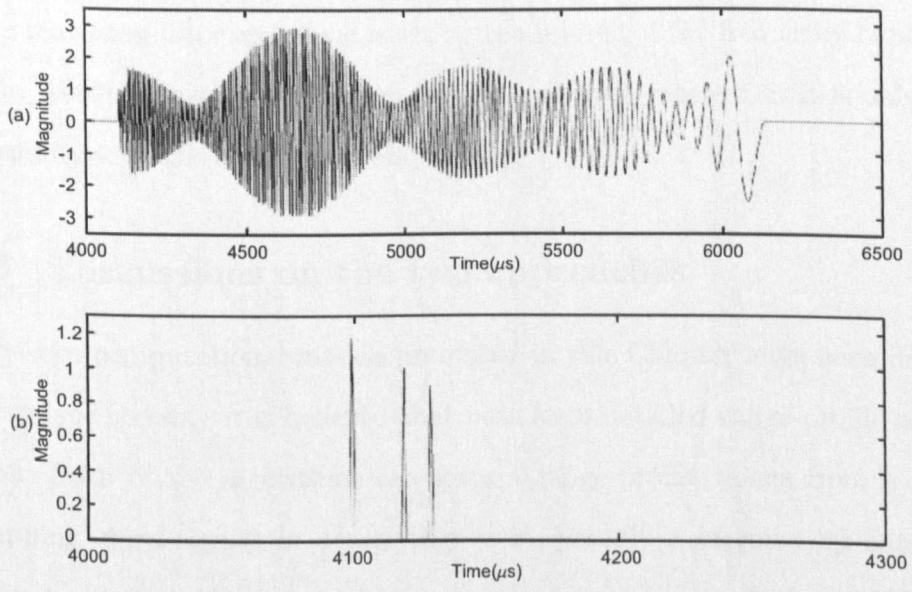

Figure 3.23: **(a)**: Sum of three overlapping chirp signals. **(b)**: Output signals of Matsuo bat auditory model.

3.3.2.7 Discussions

The reflected intensity distribution is used to approximate frequency patterns from previous delay and used to cancel out their influence to determine the following time delays. From the results [Matsuo et al., 2004], it can separate multiple overlapping echoes with any associated reflectivity.

The interesting point is the way *Matsuo et al* chose to determine T_1 by using successive outputs of the Gaussian filterbank at the onset time τ_{on}. This approach is different from cross-correlation where the full signal is used. In the case of *Matsuo et al* it may be closer to what the bats do, as they probably use parallel processing such as multiple filtering outputs. However, the precise determination of T_1 depends upon the precise determination of τ_{on}. *Matsuo* mention of such a technique in [Matsuo et al., 2001].

Moreover the model can resolve objects with a minimum time separation of 10 μs with a precision of 1 μs on the time of arrival. This resolution of 10 μs is equivalent to the theory of radar where the resolution for a coherent receiver using a matching filter technique is set by the inverse of the frequency bandwidth [Barton, 1997]. However, the model is not a coherent receiver as it is only using the magnitude of the chirplet decomposition.

3.3.3 Discussions on the two approaches

The two computational models presented in this Chapter have been designed to reproduce the way it is believed that bats form detailed range-profile acoustic images. Both of the algorithms can form a range-profile image from a sum of overlapping chirp signals in a way that is supposedly performed by bats. The complexity of the Matsuo model is more significant than with the SCAT model which separate an infinite number of overlapping signals. The performance of the SCAT model has been shown to achieve a resolution of 6 μs, i.e. about 2 mm in

air, to separate a maximum of two overlapping chirp signals. This performance is not equivalent to the one achieved by bats of 2 μs, i.e. 0.7 mm in air, but in superior to the theoretical limit set by the inverse frequency bandwidth, i.e. 10 μs.

These models reproduced to some extent the underlying processes involved in the bat auditory system without necessarily using chirp signals similar to those used by the bats, i.e non-linear type. Moreover, the author processed the chirp signals under idealistic conditions that may not be relevant to those encountered by bats when hunting for a flying prey. The approaches described in the models have to be evaluated to determine if they can be used under practical imaging conditions. The robustness to noise and the influence of air attenuation must be quantified.

3.4 Conclusion

This Chapter presented a set of bat auditory models developed to reproduce behavioural tasks observed by experiments done in the field or a laboratory. The aim of the models varies from finding the position of an object in a three dimensional space, range discrimination or robots mimicking bats.

The models based on range discrimination appear to be of interest to develop innovative imaging techniques. When both models are compared, the enhancement in the resolution appears to be obtained by combining parallel processing and signal processing techniques (Cepstrum) to lead to enhanced axial resolution. The techniques presented in that Chapter are now used to develop a bio-inspired imaging algorithm to enhance image resolution in ultrasonic applications.

Chapter 4

Bio-Inspired Range finding Algorithm (BIRA)

4.1 Introduction

Bats show a remarkable capacity to track an insect in open air. Their echolocation system has evolved to detect and identify a moving insect in complex surrounding environments. Literature about bats indicates that they do not perform a simple tracking task of the movement. In fact, they appear to form detailed acoustic images to characterise elements contained in their surroundings. Each object is identified by its acoustic signature, also termed its impulse response. The impulse response of an insect, depending on the angle of view, is going to be formed from a set of closely spaced "replicas" of the incident wave. The various delay times between the "replicas" give information about the characteristics of the insect, such as the dimensions of the insect, size of the wings, etc... Due to the size of the insect, it is required for the bats to be able to precisely determine the delay time of each "replica" to characterise its acoustic signature. As stated previously, experiments have been conducted and have shown that they can reach a resolution far above any current approach. In other words, they possess a high range resolution when compared to the frequency bandwidth they use.

The processes by which they accomplish such a task have been evaluated with computational models based on the current knowledge of the bat auditory system. By extracting techniques used in these models, it indicates a possible way forward for reproducing the bat's resolution. The purpose of this Chapter is to present the work done on mimicking the bat auditory system to reproduce the resolution achieved by bats. It applies the known processes used by bats to obtain such a high range resolution. The new model is then compared to other well-established techniques used to enhance the axial resolution [Lewis, 1987].

Firstly, this Chapter presents some of the well-established techniques for resolution enhancement based on deconvolution. Secondly, the new Bio-Inspired Range finding Algorithm (BIRA) is presented, mimicking the bat auditory system

with the aim of improving the axial resolution. Finally, a Section of discussions and conclusions on the work are presented.

4.2 Deconvolution techniques

4.2.1 Definition of the deconvolution problem

The deconvolution process consists of solving an inverse problem where the goal is to separate the impulse response of the device, i.e. the transducer, and the impulse response from the system, i.e. the object to image. In our case, the deconvolution algorithms are applied on a one-dimensional signal. A mathematical description of the type of signal on which the algorithms are applied is shown in Equation 4.1 which is representative of a linear model of an ultrasonic pulse-echo system.

$$x(t) = \int_0^{+\infty} w(\tau)u(t-\tau)\,d\tau = w(t) * u(t) \tag{4.1}$$

where $x(t)$ is the measured signal, $w(t)$ is the pulse-echo impulse response of the transducer and $u(t)$ is the impulse response of the system. $u(t)$ is the signal that contains information about the medium being measured using the device $w(t)$ that masks partially or fully the signal $u(t)$. The deconvolution algorithm consists of calculating an inverse form of the transducer impulse response $w(t)$. Then the inverse form is applied to the measured signal $x(t)$ to extract $u(t)$. However, the computation of the inverse of $w(t)$ is inherently ill-conditioned [Lewis, 1987]. The stability of the solution computed by the inversion process depends on the type of data measured, $x(t)$. A small error in the data can result in a large unwanted signal. Therefore in order to make the process reliable, it is required to introduce some constraints on the computation of the inverse.

The various algorithms presented here introduce different constraints that im-

pairs the performance of the inversion process to produce a stable solution. Various aspects of comparison have to be covered such as the noise robustness, design time and the resolution enhancement. The primary interests are in the resolution enhancement and the robustness in noise contaminated data. Different ways of implementing the deconvolution algorithms have been developed. They can be classified in two groups of implementation, frequency domain algorithms and time domain algorithms.

4.2.2 Frequency domain deconvolution algorithms

Frequency deconvolution has two main advantages in the implementation of the inverse problem. First of all, it is based on the use of the Fourier transform that can be implemented with the Fast Fourier Transform (FFT) algorithm to reduce computation time [Oppenheim and Schafer, 1989]. The second advantage of using the Fourier domain is the transformation of the convolution operator in the time domain into a product operator in the frequency domain, reducing significantly the amount of computation to realise the same operation. Two frequency domain algorithms are presented here [Lewis, 1987]:

- A spectral division algorithm
- Oldenburg's least square algorithm

The two algorithms utilise different approaches to solve the inversion problem.

4.2.2.1 Spectral division

The spectral division is the most straightforward implementation of the deconvolution operation. Consider the received signal represented by the Equation 4.2:

$$x(t) = w(t) * u(t) \tag{4.2}$$

Taking the Fourier transform of 4.2 gives:

$$X(f) = W(f)U(f) \tag{4.3}$$

To extract the Fourier transform of the system, $U(f)$, the spectral division can be performed as:

$$U(f) = \frac{X(f)}{W(f)} \tag{4.4}$$

This expression can be rewritten as:

$$|U(f)|\exp(j\theta_U) = \frac{|X(f)|\exp(j\theta_X)}{|W(f)|\exp(j\theta_W)} \tag{4.5}$$

Calculating the inverse process is restricted by the data. In order to reduce the ill-conditioning involved in this inversion problem, a preset threshold is applied that creates a new spectrum:

$$|W_n(f)| = |W(f)| \quad for \quad |W(f)| \geq c \tag{4.6}$$

$$|W_n(f)| = c \quad for \quad |W(f)| < c$$

where c is a small, non-negative threshold. The spectral division is then performed as follows:

$$U(f) = \frac{X(f)}{\tilde{W}_n(f)} \tag{4.7}$$

The final data $u(t)$ is then obtained by inverse Fourier transforming $U(f)$.

4.2.2.2 Oldenburg

The Oldenburg deconvolution technique is a more sophisticated technique than the spectral division as it consists of designing a pulse shaping filter to maximise

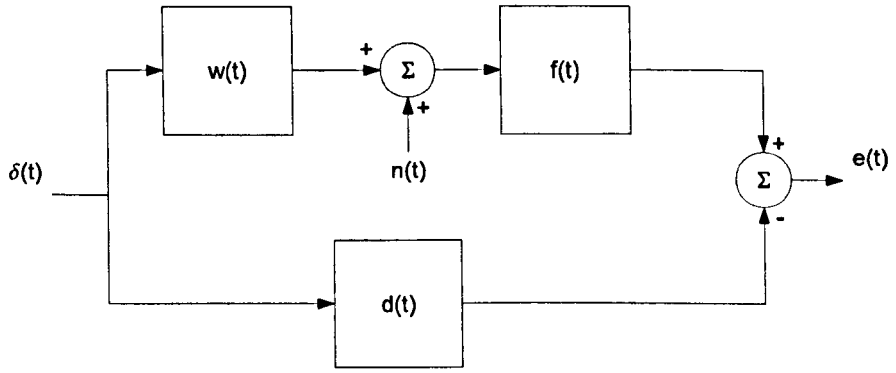

Figure 4.1: Pulse shaping for Oldenburg algorithm

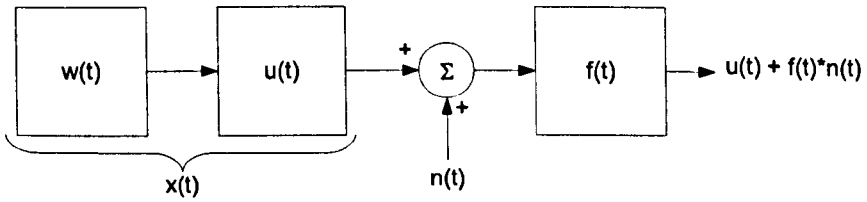

Figure 4.2: Deconvolution using the Oldenburg algorithm

the data resolution and minimise the influence of the noise [Lewis, 1987]. The purpose of a pulse shaping filter is to transform a waveform into a desired shape. Figure 4.1 illustrates the principle of the filtering technique. $w(t)$ represents the waveform to be shaped by using the shaping filter $f(t)$ to create a desired signal $d(t)$ by minimising the error $e(t)$. If $d(t)$ is set to an impulse function then the process is equivalent to deconvolving $w(t)$ from another signal. This shaping filter is applied to the observed data $x(t)$ contaminated with noise $n(t)$ in order to generate $u(t)$ as illustrated in Figure 4.2.

Under a noise-free environment, the ideal pulse shape would be an impulse. However to minimise the noise output, it is required to select a suboptimal shaping filter. This suboptimal filter introduces the generation of significant sidelobes that are due to the bandlimiting of the inversion process. To reduce the sidelobe level, a solution consists of using a gaussian bell as a desired signal $d(t)$. This type of signal minimises the sidelobe levels and also preserves the data resolution. The

design of the filter $f(t)$ is done to generate an output close to the desired output $d(t)$ and to minimise the noise level. To find a filter $f(t)$ that follows those constraints, Oldenburg introduced the use of a cost function J shown in Equation 4.8.

$$J = \cos(\theta) \int_{-\frac{T}{2}}^{+\frac{T}{2}} [w(t) * f(t) - d(t)]^2 \, dt + \sin(\theta)\sigma^2(n(t) * f(t)) \tag{4.8}$$

where $\sigma^2(n(t) * f(t))$ represents the variance of the filter noise output and θ a trade off parameter. This cost function J can be rewritten in terms of the Fourier components of each time series. The Equation in the Fourier domain is obtained by applying Parseval's theorem to give Equation 4.9.

$$J = \cos(\theta)T \sum_{k=-\infty}^{+\infty} [TW(k)F(k) - D(k)]^2 + \sin(\theta) \sum_{k=-\infty}^{+\infty} [TN(k)F(k)] \tag{4.9}$$

where T is the time duration of the time series data and $W(k)$ are the Fourier coefficients of $w(t)$ with $k \in \mathbb{N}$. The solution minimizing Equation (4.9) with respect to $F(k)$ is obtained by differentiation of J to give:

$$F(k) = \frac{\cos(\theta)W(k)D(k)}{T\cos(\theta)W(k)^2 + \sin(\theta)\eta(k)^2} \tag{4.10}$$

Equation (4.10) gives a solution in the Fourier domain that minimizes the cost function J. The solution filter is then applied to the signal $X(k)$ to determine the system impulse response $U(k)$:

$$U(k) = X(k)F(k) \tag{4.11}$$

Finally the time signal $u(t)$ is obtained by inverse Fourier transformation of $U(k)$. The Oldenburg algorithm has two properties of importance. The first one concerns an optional trade off parameter $\theta \in [0; \frac{\pi}{2}]$. It is used to constrain the

noise output at the cost of resolution. If θ is set to zero, there is no constraint on the noise but it is the closest solution to the least mean square error. When θ is increased, it constrains the noise output but decreases the resolution. The second property concerns the contaminative noise. The spectral components associated with the contaminative noise are normally assumed to be constant. Thus, the expression $\eta(k)^2$ is assigned a small non-negative value in practice.

4.2.3 Time domain deconvolution algorithms

Time domain algorithms represent an alternative approach to solve the inverse problem and are similarly based on the computation of a filter to counter-act the temporal smearing effect introduced by the transducer. Two algorithms are presented here [Lewis, 1987]:

- The Wiener Pulse Shaping filter
- The Two-Sided Wiener Pulse Inverse filter

4.2.3.1 The Wiener Pulse Shaping filter

The approach for the case of a Wiener filter is to separate a signal from its noise. A-priori knowledge of the nature of the noise and the original signal is required. For the case of this application, it is designed to separate the impulse response of the system $u(t)$ from the transducer impulse response $w(t)$ and also reduces the influence introduce by the noise. The Wiener Pulse Shaping (WPS) filter is designed to minimize the least mean square function defined by Equation 4.12 below:

$$J_{wps} = E\sum_{t=T_i}^{t=T_f} [[w(t) + n(t)] * f(t) - d(t)]^2 \tag{4.12}$$

where E is the mathematical expectation. This cost function may be rewritten using the expanded vector form shown in Equation 4.13:

$$J_{wps} = \|WF - D\|_2 + W_0 \|F\|_2 \tag{4.13}$$

where $W_0 = (T_f - T_i)N_0$, N_0 is the constant spectral density of the contaminative noise and $\|Y\|_2$ denotes the Euclidean vector norm Y^TY.

The solution that minimises Equation 4.13 is obtained by differentiating with respect to F to produce:

$$(W^TW + W_0I)F = W^TD \tag{4.14}$$

where W is a NxN matrix, F is a vector of dimension N and D is a vector of dimension N. For the case where W_0 is set to zero, Equation 4.14 becomes:

$$R_{ww}F = R_{dw} \tag{4.15}$$

where R_{ww} is the NxN Toeplitz matrix containing the positive lag autocorrelation coefficients of $w(t)$. R_{dw} is the cross-correlation vector of $w(t)$ and $d(t)$.

Equation 4.15 is of matrix form and represents a system of linear, real valued simultaneous equations which can be solved to yield a formal solution for the optimal filter F. The resulting filter F is the optimal solution of the system in term of the least mean square sense to the desired signal D.

The WPS filter has a number of important properties. First, it performs better on a waveform that exhibits minimum delay properties. However ultrasonic waveforms rarely, if ever, come into this category, being of mixed phase format. Second, the performance of the filter is optimised by specifying an optimal delay for the chosen filter output shape. Finally, the W_0 term is used to stabilise the filter in the presence of noise at the cost of the resolution.

4.2.3.2 The Two-Sided Wiener Pulse inverse filter

The Two-Sided Wiener (TSW) is defined by Equation 4.16:

$$f(t) = w(-t) * f_0(t) * f_0(-t) \tag{4.16}$$

where $w(-t)$ is the time reverse of $w(t)$, $f_0(t)$ is the 0-lag WPS filter where the desired output is an impulse function.

As it is shown, the signal is based on the WPS filter. It uses the 0-lag WPS filter and its time reversal to filter the signal. It offers the advantage not to be dependent on minimum delay properties and to be a true inverse process, as it attempts to generate an impulse function. Moreover, the optimisation is not dependent any more on the optimisation delay parameter in comparison with the WPS filter. The main disadvantage is the length of the filter that is about three times as long as the WPS filter therefore it adds a delay response equal to $2N-1$ samples where N is the length of the wavelet $w(t)$.

4.2.4 Comments on the deconvolution techniques

The spectral division algorithm presents the advantages to be an intuitive algorithm with a fast design and a simple implementation. The Oldenburg method, even if it is more sophisticated, has a fast design and a straightforward implementation. However, the Spectral division and the Oldenburg method assume that the signals are spatially invariant which obviously will not be the case in practice. Moreover, the Oldenburg algorithm performs best on minimum delay waveform.

The intuitive solution offered by the spectral division algorithm is highly dependent on the choice of the threshold that may seriously impair the final solution. The performance of the Oldenburg algorithm is limited by the choice of the desired output.

The time domain algorithms, WPS and TSW, have both a fast design and

implementation. The WPS algorithm offers the advantage to be theoretically not dependent of the minimum delay properties of the signal. This Section has presented the principle of deconvolution. The following Section presents the bio-inspired imaging algorithm.

4.3 Acoustic imaging model

4.3.1 Introduction

From the analysis of the bat auditory system, various models are described in the literature to mimic the processes involved. Each of the models reproduced a limited task achieved by the bat such as locating an object in a three dimensional space [Kuc, 1994] [Erwin et al., 2001] [Matsuo et al., 2001], identify the wing flutter of an insect [Grossetete and Moss, 1998] or reproduce the bat ability to separate two closely spaced reflectors [Saillant et al., 1993] [Peremans and Hallam, 1998] [Matsuo et al., 2004]. Those models imitate known processing involved in the bat auditory system into a computational counterpart. The algorithm introduced in this Section has been developed from the analysis of the bat auditory system and the various computational models already presented. The focus of the algorithm is to improve the axial resolution.

4.3.2 Background of the algorithm

Bats use frequency modulated acoustic signals to discriminate objects in a three dimensional space. In many situations, they show a remarkable ability to track a single reflecting object among a densely packed group of reflectors. The complex echo returned by the object is composed of the sum of overlapping echoes from the reflector ensemble. As the bats can track an insect in such environment, it seems to indicate that they are somehow capable of decomposing the summa-

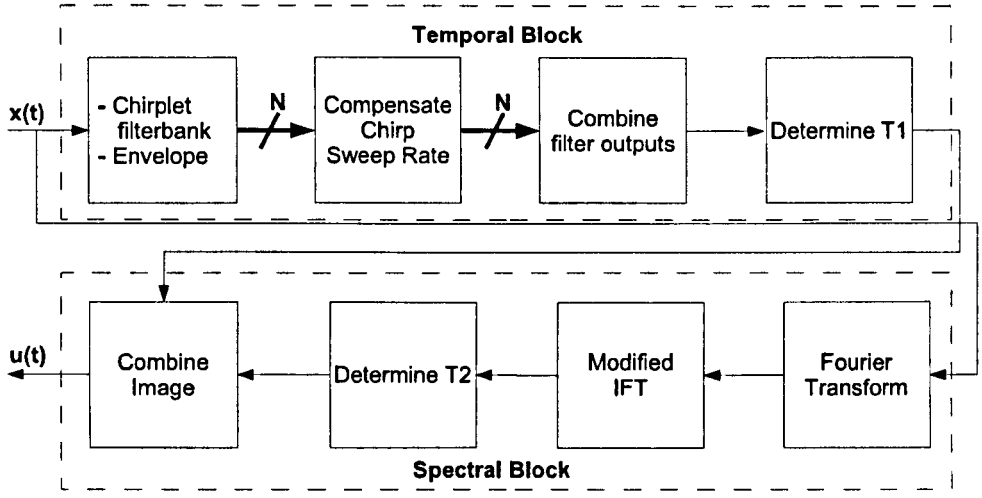

Figure 4.3: Overview of the algorithm.

tion of highly overlapping echoes into its constituent parts. When echoes overlap, they interfere with each other, cancelling or reinforcing in amplitude at different frequencies depending on their separation in time. The spectrum of the overlapping echo contains peaks and notches at specific frequencies determined by the time separation of the individual reflections. These frequency peaks and notches or "frequency interference patterns" are used in the algorithm presented here as a way forward to improve the axial resolution. A new algorithm, Bio-Inspired Range finding Algorithm (BIRA), combines the time domain and frequency domain to analyse the information of the received signal. Then the algorithm forms a time domain image indicating the time of arrival of each individual echo.

4.3.3 Outline of the algorithm

An overview of the computational model is shown on Figure 4.3. The computational model consists of two processing blocks which represent signal processing characteristics at various levels in the bat auditory system. The *temporal block* is designed to determine the time of occurrence of the first element in the sum of echoes by decomposing the received signal into subbands. The processing is done

by N parallel pathways and the respective information about the time of arrival is combined to determine an average time of arrival. The *spectral block* makes use of the frequency domain to resolve the time of appearance of the following successive echoes. It converts frequency interference patterns into time of arrival of each echo. This algorithm combines the techniques used from previous computational models using the subband decomposition from [Matsuo et al., 2004] and the cesptrum techniques from [Saillant et al., 1993] [Matsuo et al., 2004]. The software development of BIRA has been implemented in Matlab©.

4.3.3.1 Temporal block

The rule of the *temporal block* is to encode the waveform into a spectrogram-like format as it is done in the mammalian auditory system. The inner ear of a bat is composed of an element named the basilar membrane that transforms the acoustic vibrations into electric signals. Frequency sensitivity varies along this membrane from one end to the other and can be modelled (as a first approximation) as a filterbank with constant frequency carrier, to approximate the inner ear [Saillant et al., 1993].

However, with such a filterbank, as shown in Chapter 3, it was not possible to extract interference patterns in the temporal domain as they were masked by the CF carrier. The alternative choice was based on a Gaussian chirplet transform with a carrier frequency in agreement with the sweep rate of the emission [Matsuo et al., 2004]. The characteristics of the chirplet filter can be described by:

$$F(f_j, t) = \exp(-\frac{t^2}{\alpha}) \exp(2\pi(f_j t + \frac{1}{2} s t^2)) \tag{4.17}$$

where f_j is the starting frequency for the j^{th} chirplet filter, s is the sweep rate of the emitted wave and α is a parameter for the width of the window function. The chirplet filter matches a LFM chirp emission. The model used a set of filters

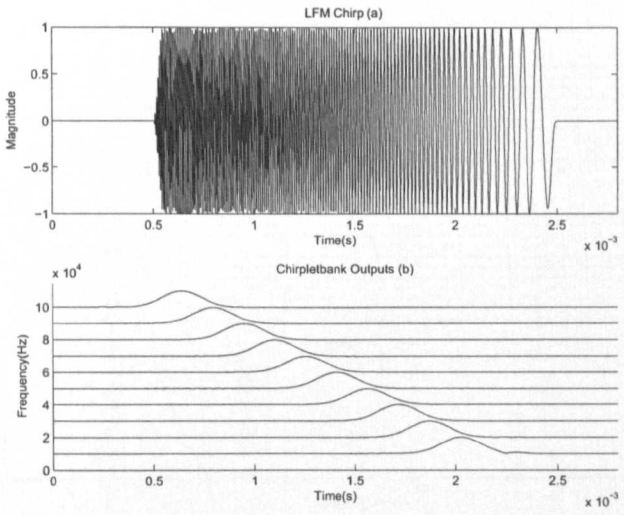

Figure 4.4: **(a):** Linear Frequency Modulation chirp signal from 135 kHz to 5 kHz Period = 2 ms. **(b):** Magnitude of the outputs of ten chirplet filters.

to split the signal in parallel pathways and determine the time of occurrence of each chirplet where each chirplet is a part of the overall chirp. The principle with a set of ten chirplet filters to transform a LFM chirp is illustrated on Figure 4.4.

This process transforms a One Dimensional (1D) signal into a parallel processing unit which is similar to the processing involved in the bat auditory system. It models the frequency selectivity of the basilar membrane with a set of chirplet filters: Each chirplet filter represents a "part" of the basilar membrane. It is also designed to mimic the parallel processing that occurs in the bat auditory system. Only the envelope of the chirplet filter outputs was used as it models a smoothing process involved in the auditory system [Saillant et al., 1993]. As the nature of the broadcasted signal is known, it is possible to decompose the chirp into chirplet components. Then the time of occurrence of each individual chirplet is combined to determine the time of occurrence of the overall chirp or sum of overlapping chirps, as shown on Figure 4.5(a). In order to combine the time of occurrence, the chirplet filter outputs are shifted in time to compensate for the chirp sweep rate, as shown on Figure 4.5(b). Finally, all the outputs are summed along the time axis to represent the average time of occurrence of the chirp, as shown on

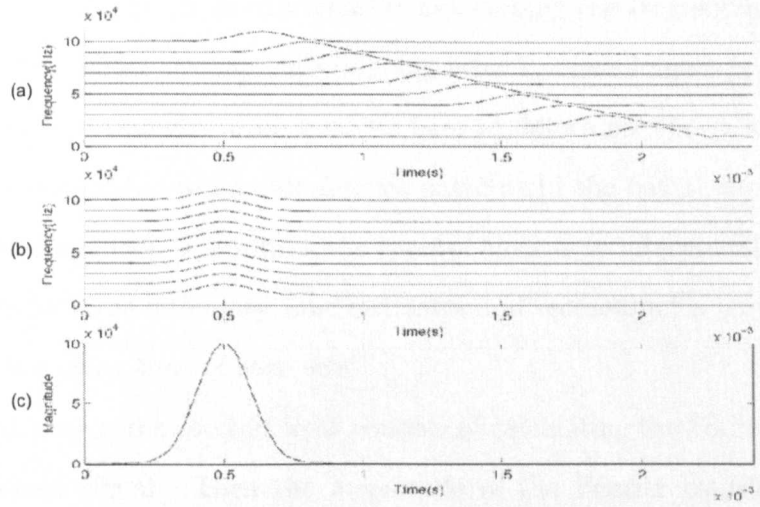

Figure 4.5: **(a):** Magnitude of the ten outputs of the chirplet filters. **(b):** Compensated outputs for the sweep rate of the chirp. **(c):** Sum of the compensated outputs.

Figure 4.5(c). It represents a combined estimator of the distance to the nearest echo where the estimate of the time of arrival is obtained by the location of the maximum.

The model is designed to process an emission with a single LFM sweep. The emission starts at 135 kHz and sweeps down to 5 kHz in a period of 2 ms. The rise and fall times are 50 μs. This emission is a simplified version of the bat acoustic emission, as the purpose of the model is to identify an object's location and the properties used are, for the time delay, considered independent on the nature of the emission.

The filter bank is composed of 101 chirplet filters with the frequency range from 20 kHz to 120 kHz positioned at regular frequency intervals. The positions of following echoes are then estimated with the use of the *spectral block*.

4.3.3.2 Spectral block

While the *temporal block* is used to determine the overall delay time, the *spectral block* is used to determine the *fine delays* which correspond to the echoes

following the first echo. Bats can separate overlapping echoes from reflecting surfaces when the echoes overlap. Overlapping echoes create frequency interference patterns that are thought to be used by bats to determine the *fine delay*. Evidence of the use of frequency interference patterns in the bat auditory has been shown [Schmidt, 1988]. The aim of the *spectral block* is to interpret the frequency interference patterns into delay time estimates and reconstruct a temporal signal indicating the delay time of each echo.

The first step in the *spectral block* consists of calculating the Fourier transform of the received signal. Then the magnitude of the Fourier transform is used to work out fine delay time estimates. The frequency interference patterns are characterised as oscillations in the magnitude of the spectrum. Considering the case of two overlapping echoes $e(t)$, with magnitude r_1, r_2 and respective delay times of T_1, T_2. The received signal is expressed by:

$$s(t) = r_1 e(t - \tau_1) + r_2 e(t - \tau_2) \tag{4.18}$$

The expression for the spectrum is:

$$S(f) = E(f)\exp(-j2\pi f\tau_1)(r_1 + r_2\exp(-j2\pi f(\tau_2 - \tau_1))) \tag{4.19}$$

with $E(f)$ the spectrum of the echo $e(t)$. By differentiating $S(f)$ with respect to f the equation (4.19) and equate to zero, when considering $E(f) = 1$, the position of the peaks and notches in the spectrum are determined as:

$$f_{notches} = \frac{2m+1}{2}\frac{1}{\tau_2 - \tau_1} \tag{4.20}$$

$$f_{peaks} = m\frac{1}{\tau_2 - \tau_1} \tag{4.21}$$

The expression of the magnitude of the Fourier transform of Equation (4.19)

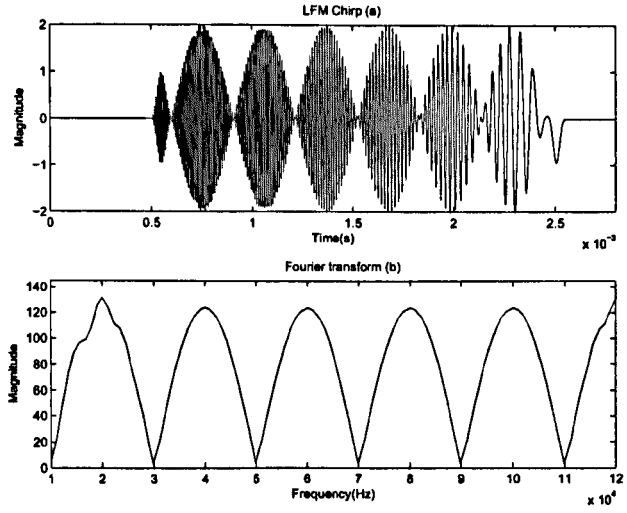

Figure 4.6: **(a):** Two LFM chirps at 500 ms and 550 ms. **(b):** Magnitude of FFT (Interference patterns).

can be expressed for the case of $e(t) = \delta(t)$ as:

$$|S(f)|^2 = r_1^2 + r_2^2 + 2r_1 r_2 \cos(2\pi f(\tau_2 - \tau_1)) \tag{4.22}$$

The oscillation patterns in the magnitude of the Fourier transform are clearly identified in Equation 4.22. Figure 4.6 illustrates an example of the sum of two overlapping chirps and the corresponding magnitude of the Fourier transform.

The transform of the frequency interference patterns, into delay estimates, is done by using a modified definition of the inverse Fourier transform, named in the literature by [Matsuo et al., 2004] as the Cepstrum. The base vectors for the calculation of the Cepstrum are altered to cancel out ripples that mask the determination of the delay time between the echoes. Moreover, to improve the delay time determination, the inverse Fourier transform is calculated on a frequency range that matches the frequency range covered by the chirp signal. It is equivalent to filtering the signal and it reduces the noise level.

The *spectral block* inverse Fourier transforms the magnitude using the base vector implemented in [Matsuo et al., 2004] and described in Chapter 3 in Equation

3.4 and Equation 3.5. The two cepstras are then derived as defined in Equation 3.6 and Equation 3.7, as described in Chapter 3. Finally the Cepstrum is obtained using Equation 3.8 in Chapter 3. This inverse process is used as it leads to the improvement in discrimination resolution cancelling out the ripples.

The inverse process consists of a inverse Fourier transform of the magnitude of the Fourier transform. To demonstrate the advantage of the altered base vectors, let's consider the Fourier transform of two $\delta(t)$ functions:

$$S(\omega) = r_1 \exp(-j\omega\tau_1) + r_2 \exp(-j\omega\tau_2) \tag{4.23}$$

The magnitude can be expressed as:

$$|S(\omega)|^2 = r_1^2 + r_2^2 + 2r_1r_2\cos(\omega(\tau_2 - \tau_1))) \tag{4.24}$$

If now, the standard inverse Fourier transform of Equation 4.23 and Equation 4.24 are calculated:

$$s_d(t) = r_1\delta(t - \tau_1) + r_2\delta(t - \tau_2) \tag{4.25}$$

$$s_m(t) = r_1^2\delta(t) + r_2^2\delta(t) + 2r_1r_2\left[\delta(t - \tau_1 - \tau_2) + \delta(t - \tau_2 - \tau_1)\right] \tag{4.26}$$

The inverse Fourier transform of Equation 4.24, which is Equation 4.26, is returning four $\delta(t)$ functions with two of them at time $t = 0$ and two at time $t = \pm(\tau_2 - \tau_1)$. By using the base vectors of Equation 3.4 and Equation 3.5, the inverse process (Cepstrum) is equivalent to cancelling out the mean value of Equation 4.24, i.e. $r_1^2 + r_2^2$. Then the inverse solution in Equation 4.26 leads to Equation 4.27 below:

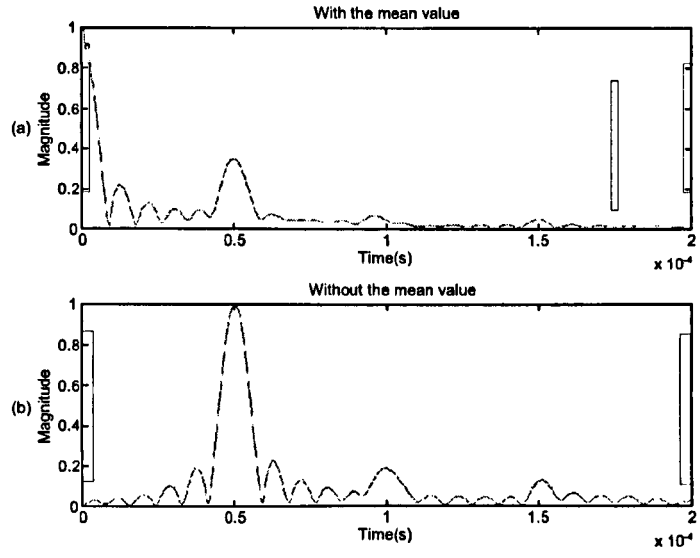

Figure 4.7: **(a):** Inverse Fourier transform. **(b):** Modified Inverse Fourier Transform (Cepstrum).

$$s_m(t) = 2r_1r_2\left[\delta(t-\tau_1-\tau_2)+\delta(t-\tau_2-\tau_1)\right] \tag{4.27}$$

The inverse signal from Equation 4.27 contains a peak value at time $t = \tau_2 - \tau_1$ when only considering the positive time. This time corresponds to the time delay between the signals. The fact of using the modified base vectors from Equation 3.4 and Equation 3.5 has cancelled out the δ functions at time $t = 0$, meaning the final signal only contains information about the time delay separation.

Figure 4.7 illustrates the signal with the Cepstrum and the standard inverse Fourier transform for the case of the two overlapping chirp signals shown on Figure 4.6.

The Cepstrum is computed with 101 equally spaced frequency base vectors ranging from 35 kHz to 95 kHz. As illustrated in Figure 4.7, for the case of the modified inverse Fourier transform (Cepstrum), the ripples at the start are cancelled out. The peak with a time delay of 50 μs corresponds to the time delay of the second echo relatively to the first echo. The peak indicating the second

echo is less masked by the ripples at time $t = 0$. This property is of interest when the echoes are closely spaced.

Finally if there is only one echo in the signal to be processed, as the modified inverse Fourier transform cancels out the ripples, the *spectral block* returns a flat response. The Cepstrum is only performed on the magnitude of the Fourier transform because there is evidence that the output of the peripheral auditory system comprises only the amplitude spectrum over a restricted frequency range [Matsuo and Yano, 2004].

To summarise, BIRA is composed of the *temporal block* from [Matsuo and Yano, 2004] that is composed of a chirplet filterbank to decompose the signal into a spectrogram-like representation. This block is used to determine the time of arrival of the first echo as it is done in [Matsuo and Yano, 2004]. Then, BIRA implements a *spectral block* with the use of the Fourier transform calculated to determine the energy value at each frequency to be used in the inverse process, named Cepstrum by [Matsuo and Yano, 2004]. The base vectors used for the Cepstrum are identical to the one presented by [Matsuo and Yano, 2004]. The design of the BIRA is straightforward when compared to [Matsuo and Yano, 2004] and [Saillant et al., 1993] for the determination of the time of arrival of successive echoes as the aim is not to mimic the bat brain but rather to implement the underlying methods used by the bats.

4.3.4 Output signals formed with the BIRA

By combining the *temporal block* and the *spectral block*, range-profile images are formed. Figure 4.8 illustrates an example with two overlapping chirps. The delay time of the first chirp is determined by the *temporal block* whereas the delay time of the second one is found by the *spectral block*.

First, the sum of the two overlapping chirps is processed by the *temporal block* which output the time of arrival, T_1, of the first chirp. The time T_1 is determined

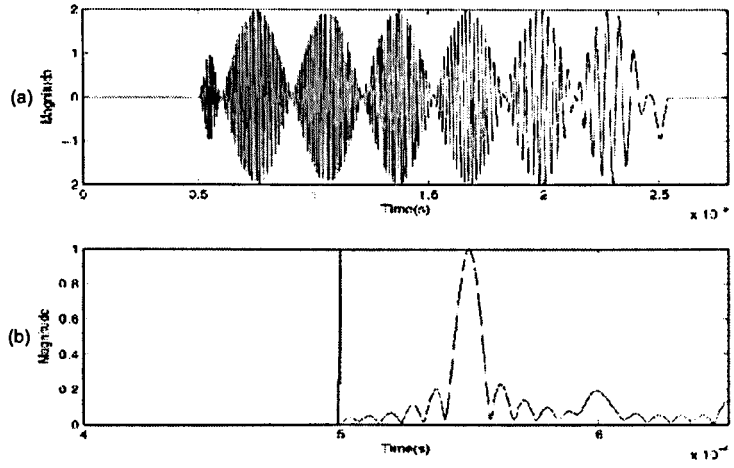

Figure 4.8: **(a):** Two overlapping chirps(500 μs and 550 μs). **(b):** Response from the BIRA.

by the position of the maximum in the sum of the output filters as described in the Section on the *temporal block*. Then the *spectral block* computes the modified inverse Fourier transform on the sum of the two overlapping chirps. The final range-profile image is formed by the juxtaposition of a short pulse to indicate the position of the first chirp at T_1 and the output of the *spectral block*, which corresponds to the modified inverse Fourier transform. The delay of the second echo, T_2, is identified by the position of the maximum in the inverse Fourier transform as illustrated on Figure 4.8(b).

Figure 4.9 illustrates the case when there is only one echo in the signal. It shows that the *temporal block* determines the time of arrival of the first echo, indicated by the short pulse on Figure 4.9(b), and the *spectral block* returns a "flat response" after the short-pulse.

However, the conditions of the design of the algorithm are idealised: echoes have equal amplitudes, echoes are perfect time-delayed copies of emission, and there are only two overlapping echoes. The following Section will analyse the constraints of the algorithm.

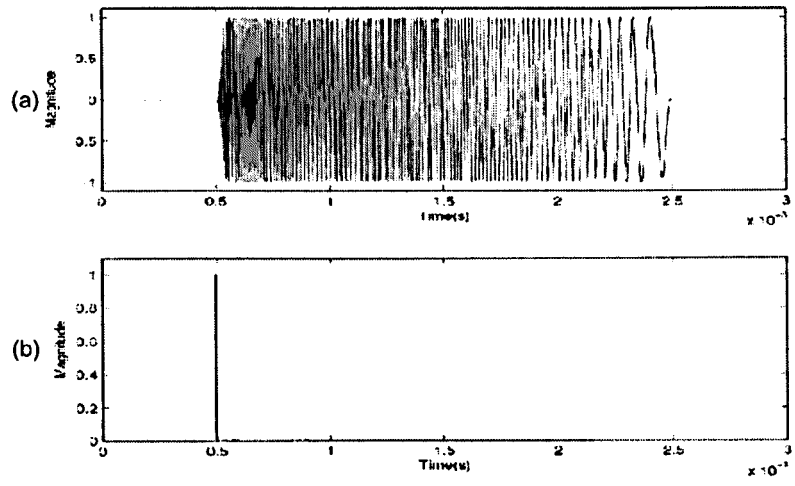

Figure 4.9: **(a):** A single chirp(500 μs). **(b):** Response from the BIRA.

4.3.5 Limits of the spectral block

The BIRA has been illustrated on the case of two overlapping chirp echoes. When the *spectral block* is used to separate more overlapping echoes, spurious peaks appear that do not represent any echoes. Figure 4.10 illustrates the sum of three overlapping chirps and the corresponding plot formed by the BIRA.

With three elements, the *spectral block* forms a plot that contains three peaks and the short pulse. The short pulse corresponds to the delay time, T_1, calculated by the *temporal block*. The output of the *spectral block* contains three peaks where two of the peaks, as expected, correspond to the second and third chirps: peaks at 573 μs and 620 μs. However, a third peak appears earlier at 547 μs. This peak corresponds to the time delay between the second and third chirp (47 μs). This extra peak indicates the existence of an extra echo in the returned signal whereas, in reality there is none. Therefore, the *spectral block* is limited in the number of elements that can be properly separated, as the Cepstrum of more than two echoes outputs an ambiguous range-profile image, containing spurious reflective surfaces. The output is not only dependent on the time delay relative to the first echo but also the time delay between each echo.

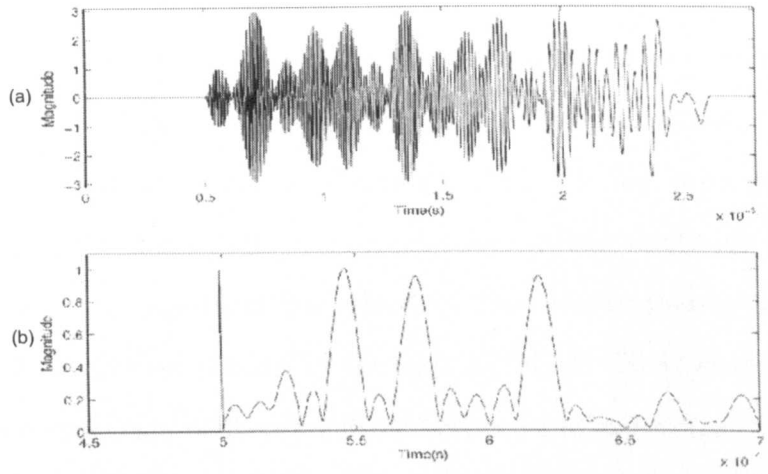

Figure 4.10: **(a):** Three overlapping chirps at 500 μs, 573 μs and 620 μs). **(b):** Response from BIRA.

To illustrates the case of multiple elements, N reflective objects are modelled using the $\delta(t)$ function. Let's consider $h(t)$ the sum of the N objects:

$$h(t) = \sum_{n=1}^{N} r_n \delta(t - \tau_n) \tag{4.28}$$

The magnitude of the Fourier transform of Equation 4.28 is:

$$|H(\omega)|^2 = \sum_{k=1}^{N} r_k^2 + 2 \sum_{i=1}^{N-1} \sum_{j=i+1}^{N} r_i r_j \cos(\omega(\tau_j - \tau_i)) \tag{4.29}$$

Then the Cepstrum from the definition of the BIRA gives:

$$s(t) = 2 \sum_{i=1}^{N-1} \sum_{j=i+1}^{N} r_i r_j \left[\delta(t - \tau_i - \tau_j) + \delta(t - \tau_j - \tau_i)\right] \tag{4.30}$$

In that case, the signal $s(t)$ depends on all the possible time delays. For example, if there are three objects arriving at time T_1, T_2 and T_3, the signal $s(t)$ will contain $\delta(t)$ functions at time $t = T_2 - T_1$, $t = T_3 - T_1$ and $t = T_3 - T_2$. Figure 4.10 illustrates this case. This principle can be extended to multiple echoes and it shows that spurious echoes are generated as the inverse process depends on all

the time delays between the $\delta(t)$ functions. Another limitation of the BIRA is when the chirp signals have different amplitude. For the case of two chirp signals with different amplitude, the depths and peaks in the magnitude of the Fourier transform are going to be altered [Schmidt, 1992]. It has been demonstrated in [Peremans and Hallam, 1998] that a difference in the amplitude between the two chirps make the algorithm less robust to noise contamination and scale the amplitude of the inverse process in the spectral block. Howevever, it does not affect the determination of the time delay between the two chirps.

4.3.5.1 Discussions

For the case of two overlapping echoes, the BIRA can discriminate echoes separated as close as 6 μs, i.e around 2 mm in air when considering the highest frequency (100 kHz). This resolution corresponds to 0.6λ. The discrimination resolution is equivalent to the computational models of [Saillant et al., 1993] and [Matsuo et al., 2001]. This resolution is theoretically higher than the actual resolution limit set by the inverse of the frequency bandwidth contained in the signal, for an optimum receiver at a given Signal-to-Noise Ratio (SNR), as defined by a matching filter. The resolution capability for a matching filter is set by the half width of the filter output. The half width time duration has been measured to be equivalent to the inverse frequency bandwidth contained in the signal [Barton, 1997]. Therefore for a signal containing a frequency bandwidth of 100 kHz, the inverse calculation is 10 μs. BIRA with a resolution of 6 μs overcomes this limit. The algorithm also offers the advantage of straightforward implementation that does not require priori knowledge of the device impulse response.

The BIRA has been applied on idealistic echoes as it is considered that the received echoes are perfect copies of the emission. However, it would not be the case in practical applications. The ultrasonic transducer, the propagation medium and the object being image itself will modify the phase and bandwidth

of the echoes.

Moreover, the BIRA has been designed using the same frequency bandwidth as the FM bats. To be exploitable, the methods must be useable on different frequency bandwidths.

4.4 Conclusion

This Chapter has presented some inversion processes used to enhance axial resolution alongside their characteristics.

An algorithm based on computational models of the bat auditory system was then introduced and designed with the aim of enhancing the axial resolution. Its behaviour under idealistic conditions has been presented. The BIRA was shown to perform well for the case of two quite idealistic overlapping echoes with the limits detailed previously. Despite those current restrictions, the following Chapter investigates the performance of this algorithm when the influence of the transducer and the attenuation in the medium are considered, two factors that must be considered for any practical ultrasonic imaging system.

Chapter 5

Evaluation of the BIRA

5.1 Introduction

The performance of the BIRA has been quantified on idealistic signals. The purpose of this Chapter is to evaluate the robustness of the algorithm in a software modelled environment that includes artefacts occurring in engineering applications. The attenuation of air, the limited bandwidth of the broadcasting device and other parameters may alter the processes of the algorithm.

This Chapter will describe the methods used to evaluate the algorithm when air attenuation is introduced. An accurate software model has been used to evaluate the performance of the algorithm. Then the frequency bandwidth requirement for the algorithm is evaluated. Finally, the robustness to noise of the algorithm is assessed.

5.2 Evaluation methods

Two parameters have been evaluated to quantify their influence on the performance of the algorithm: air attenuation and transducer Fractional BandWidth (FBW). Air attenuation is evaluated on the algorithm with the use of a software model developed by [Benny and Hayward, 2000] based on the work from [Bass et al., 1972]. The air attenuation model is used to calculate the frequency attenuation dependence of acoustic waves when propagating through air. The second parameter being analysed, is the limited bandwidth of the broadcasting device, i.e. the transducer.

5.2.1 Air model

This Section outlines a method that has been implemented to predict and measure the acoustic radiation generated by ultrasonic transducers operating into air in continuous wave mode.

The air attenuation simulation model from [Benny and Hayward, 2000] considers a homogeneous medium for the acoustic field generated by a planar transducer. The computation of the acoustic pressure is calculated from the Rayleigh integral which includes frequency dependent air attenuation coefficients. A continuous wave at an angular frequency ω will undergoes frequency dependent attenuation introduced by the medium. The representation of the acoustic wave $v(R,t)$ can be modelled by Equation 5.1:

$$v(R,t) = a\exp(-\alpha R + j\omega t) \tag{5.1}$$

where R is the range to the source of emission, a is the complex amplitude, ω the angular frequency and α the frequency dependent medium attenuation coefficient. The attenuation coefficient is a complex quantity containing the loss element generated by "classical" losses. The model from [Benny and Hayward, 2000] has also introduced losses from thermal and viscous losses, and molecular energy interchanges between the gaseous components of air. The addition of the last parameters improves the accuracy of the model to real physical phenomena. The attenuation coefficient is decomposed as described in Equation 5.2:

$$\alpha = \alpha_{cr} + \alpha_{vib,O} + \alpha_{vib,N} \tag{5.2}$$

where α_{cr} represents the "classical" air attenuation coefficient, $\alpha_{vib,O}$ and $\alpha_{vib,N}$ are vibration loss coefficients due to oxygen and nitrogen. By introducing the molecular loss, the field structure of devices could be predicted where simple, closed-form classical techniques produce inadequate data. The coefficient α depends on air temperature, pressure and frequency in various degrees.

Before giving an expression for the three coefficients, it is required to define constant parameters of standard pressure and temperature such as $P_0 = 1$ bar and $T_0 = 293.15$ K and the triple point of water, $T_{01} = 273.16$ K, corresponding to

the temperature at which water can coexist in the three phases of gas, liquid and solid. The methodology derived from the work by [Bass et al., 1972], consisting of four calculation steps, leads to the determination of the attenuation coefficient α at a frequency f in *Hertz*, a temperature T in *Kelvin degree* and a pressure P in *bar*. P_{Sat} is the saturation pressure.

1- First, the saturation pressure ratio $\frac{P_{Sat}}{P_0}$ is calculated from the expression:

$$\log_{10}(\frac{P_{Sat}}{P_0}) = 10.79586(1 - \frac{T_{01}}{T}) + 1.50474 \times 10^{-4} \times (1 - 10^{8.29692(\frac{T}{T_{01}}-1)}) + 0.42873 \times 10^{-3}(10^{4.76955(1-\frac{T_{01}}{T})} - 1) - 2.2195983$$

2- Then the water mole fraction, $h(\%)$ is derived from the relative humidity h_r and relevant pressure ratios as follows:

$$h = h_r \frac{P_{Sat}}{P}$$

3- Oxygen and Nitrogen relaxation frequencies $f_{r,O}$ and $f_{r,N}(\mathrm{Hz})$, respectively, are calculated from:

$$f_{r,O} = \frac{P}{P_O}(24 + (4.04 \times 10^4 h(\frac{0.02 + h}{0.391 + h})))$$

$$f_{r,N} = \frac{P}{P_O}\sqrt{\frac{T_0}{T}}(9 + (280h \exp[-4.17(\frac{T_0}{T}^{-\frac{1}{3}} - 1)]))$$

4- The individual attenuation components may now be calculated from the following relationships:

$$\alpha_{cr} = 1.84 \times 10^{-11} f^2 \frac{P}{P_0}\sqrt{\frac{T}{T_{01}}}$$

$$\alpha_{vib,O} = f^2 \frac{T_0}{T}^{\frac{5}{2}} (1.278 \times 10^{-2} \frac{exp[\frac{-2239.1}{T}]}{f_{r,O} + \frac{f^2}{f_{r,O}}})$$

$$\alpha_{vib,N} = f^2 \frac{T_0}{T}^{\frac{5}{2}} (1.068 \times 10^{-1} \frac{exp[\frac{-3352}{T}]}{f_{r,N} + \frac{f^2}{f_{r,N}}})$$

The attenuation coefficient α_{cr} is calculated by setting the frequency f in *Hertz*, the pressure P in *bar* and the temperature T in *Kelvin degree*. The following attenuation coefficients $\alpha_{vib,O}$ and $\alpha_{vib,N}$ are calculated for a given frequency f in *Hertz* at a temperature T in *Kelvin degree*. The overall value of α can now be estimated by summing the three idependent coefficients and the sum is used to determine the attenuation in air at a specific frequency. Then Equation 5.2 can be used to calculate the attenuation coefficients in air for any temperatures, pressure and humidity conditions. For the purpose of the evaluation, the attenuation coefficients at each frequency for a given range have been computed and applied to the signal. Generally, the attenuation in air of an acoustic wave is more significant on the higher frequency components. To illustrate all of this, the air attenuation model developed by [Benny and Hayward, 2000], is applied on a LFM chirp signal sweeping downward from a frequency of 135 kHz to 5 kHz over a period of 1 ms. The results on the chirp in the time domain and frequency domain are illustrated on Figure 5.1. As illustrated, for a range of 2 meters, the attenuation is more significant on the higher frequency than the lower frequency.

The non-linearity of the attenuation in air is illustrated on Figure 5.2 for six ranges of: 10 cm, 25 cm, 50 cm, 1 m, 2 m and 10 m. It shows the significant attenuation for close ranges from a bat point of view and how the higher frequencies are much more attenuated. For example, at a range 10 m, frequency components above 50 kHz are negligible. This has signficant consequences for the BIRA.

The implementation of the air attenuation model is performed in the frequency

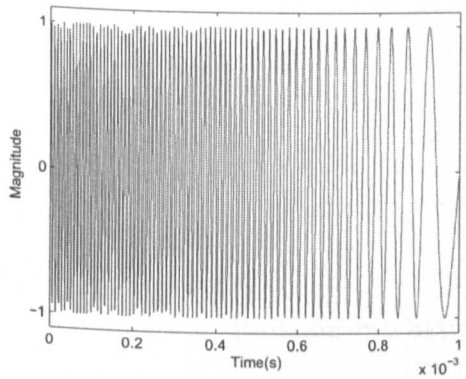

(a) Original LFM chirp signal

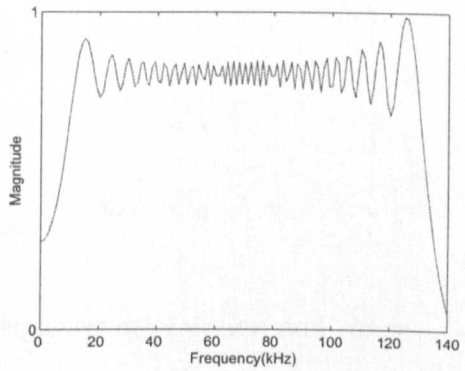

(b) Fourier transform of Original LFM chirp signal

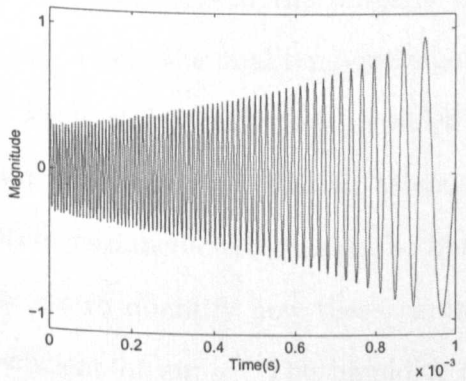

(c) Attenuated LFM chirp signal

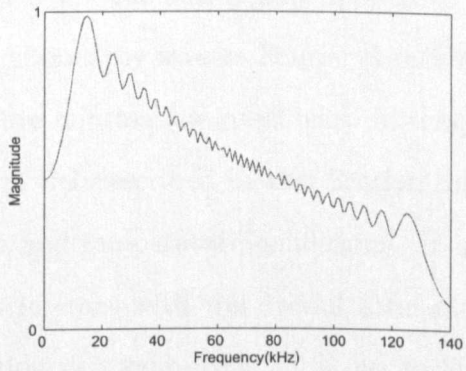

(d) Fourier transform of attenuated LFM chirp signal

Figure 5.1: Frequency dependence of air attenuation

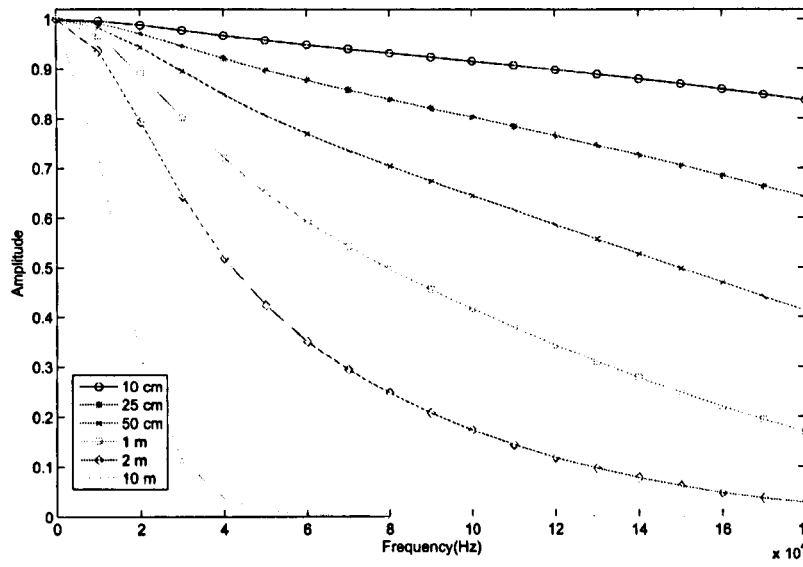

Figure 5.2: Relationship between frequency attenuation and range

domain. First, the Fourier transform of the signal is calculated. Then the attenuation coefficients at the range of the signal are calculated and applied to the signal. Then, the final temporal signal is obtained by inverse Fourier transform.

The weather conditions in which bats are hunting for insect vary in temperature and humidity. The air attenuation model described in this Section incorporate parameters to change the humidity and temperature conditions. It is of interest to quantify how these parameters interact with the overall attenuation coefficient of air α. The humidity condition can vary from 20 % up to 80 % depending on the continent where the bat is. The change in the attenuation coefficient α for such a range has been quantified for three frequencies of 5 kHz, 70 kHz and 135 kHz. They correspond to the starting frequency of the chirp, the centre frequency and the ending frequency. As shown on Figure 5.3, the attenuation increases as the humidity increases and the attenuation stays significant for the range of humidity.

The relative error in temperature is also going to alter the overall attenuation

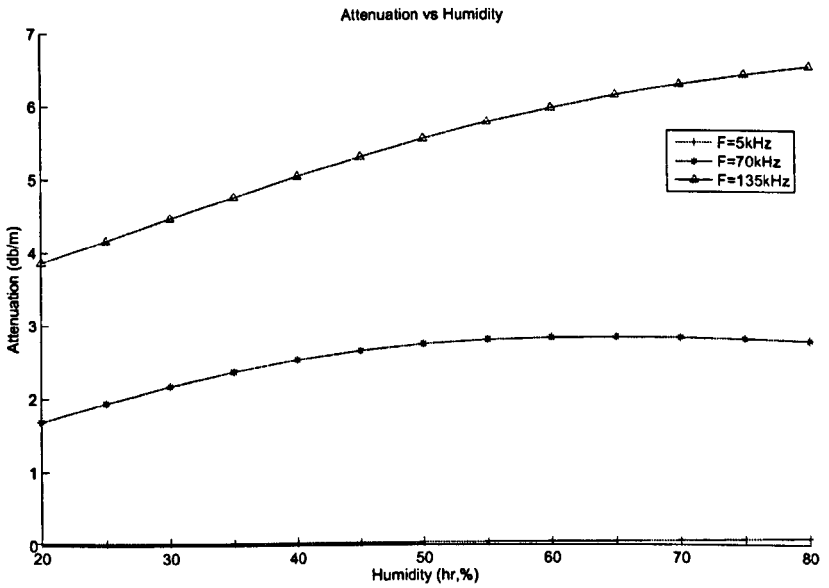

Figure 5.3: Relationship between frequency attenuation and humidity

coefficient α. For this purpose, the changes in the attenuation coefficient α for a range of temperature from 5 °C to 30 °C has been computed for the three frequencies of 5 kHz, 70 kHz and 135 kHz. For an increase in temperature, the attenuation in air is also increasing as shown on Figure 5.4. Even for low temperature, the attenuation remains significant.

For the purpose of the simulations, the parameters of the air model have been set to a pressure of 1 atmospheric, the temperature at 20 °C and the humidity at 45 %. These conditions are representative of the one in which the bats are hunting for flying prey.

5.2.2 Model of transducer frequency response

When broadcasting or receiving a signal through an ultrasonic transducer, it is altered by the impulse response of the device. The frequency response of the transducer is an important characteristic as it limits the signal that can be transmitted (or received) by the device. The transducer characteristic can be

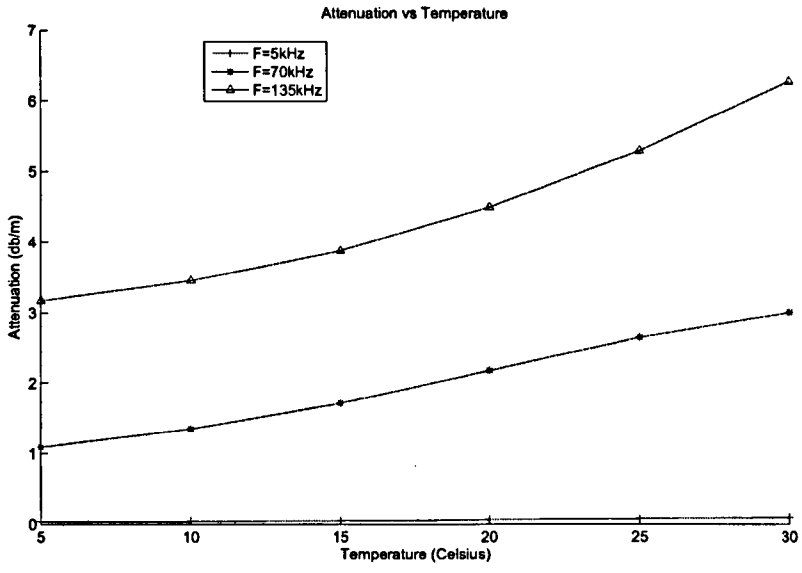

Figure 5.4: Relationship between frequency attenuation and temperature

defined by its impulse response and the corresponding frequency response will limit the available chirp bandwidth.

For the purpose of this Section the transducer frequency response is considered with a centre frequency where the sensitivity is decaying in a "bell-shape" form as the frequency moves apart from the centre frequency of the transducer.

A straightforward method is implemented to model the transducer frequency response. It is modelled as a first approximation with a band-pass filter where the -3 dB points around the centre frequency represents the frequency bandwidth of the transducer named as the FBW. The FBW is defined by Equation 5.3:

$$FBW = \frac{Bandwidth}{F_{Centre}} \tag{5.3}$$

where $Bandwidth$ is the -6 dB cut-off frequency bandwidth and F_{centre} is the centre frequency of the transducer. The FBW is a ratio that quantifies the frequency bandwidth of the transducer.

The transducer frequency response was modelled using a Butterworth band-

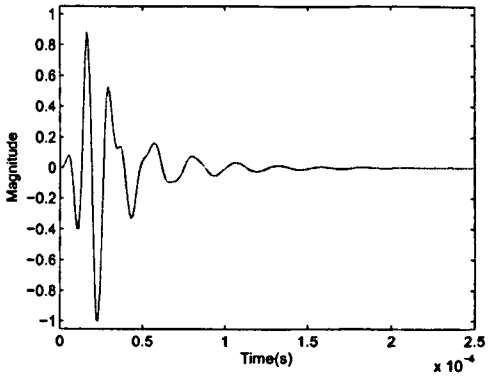

(a) Impulse response

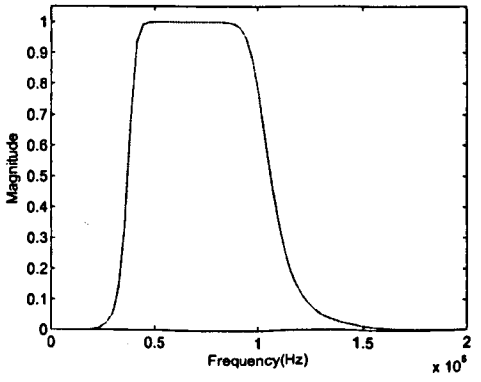

(b) Frequency response

Figure 5.5: Butterworth filter for a $FBW = 90\%$

pass filter as they are characterized by a magnitude response that is maximally flat in the bandpass [Selesnick and Burrus, 1998]. It was designed to simulate a range of FBW to quantify the requirement for the algorithm. The impulse response of the Butterworth filter is then convolved with the chirp signal to simulate the constraints introduced by the transducer.

The impulse response and the corresponding frequency spectrum for a Butterworth filter with a simulated FBW of 90 % are illustrated on Figure 5.5. The responses from Figure 5.5 are calculated with a centre frequency of 70 kHz. The two frequencies at -6 dB are calculated from the centre frequency and the required FBW.

The two methods presented here, i.e. the air attenuation model and the transducer model, are then applied to evaluate the performance of the BIRA. The evaluation of the role of air attenuation and transducer bandwidth is done independently.

5.3 Influence of air attenuation

This Section presents the results from the simulation of the BIRA when attenuation in air is introduced. The aim is to evaluate the robustness of the algorithm when a more realistic signal is processed. Both the *Temporal block* and *Spectral block* are being assessed to quantify their behaviour.

5.3.1 Performance of the *Temporal block*

The air attenuation model is firstly applied on the *Temporal block*. This block is designed to determine the time of arrival of the first element in a sum of overlapping echoes.

The software development have been implemented in Matlab©. The simulation of the air attenuation is realised without considering the frequency limited bandwidth of the transducer. The *Temporal block* is using 101 Gaussian filters ranging from 35 kHz up to 95 kHz. A single LFM chirp signal is processed by the *Temporal block*. It is a LFM chirp signal sweeping from 5 kHz up to 135 kHz on a period of 1 ms. To create variability in the data, the simulations were performed with a relatively low noise level, with a SNR = 100 dB.

The role of air attenuation on the performance of the *Temporal block* is evaluated on four distances of 10 cm, 50 cm, 1 m and 10 m. The velocity in air is of $c = 340\ m/s$ and as the acoustic waves have to travel forward and back, the time of flight is calculated on twice the distance. Therefore these distances respectively correspond to a time of arrival of 580 μs, 2.9 ms, 5.8 ms and 58 ms in air. The

air attenuation coefficients are calculated with the air model presented previously. The air attenuation coefficients are calculated in the frequency domain and then applied to the Fourier transform of the chirp signal. The final time signal is obtained by inverse Fourier transformation of the air attenuated Fourier signal. This final time signal is the one processed by the *Temporal block*.

To evaluate the performance in determining the time of arrival of the echo, five hundred simulations were run with for each simulation Gaussian distributed white noise was added. As the time of arrival of the echo is determined by the position of the maximum value, for each simulation, the position has been recorded. The distributions of the position are displayed to evaluate the relative error to the theoretical values in determining the time of arrival.

The histograms of the results is shown on Figure 5.6 for the four distances. Each bar on the Figure 5.6 show the corresponding number of echoes determined with a relative error value indicated on the x axis. The histograms of four distances show the relative error of the time of arrival when compared to the theoretical time of arrival. It shows that for the 500 simulations, all the echoes are determined properly as the relative error is zero.

The matching between the theory and the simulations lead to the conclusion, that the attenuation in air does not impair the behaviour of the *Temporal block*. The time of arrival of a single chirp can be determined as long as there is some frequency component of the chirp. As the *Temporal block* is designed to split the chirp signal into subbands and the air attenuation does not modify the time of arrival of the frequencies, the *Temporal block* remains robust with respect to the attenuation in air.

5.3.2 Performance of the *Spectral block*

The performance of the *Spectral block* when air attenuation is introduced is then quantified. The simulations are conducted in the same conditions as for

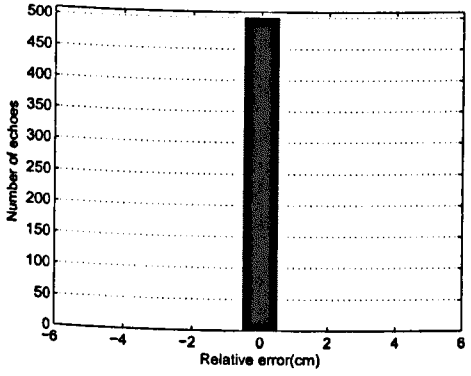

(a) Histogram for a distance of 10 cm

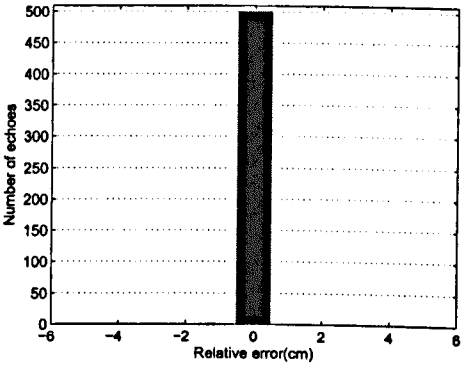

(b) Histogram for a distance of 50 cm

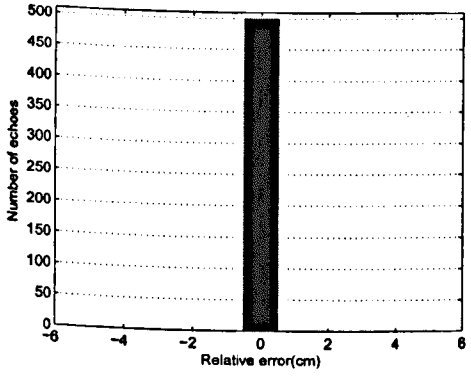

(c) Histogram for a distance of 1 m

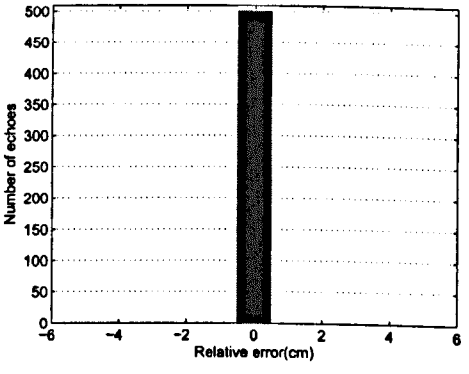

(d) Histogram for a distance of 10 m

Figure 5.6: Robustness to air attenuation of the *Temporal block*.

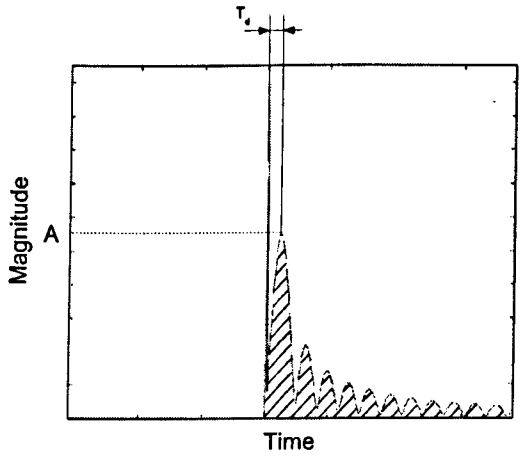

Figure 5.7: Illustration of the resolution measurements.

the *Temporal block*, i.e. with no consideration of the transducer bandwidth, in a noise free environment and with a single chirp signal. The *Spectral block* has been evaluated on five ranges: 5 cm, 25 cm, 50 cm, 1 m and 10 m that correspond to time of arrival of respectively 290 μs, 1.4 ms, 2.9 ms, 5.8 ms and 58 ms in air.

The attenuation coefficients are similarly computed in the frequency domain and the time signal are generated by inverse Fourier transform. The results for the five ranges are presented on Figure 5.8. It shows that sidelobes are introduced by the *Spectral block* when air attenuation is considered. The level of sidelobes increases with the range as the attenuation does.

To quantify the loss in resolution, three measurements are realised on the signals generated by the *Spectral block*. The first measurement, named T_d, corresponds to the time delay between the first short pulse and the maximum value of the main peak as illustrated on Figure 5.7. It is used to quantify the limit of separation of closely spaced objects. The second measurement consists of measuring the highest level of sidelobes generated in the *Spectral block*, illustrated by the value of A on Figure 5.7. Finally, the last measurement is to calculate the area under the sidelobes, as illustrated by the dashed line on Figure 5.7, to quantify their level on the signal formed by the *Spectral block*.

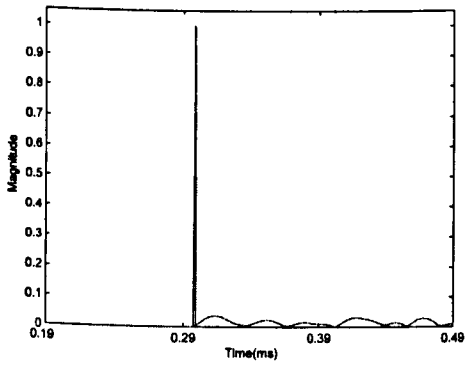

(a) Algorithm for a range of 5 cm

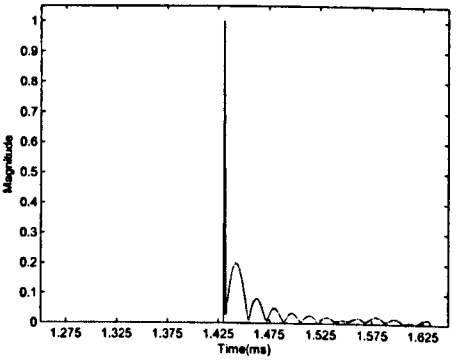

(b) Algorithm for a range of 25 cm

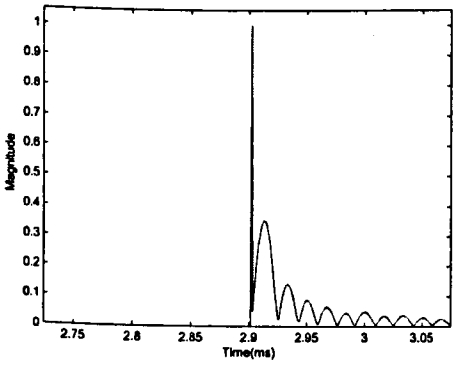

(c) Algorithm for a range of 50 cm

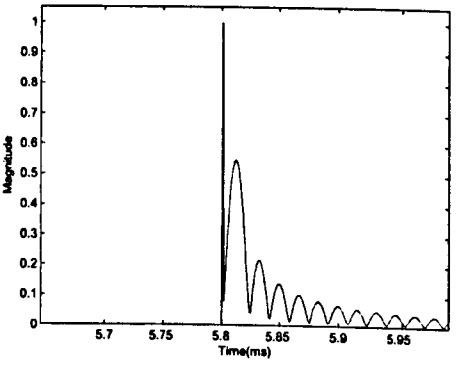

(d) Algorithm for a range of 1 m

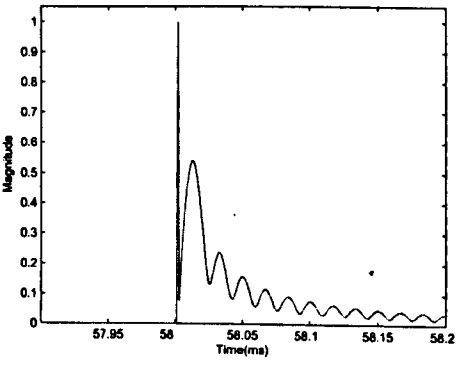

(e) Algorithm for a range of 10 m

Figure 5.8: Robustness to air attenuation of the *Spectral block*.

Range(m)	Sidelobes area(Dashed lines)	Sidelobe level(A)	$T_d(\mu s)$
0.05	0.06	N/A	N/A
0.25	0.40	0.21	12
0.5	1.29	0.33	12
1	4.00	0.53	12
10	4.66	0.54	12

Table 5.1: Resolution measurements of the *Spectral block*

For a really close range (5 cm), the sidelobe level is negligible and it is not possible to quantify T_d as it is not possible to identify the mainlobe as shown on Figure 5.8(a). The results shown on Table 5.1 indicate that when the range is increasing the sidelobes level and area significantly rise. The delay time, T_d, measured of about 12 μs indicates the closest resolvable lobe. Any object within this time delay will not be resolvable as it would be masked by the spurious mainlobe. When compared to the idealistic case, where the resolution was measured of 6 μs, it is twice the value but also above the theoretical resolution set by the inverse of the bandwidth of the chirp signal, i.e. 10 μs. The level of the sidelobes increases up to a value of 0.54 for a range of 10 meters as shown on Table 5.1, it has a significant impact as this strong spurious lobe could be interpreted as an actual object in the range-profile image.

The BIRA has been designed with the consideration of a flat frequency spectrum to determine the following echoes from the frequency spectrum. The inverse mechanism based on the Gaussian filters from [Matsuo et al., 2004] or the original *voting mechanism* from [Saillant et al., 1993] did not mention any requirement on the frequency spectrum. However for an appropriate reconstruction of the signal into the time domain, the frequency spectrum has to be preserved. When air attenuation is introduced, the non-linear frequency attenuation impairs the inverse process. The modified base vectors, presented in Chapter 4, do not cancel out anymore the sidelobes at time $t = 0$ of the cesptrum. The inverse process is based on the location of peaks and notches in the frequency spectrum. Therefore when

air attenuation is introduced, the strength of the peaks are altered and it alters the inversion process. The theoretical inverse process considered the frequency spectrum of the chirp signal as constant over the frequency spectrum, however when attenuation in air is introduced, this condition is no longer valid.

5.4 Fractional Bandwitdh requirement

In order to develop applications for the BIRA, it is of interest for the design of a practical transducer to define the requirement in term of usable frequency bandwidth.

The next set of simulations consisted of evaluating the required FBW. As previously presented, a band-pass filter was used to simulate the transducer impulse response. The simulations were conducted for a single LFM chirp. Air attenuation was not included in the simulations as the purpose was to independently quantify the bandwidth requirement to use the algorithm.

The band-pass filter is set to simulate three FBW of 20 %, 70 % and 160 %. The corresponding impulse and frequency response are shown on Figure 5.9. The FBW is calculated from the centre frequency of the chirp of 70 kHz. As shown on Figure 5.9, when the frequency bandwidth is increased, the impulse response of the modelled transducer is sharpened, as expected.

The chirp signal is convolved with the impulse response of the modelled transducer impulse response. The result of the convolution is then processed by the BIRA. The output signals from the BIRA are shown on Figure 5.10. For a FBW of 20 % when the band-pass filter is applied to the chirp signal, the chirp is narrowed around the centre frequency of 70 kHz. When the FBW reaches 160 %, the chirp signal is only altered at the beginning and the end.

Concerning the performance of the BIRA, for a FBW of 20 %, the limited bandwidth of the transducer model introduced significant sidelobes in the *Spectral*

block of the algorithm. When the FBW is progressively increased to a FBW of 70 %, the sidelobes are still present in the *Spectral block* but with a lower level. Finally, when the FBW reaches 160 %, the BIRA returns a "flat response" similar to the one observed under ideal conditions.

The simulations show that the FBW has a significant impact on the performance of the algorithm as illustrated on Figure 5.10. A FBW below 160 % introduces sidelobes in the *Spectral block* when only one chirp signal is present. When the signal is filtered by the band-pass filter, the "flat frequency" spectrum from the LFM chirp signal is weighted. However, the performance of the inversion process (Cepstrum) used in the *Spectral block* is dependent on the frequency content. The simulations show that if the frequency spectrum is not "constant" over the frequency covered by the chirp signal, sidelobes are introduced, degrading the performance of the algorithm. When the FBW reaches a value of 160 %, the Cepstrum is applied on a frequency spectrum that is not weighted by the band-pass filter and therefore the *Spectral block* reconstructs an appropriate range profile.

Concerning the influence on the *Temporal block* of the change in the FBW, the change in the FBW does not alter the time of arrival of each frequency component therefore the evaluation method used in the *Temporal Block* stays robust. As stated previously, the time of arrival of a chirp signal can be determined as long as there is some frequency component of the chirp signal. Figure 5.10 shows the changes occurring in the chirp signal starting at a time of 500 μs. For the three levels of FBW, the time of arrival of the chirp determined by the *Temporal block* is of 500 μs, as indicated by the short-pulse. It shows that the *Temporal block* stays robust to the changes in FBW and in the frequency bandwidth of the chirp signal.

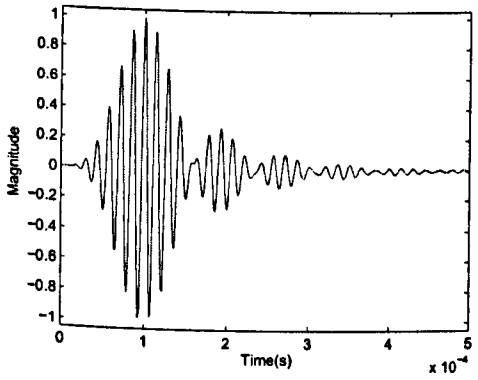

(a) Impulse response for $FBW = 20\%$

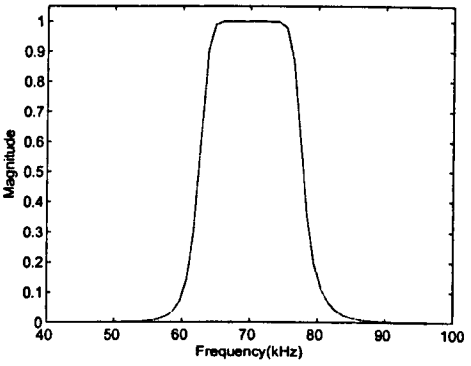

(b) Frequency response for $FBW = 20\%$

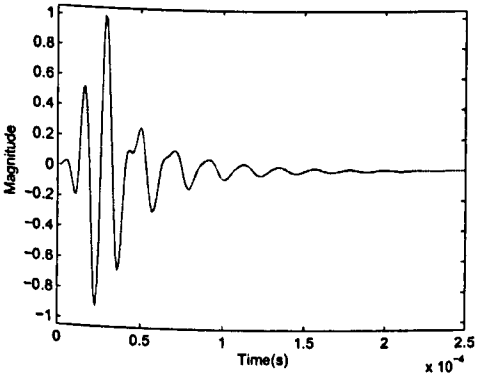

(c) Impulse response for $FBW = 70\%$

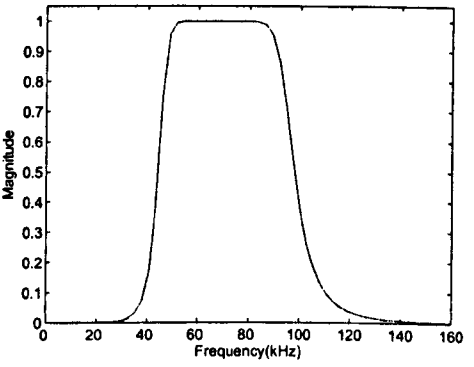

(d) Frequency response for $FBW = 70\%$

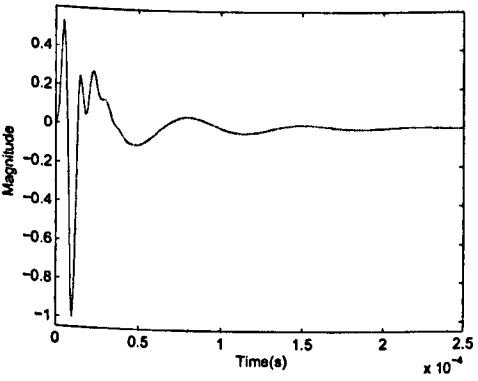

(e) Impulse response for $FBW = 160\%$

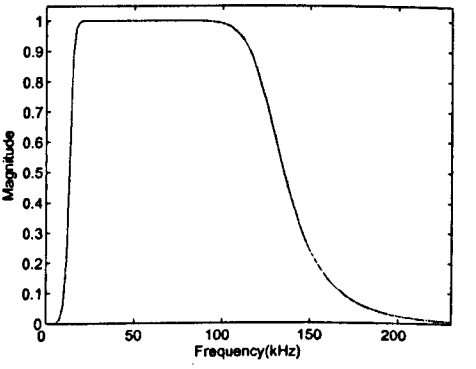

(f) Frequency response for $FBW = 160\%$

Figure 5.9: Set of modelled transducer responses.

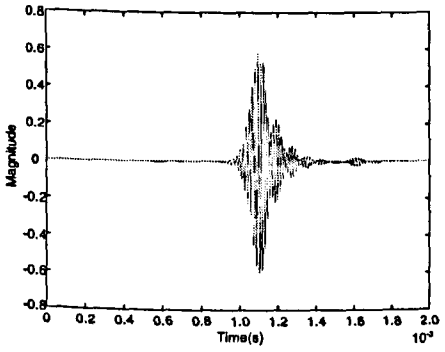

(a) Chirp signal for $FBW = 20\%$

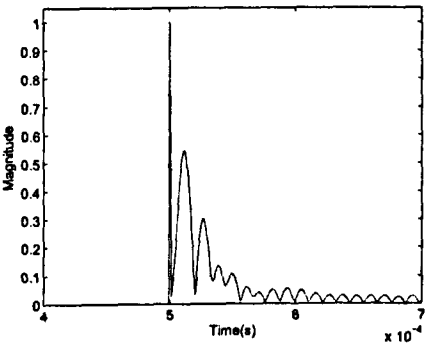

(b) Output signal for $FBW = 20\%$

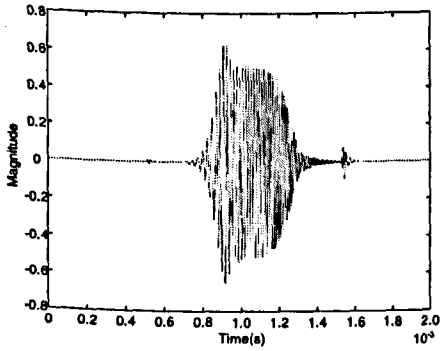

(c) Chirp signal for $FBW = 70\%$

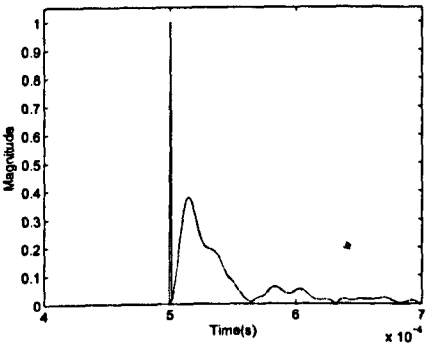

(d) Output signal for $FBW = 70\%$

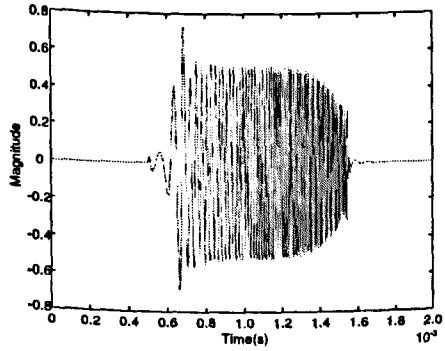

(e) Chirp signal for $FBW = 160\%$

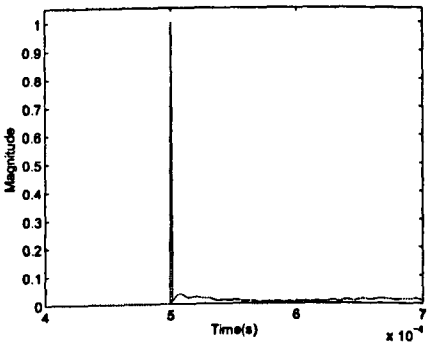

(f) Output signal for $FBW = 160\%$

Figure 5.10: Output signals from the BIRA for a set of FBW.

5.5 Noise robustness

The final set of simulations considers the robustness of the algorithm in the presence of noise. The performance of the *Temporal block* is quantified in the determination of the range of a single chirp. For the purpose of the comparison, the performance is compared to the well-established cross-correlation technique as this method is based on matched filter theory that is the optimal solution to obtain the best SNR for a known signal. The cross-correlation is used as a method to indicate the range of the chirp.

5.5.1 Simulation on a single chirp

In order to compare the performance of the two methods, i.e. cross-correlation and the *Temporal block* of the BIRA, to determine the range of a single element, a selection criteria has been introduced. This criteria aims to determine if there is only one chirp present in the signal, and strictly only one. As the two methods, the cross-correlation and the *Temporal block* both indicate the time of arrival of the echo by the position of a maximum value; it has been considered that there is only one chirp if there are no other peak values higher than 50 % of the maximum value. To illustrate the principle, Figure 5.11 shows the results from the cross-correlation of a chirp signal, one in noise-free condition (Figure 5.11(a)) and another one with contaminative noise (Figure 5.11(b)). The cross-correlation in noise-free condition returns a main peak at the 0 Lag, as shown on Figure 5.11(a). The presence of noise alters the cross-correlation output by displaying multiple peaks, as shown on Figure 5.11(b). From the definition of only one chirp, as stated previously, the plot without noise on Figure 5.11(a) is considered as having only one chirp or echo as there is only one peak whereas the other as more than one peak higher than 50 % of the maximum value. The range of the echo is determined in both methods by the position of the maximum value in the signal.

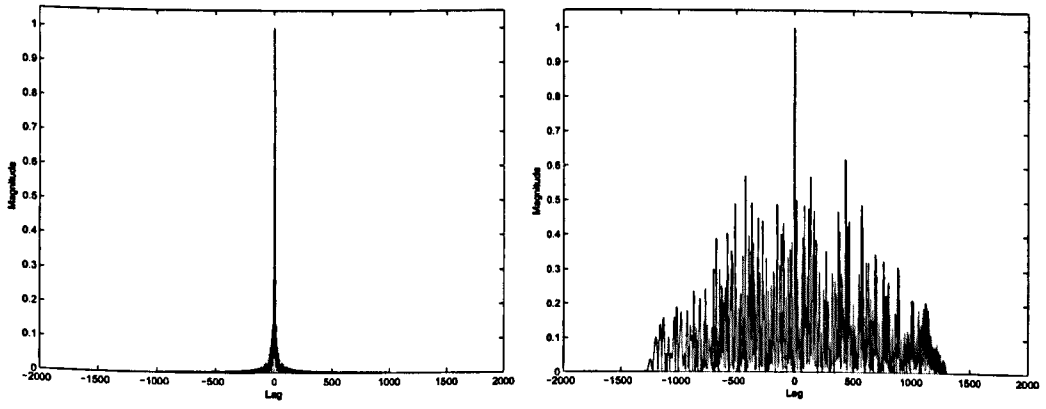

(a) Signal considered with only one echo (b) Signal not considered with only one echo

Figure 5.11: Illustrations of the criteria of a unique echo.

The simulations of noise level are conducted without considering the limited bandwidth of the transducer. However, to preserve practical accuracy, the influence of the air attenuation is considered. Four levels of SNR are simulated, of 10 dB, 0 dB, -20 dB and - 30 dB for three ranges of 10 cm, 50 cm and 10 m (Corresponding to time of arrival of 580 μs, 2.9 ms and 58 ms in air as the velocity in air is of 340 m/s and considering the wave as to travel forward and backward). For each case, five hundred simulations are run where the time of arrival and the criteria of existence of a single chirp are recorded. The SNR level is calculated over the full signal by integrating the energy contained in the original signal. Then the noise energy required reaching the SNR level is added to the signal.

Figures 5.12 to Figure 5.19 show the noisy chirp signal alongside the output signals for the cross-correlation and the *Temporal block*. It illustrates how the signals are altered with the introduction of noise. For level of SNR of 10 dB and 0 dB, the range of the single echo is clearly identified by the location of the maximum value, either in the cross-correlation as illustrated on Figure 5.12(c)(d), Figure 5.13(b), Figure 5.14(c)(d) and Figure 5.15(b). The maximum value for the output of the *Temporal block* is clearly identified on Figure 5.12(e)(f), Figure 5.13(c), Figure 5.14(e)(f) and Figure 5.15(c).

When the SNR level is of -20 dB, the cross-correlation still contains a peak

value for the ranges of 10 cm and 50 cm as shown on Figure 5.16(c)(d). For a chirp signal at a range of 10 m, as shown on Figure 5.17, the output of the cross-correlation does not indicate anymore the range by a peak value (Figure 5.17(b)). The response is masked by the level of noise. The outputs from the *Temporal block* still indicates the range for the three ranges as shown on Figure 5.16(e)(f) and Figure 5.17(c). However, the unicity of the peak value is not preserved, making it difficult to clearly identify the time of arrival of the chirp as any other peaks in the output of the *Temporal block* could be interpreted as another chirp.

Finally, when the level of SNR reaches -30 dB, both methods fail to indicate the range as there is no clearly identified peak values, as shown on Figure 5.18 and Figure 5.19.

Overall the performance of the cross-correlation if better than the *Temporal block* however the *Temporal block* stays robust to significant levels of noise.

5.5.1.1 Noise robustness with a single chirp

The criterion of existence of only one chirp, as defined previously, is relevant to the robustness of the algorithm with respect to contaminating, uncorrelated noise. For a level of SNR varying from 10 dB down to -30 dB, it has been recorded for the five hundred simulations when the processed signal was considered as containing only one chirp or not. The percentage of signal considered as containing only one chirp has been calculated. The results for the three distances are shown on Figure 5.20.

For the range of 10 cm, the number of returns considered as containing only one element is similar. The cross-correlation has better performance when the SNR level reaches -20 dB.

For the higher ranges of 50 cm and 10 m, where the attenuation in air is more significant, the cross-correlation gives better results than the *Temporal block*. These results show that the *Temporal block* is not as optimal as the cross-

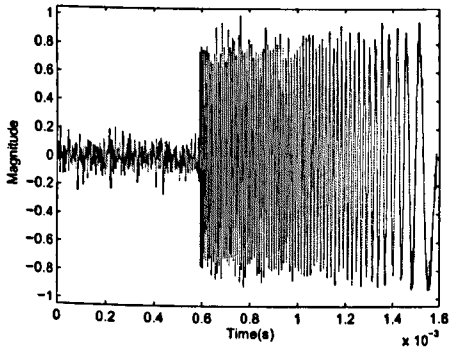

(a) Chirp signal at 10 cm

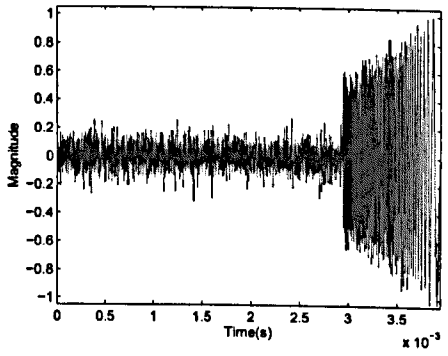

(b) Chirp signal at 50 cm

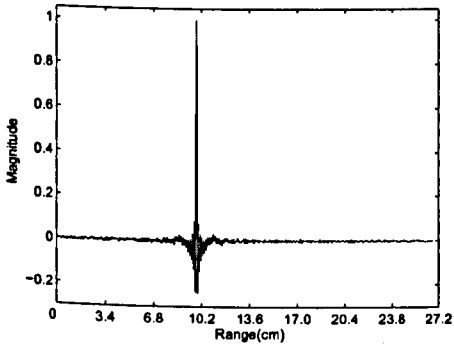

(c) Cross-correlation output at 10 cm

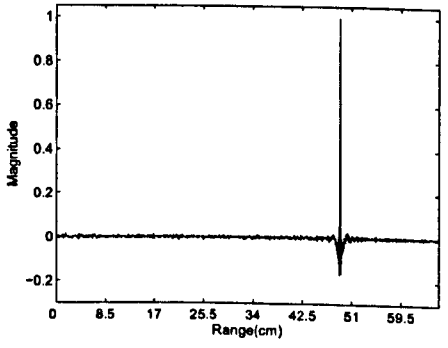

(d) Cross-correlation output at 50 cm

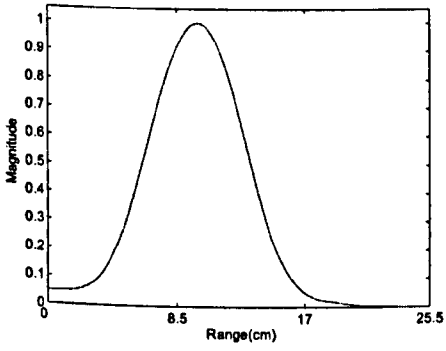

(e) *Temporal block* output at 10 cm

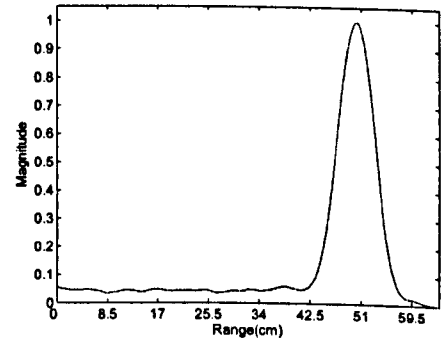

(f) *Temporal block* output at 50 cm

Figure 5.12: Signals for a SNR level of 10 dB.

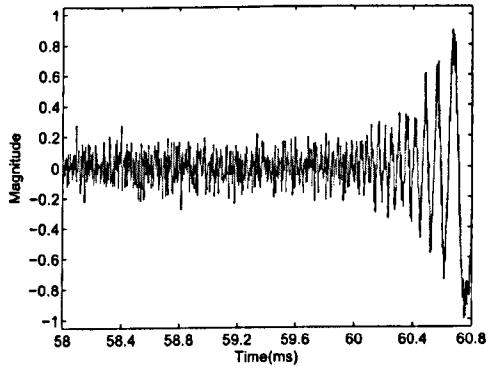

(a) Chirp signal at 10 m

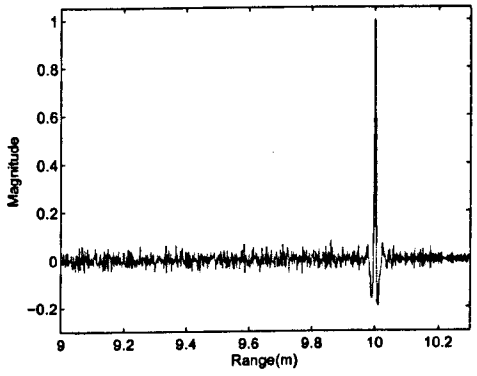

(b) Cross-correlation output at 10 m

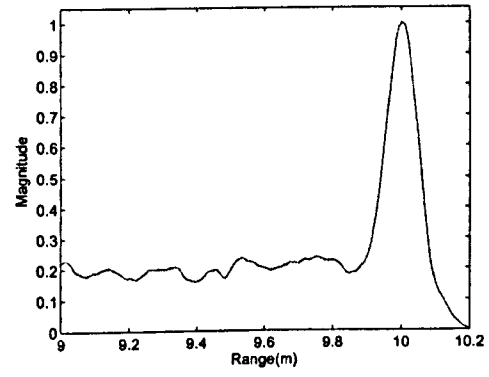

(c) *Temporal block* output at 10 m

Figure 5.13: Signals for a SNR level of 10 dB for a range of 10 meters.

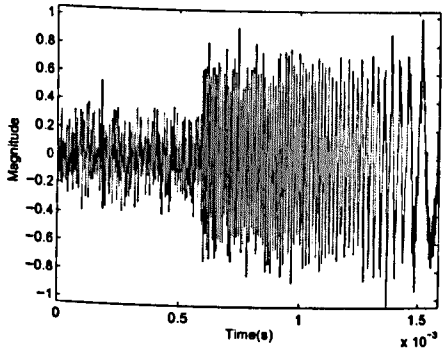

(a) Chirp signal at 10 cm

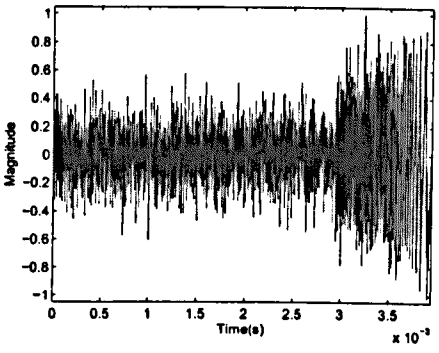

(b) Chirp signal at 50 cm

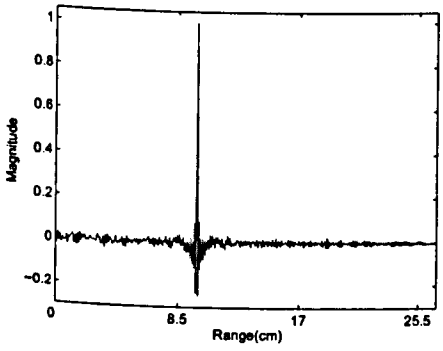

(c) Cross-correlation output at 10 cm

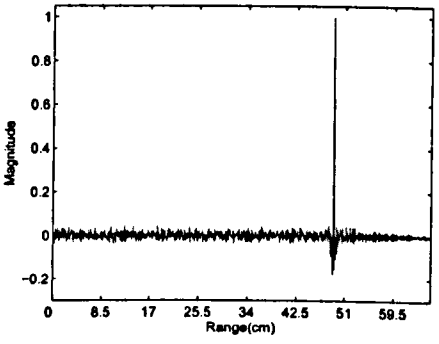

(d) Cross-correlation output at 50 cm

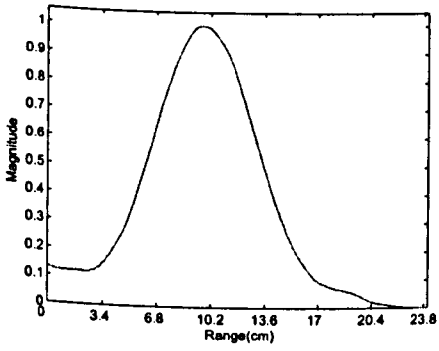

(e) *Temporal block* output at 10 cm

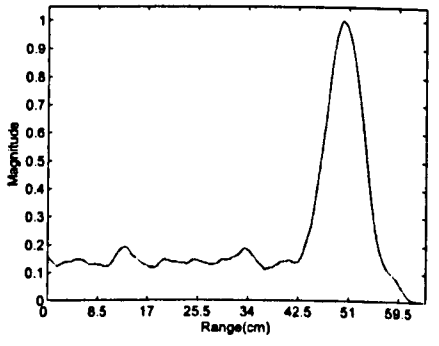

(f) *Temporal block* output at 50 cm

Figure 5.14: Signals for a SNR level of 0 dB.

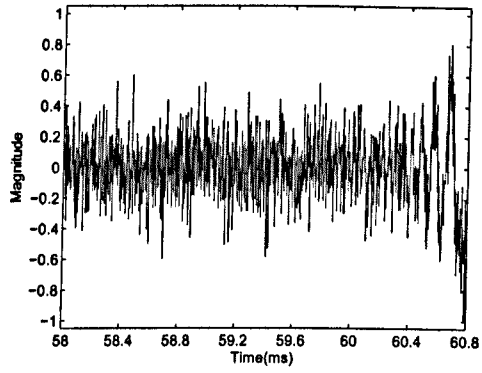

(a) Chirp signal at 10 m

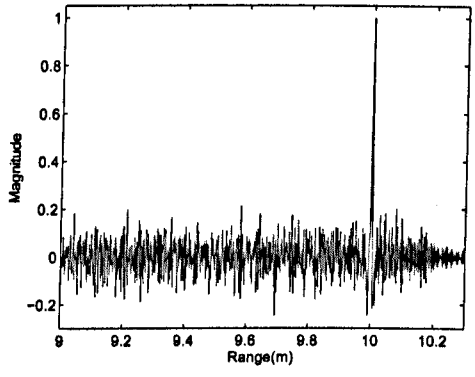

(b) Cross-correlation output at 10 m

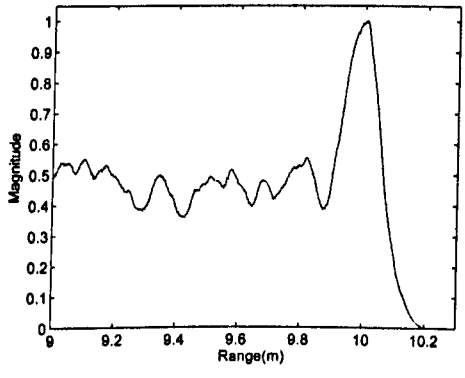

(c) *Temporal block* output at 10 m

Figure 5.15: Signals for a SNR level of 0 dB for a range of 10 meters.

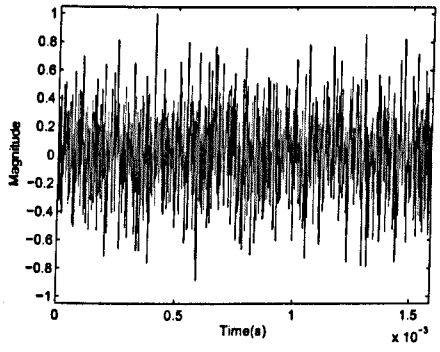

(a) Chirp signal at 10 cm

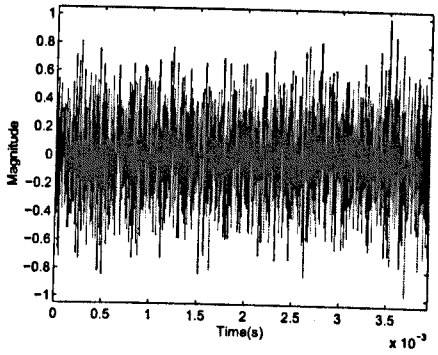

(b) Chirp signal at 50 cm

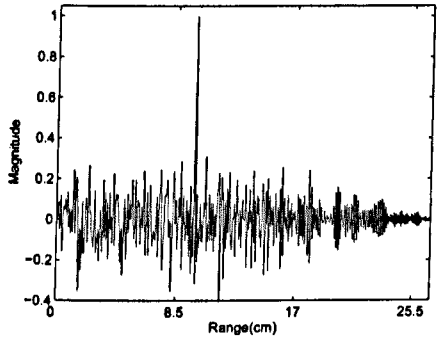

(c) Cross-correlation output at 10 cm

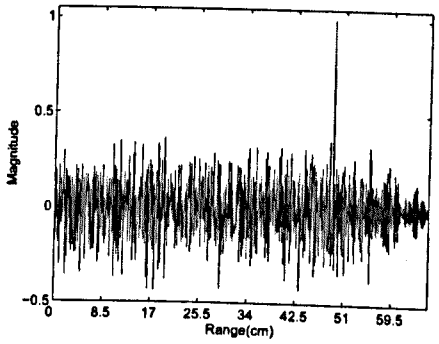

(d) Cross-correlation output at 50 cm

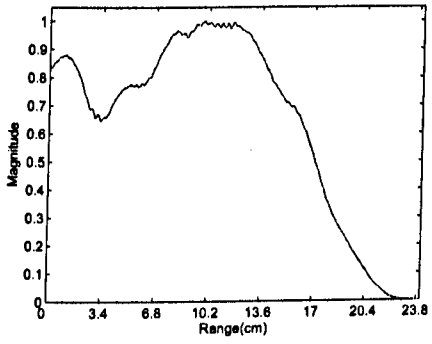

(e) *Temporal block* output at 10 cm

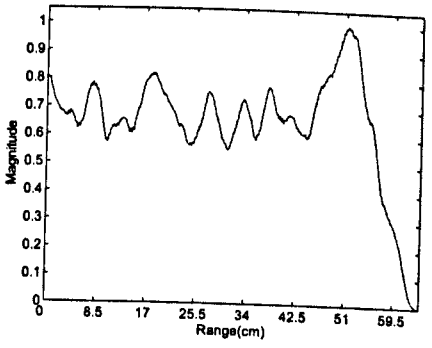

(f) *Temporal block* output at 50 cm

Figure 5.16: Signals for a SNR level of -20 dB.

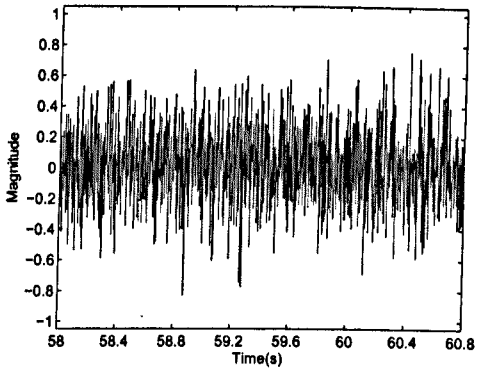

(a) Chirp signal at 10 m

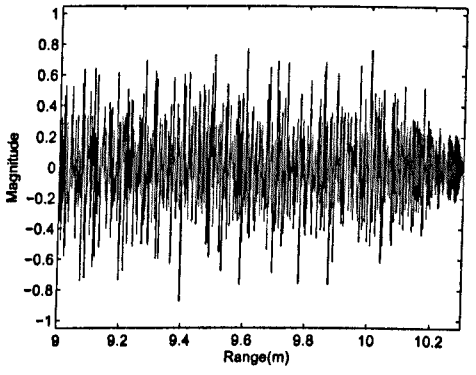

(b) Cross-correlation output at 10 m

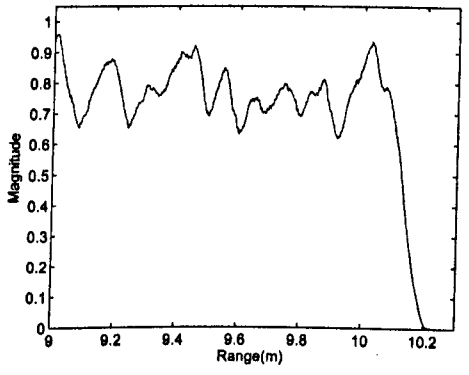

(c) *Temporal block* output at 10 m

Figure 5.17: Signals for a SNR level of -20 dB for a range of 10 meters.

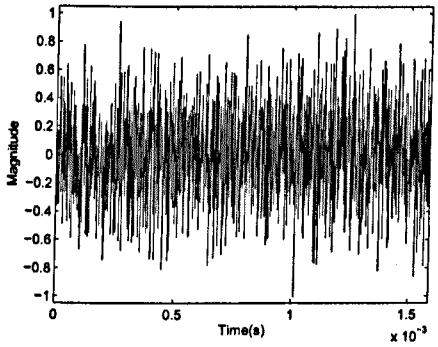

(a) Chirp signal at 10 cm

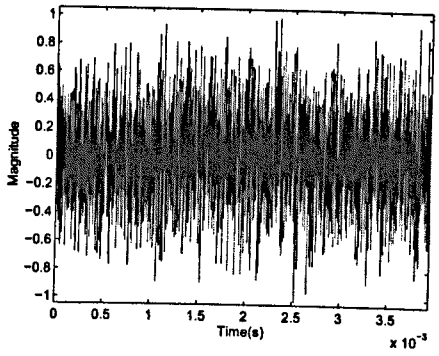

(b) Chirp signal at 50 cm

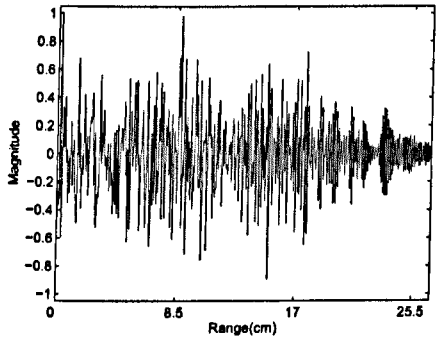

(c) Cross-correlation output at 10 cm

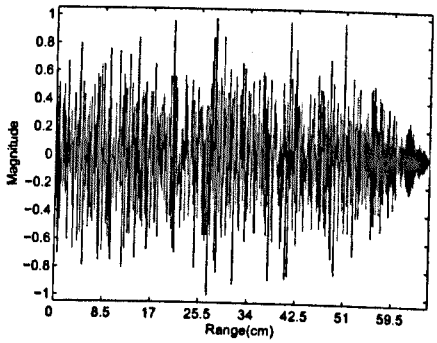

(d) Cross-correlation output at 50 cm

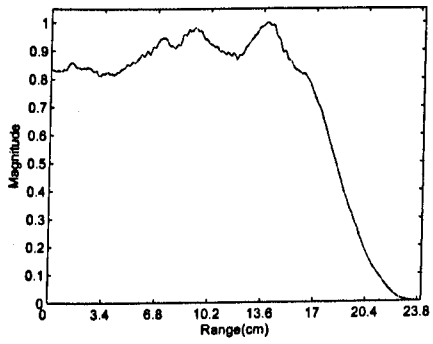

(e) *Temporal block* output at 10 cm

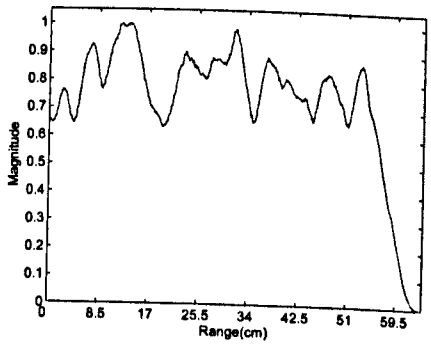

(f) *Temporal block* output at 50 cm

Figure 5.18: Signals for a SNR level of -30 dB.

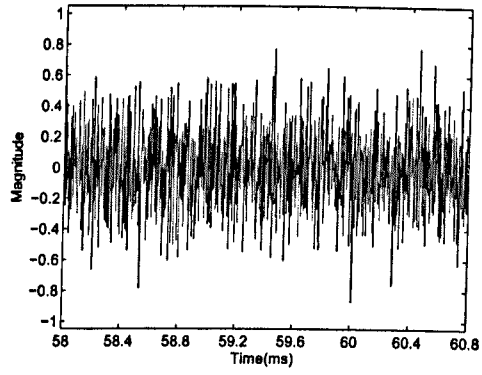

(a) Chirp signal at 10 m

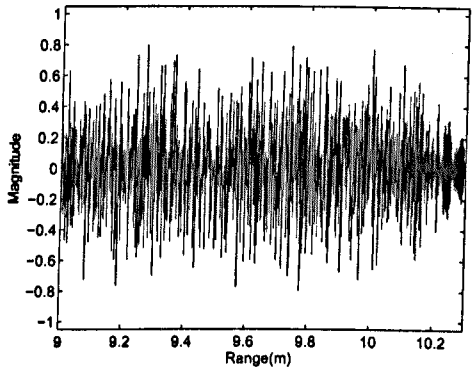

(b) Cross-correlation output at 10 m

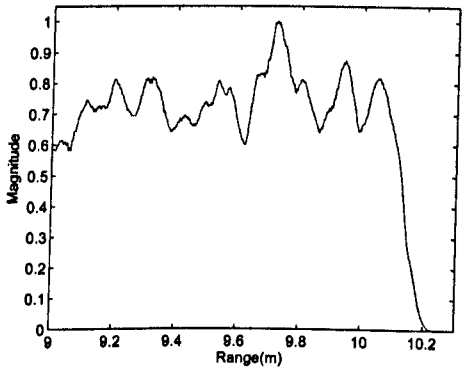

(c) *Temporal block* output at 10 m

Figure 5.19: Signals for a SNR level of -30 dB for a range of 10 meters.

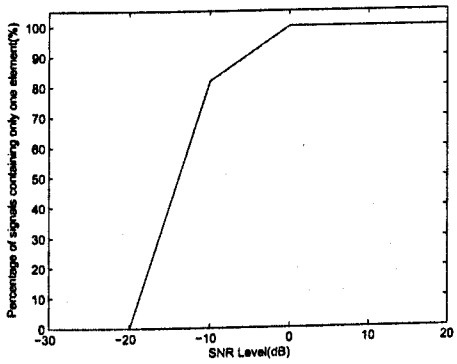

(a) *Temporal block* for a range of 10 cm

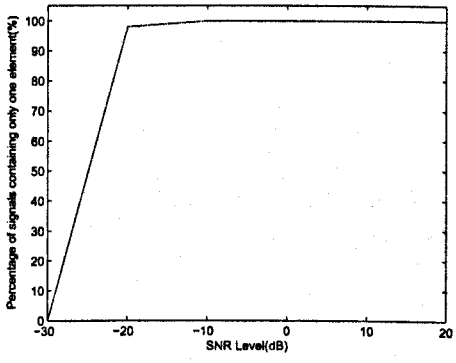

(b) Cross-correlation for a range of 10 cm

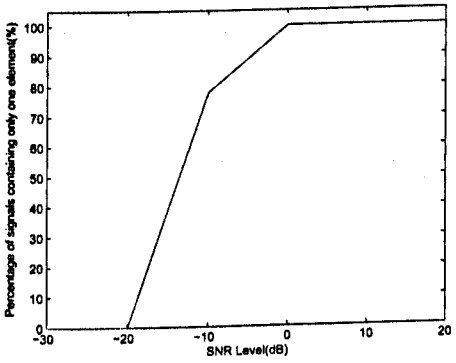

(c) *Temporal block* for a range of 50 cm

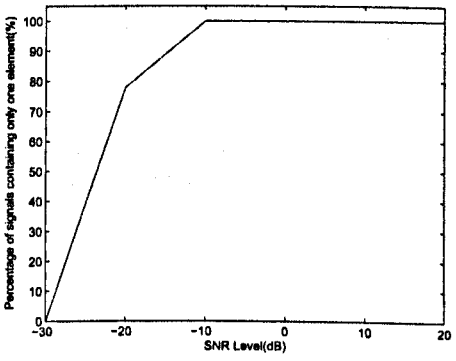

(d) Cross-correlation for a range of 50 cm

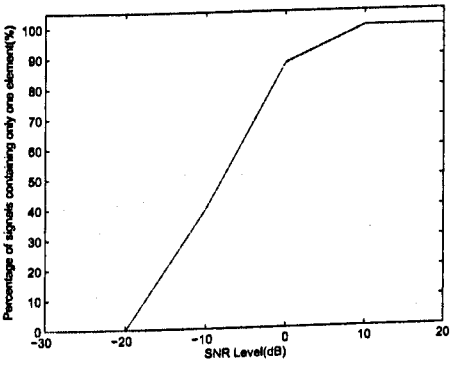

(e) *Temporal block* for a range of 10 m

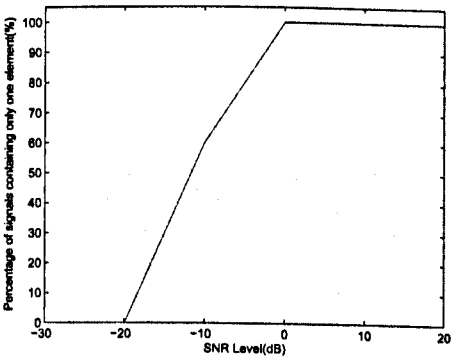

(f) Cross-correlation for a range of 10 m

Figure 5.20: Percentage of signal considered with only one element in relation to the level of SNR.

correlation method but still adequate for most practical conditions of SNR.

5.5.1.2 Relative error of the range measurement

After recording the percentage of single echo detections in the set of simulations, it was also of interest to show the distribution of the range determined by the two techniques to compare the performance. It shows how accurately the range is determined. For this purpose, the ranges for the two techniques were recorded over the five hundred simulations. In order to quantify how the two methods perform, the relative error of the range was calculated, hence providing measure of the dispersion of the values around the expected value. For each of the range measurements, the expected range value was known. Therefore for each of the five hundred simulations, the difference between the measured value and the expected value was recorded. These differences show how accurately, the techniques determine the range of an object.

In practical engineering systems, an accepted variation in resolution is commonly set at a wavelength, meaning that any object should be determined with a resolution of a wavelength. The wavelength is calculated at the centre frequency of the signal, corresponding in this case to a wavelength of $\lambda_{reso} = \frac{c}{f_c} = \frac{340}{70*10^3} \approx 4.9$ mm where f_c is the centre frequency of the chirp, i.e. 70 kHz and c is the velocity in air, i.e. 340 m/s.

Starting with a level of SNR of 10 dB, as shown on Figure 5.21, the relative error of the cross-correlation is zero for the three distances (Figure 5.21(b)(d)(f)). The relative error with the *Temporal block* varies at the extreme values from -1.36 mm to 1.7 mm with most of the values centred at zero. It shows that over the five hundred simulations, the *Temporal block* returns an accurate estimate of the three ranges, as the relative error is smaller than the wavelength resolution of $\lambda_{reso} = 4.9$ mm.

When the level of SNR decreases to 0 dB, the cross-correlation method de-

termines perfectly the range of the three chirp signals as illustrated on Figure 5.22(b)(d)(f). The relative error with the *Temporal block* is centred on a value of around 5.6 mm for the three ranges. The majority of the five hundred simulations for the three ranges have a relatie error ranging between 5 mm and 6 mm. When compared to the tolerance in resolution measurement, i.e. $\lambda_{reso} = 4.9\ mm$, it is in a close range. It demonstrates that for such a level of SNR, the *Temporal block* still determines the range of the three objects with an accuracy suitable for practical ultrasonic systems.

For a level of SNR of -20 dB, the cross-correlation determines accurately the range of the chirp signal located for the two cases of 10 cm and 50 cm as the relative error is close to zero, as shown on Figure 5.23(b)(d). However the cross-correlation fails at a range of 10 m, as shown on Figure 5.23(f), where the relative error is distributed on a large scale from 0 to 10.7 meters. The *Temporal block* for the three ranges has a large relative error. For the case of the ranges of 10 cm and 50 cm, values of the relative error are concentrated around respectively 10-15 cm and 4-7 cm on Figure 5.23(a)(c). These values are much higher than the centre wavelength of the chirp signal, i.e. $\lambda_{reso} = 4.9\ mm$, indicating that the *Temporal block* is unable to determine the range with such a level of SNR. This is confirmed by the results obtained for the range of 10 meters, where the relative error is distributed on a scale between -10.8 to 0 meters, as shown on Figure 5.23(e). With such a level of SNR, both of the techniques perform poorly. Finally for a level of SNR of -30 dB, the cross-correlation at a range of 10 cm performs accurately as the relative error is centred around zero, as illustrated on Figure 5.24(b). The variation for the *Temporal block* at a range of 10 cm shows a main peak value, as shown on Figure 5.24(a). For any other cases, Figure 5.24(c)(d)(e)(f), the distribution of the relative error is large, indicating that none of the techniques can determine the range of the chirp signals.

The evaluation of the performance is accomplished by evaluating the Range

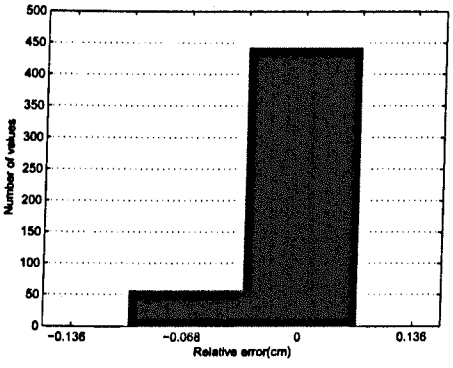

(a) *Temporal block* for a range of 10 cm

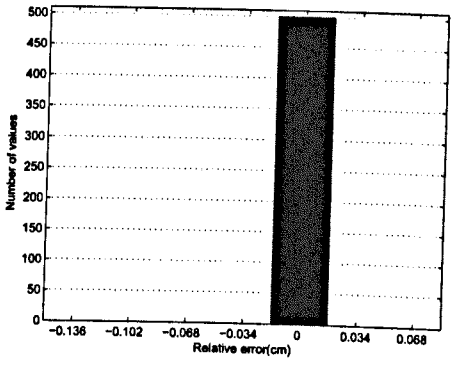

(b) Cross-correlation for a range of 10 cm

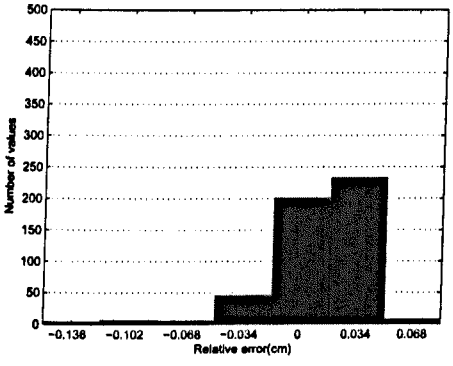

(c) *Temporal block* for a range of 50 cm

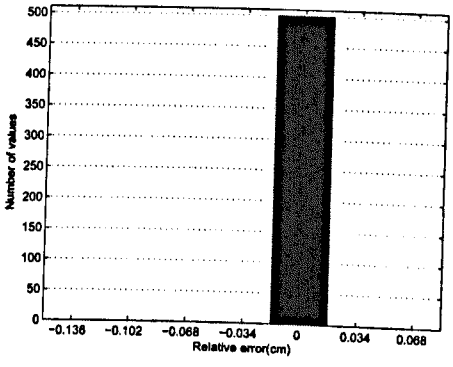

(d) Cross-correlation for a range of 50 cm

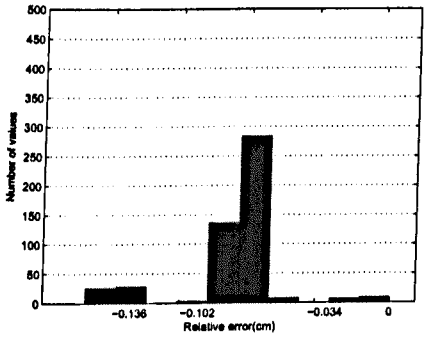

(e) *Temporal block* for a range of 10 m

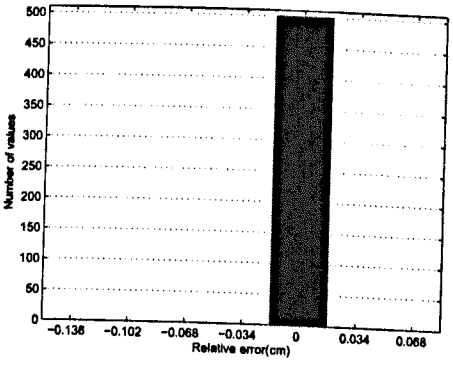

(f) Cross-correlation for a range of 10 m

Figure 5.21: Results from the *Temporal block* and cross-correlation for a SNR level of 10 dB.

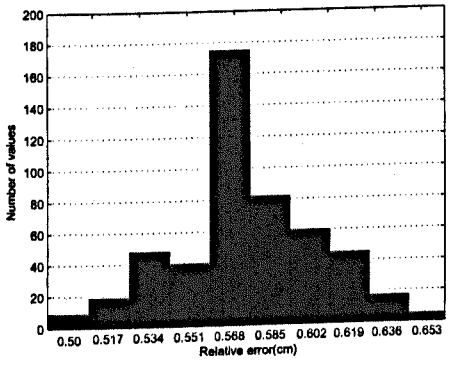

(a) *Temporal block* for a range of 10 cm

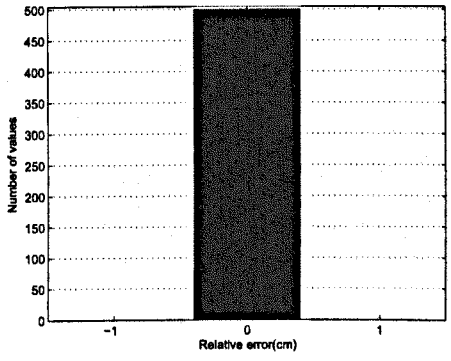

(b) Cross-correlation for a range of 10 cm

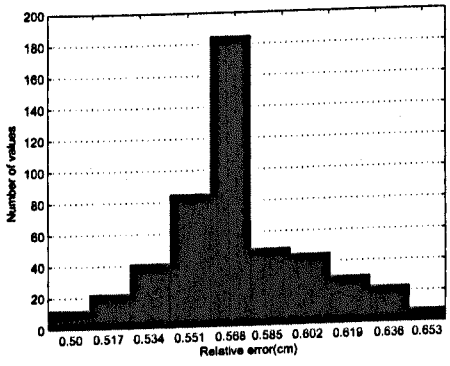

(c) *Temporal block* for a range of 50 cm

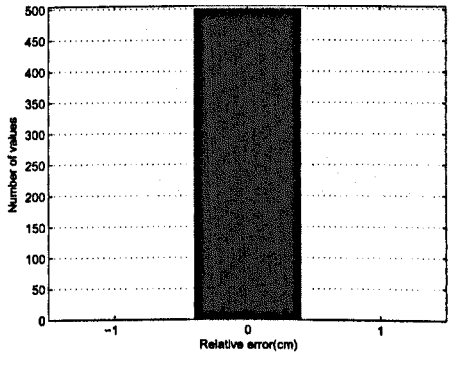

(d) Cross-correlation for a range of 50 cm

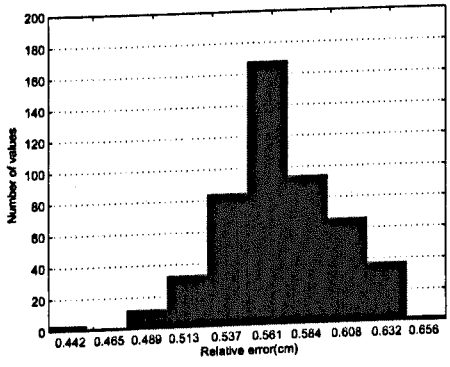

(e) *Temporal block* for a range of 10 m

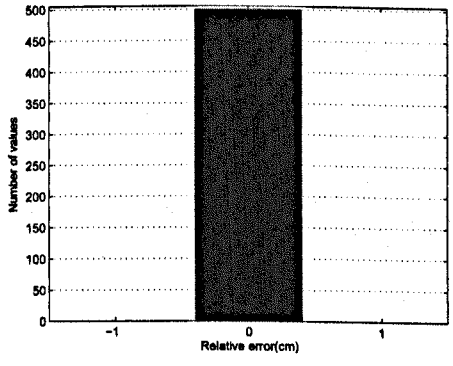

(f) Cross-correlation for a range of 10 m

Figure 5.22: Results from the *Temporal block* and cross-correlation for a SNR level of 0 dB.

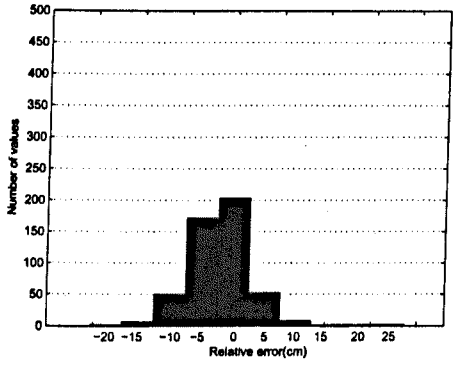

(a) *Temporal block* for a range of 10 cm

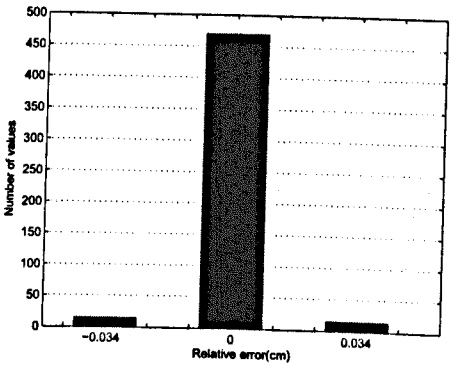

(b) Cross-correlation for a range of 10 cm

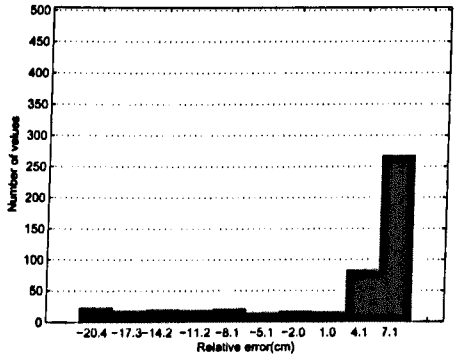

(c) *Temporal block* for a range of 50 cm

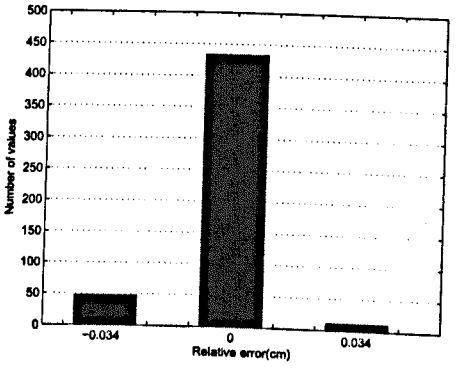

(d) Cross-correlation for a range of 50 cm

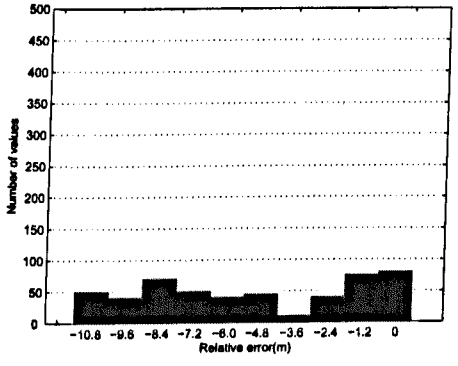

(e) *Temporal block* for a range of 10 m

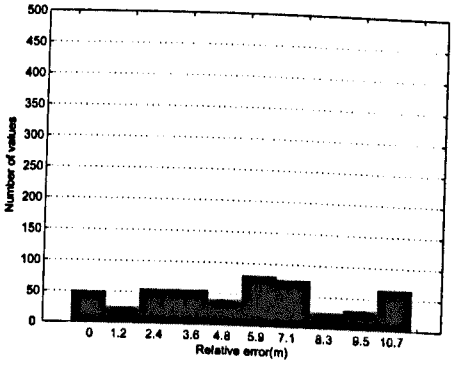

(f) Cross-correlation for a range of 10 m

Figure 5.23: Results from the *Temporal block* and cross-correlation for a SNR level of -20 dB.

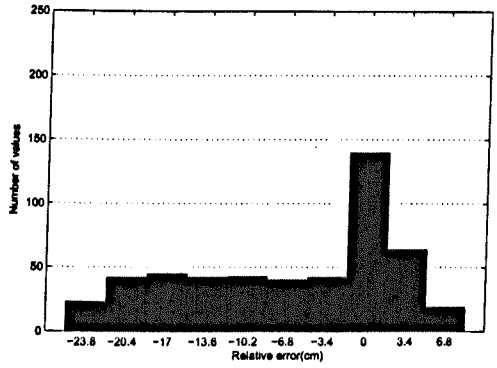

(a) *Temporal block* for a range of 10 cm

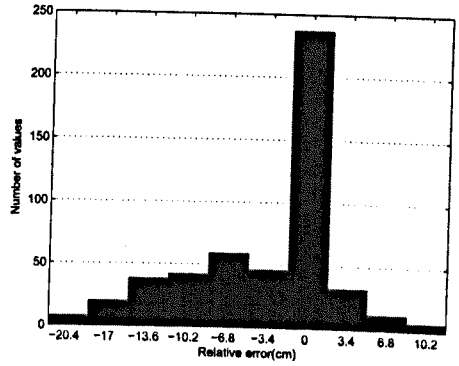

(b) Cross-correlation for a range of 10 cm

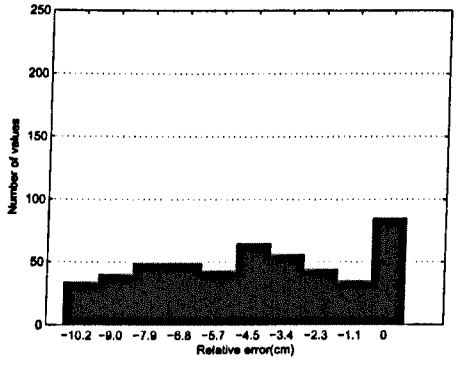

(c) *Temporal block* for a range of 50 cm

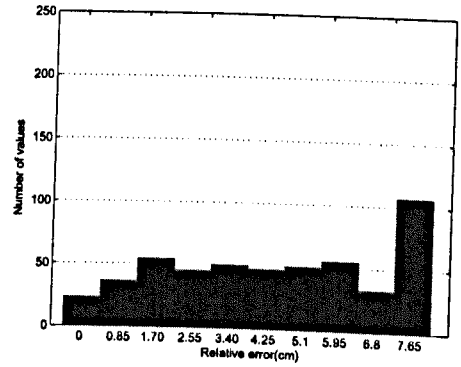

(d) Cross-correlation for a range of 50 cm

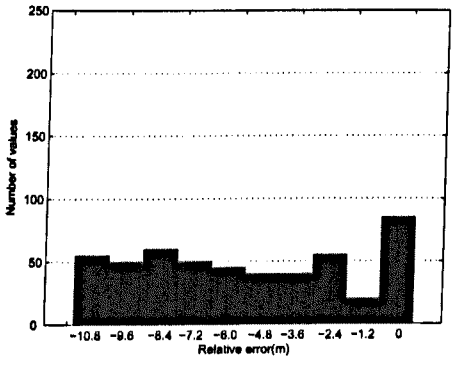

(e) *Temporal block* for a range of 10 m

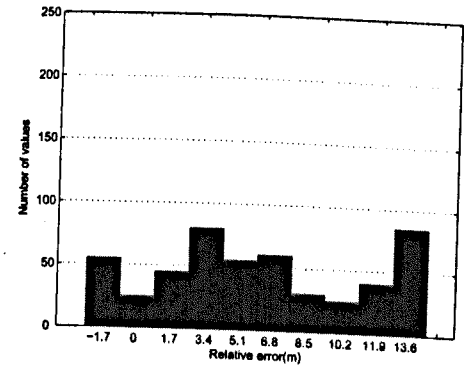

(f) Cross-correlation for a range of 10 m

Figure 5.24: Results from the *Temporal block* and cross-correlation for a SNR level of -30 dB.

Method	Range	RA (%)	WA (%)
BIRA	10 cm	100	100
	50 cm	99.9	93.1
	10 m	99.9	93.1
Cross-Correlation	10 cm	100	100
	50 cm	100	100
	10 m	100	100

Table 5.2: Range accuracy and Wavelength Accuracy evaluation for a level of SNR of 10 dB

Accuracy (RA) of the cross-correlation and the BIRA by the use of the Equation 5.4.

$$RA = \frac{MeanActualRange - RealRange}{RealRange} * 100 \tag{5.4}$$

The RA is relevant to evaluate the range accuracy of the BIRA and the cross-correlation.

The Wavelength Accuracy (WA) is also evaluated to quantify the accuracy in comparison to the average wavelength of the chirp (λ_{reso}). The definition of the WA is as defined in Equation 5.5.

$$WA = \frac{Mean\ Relative\ Error - \lambda_{reso}}{\lambda_{reso}} * 100 \quad for \quad -\frac{\lambda_{reso}}{2} \leq MeanRelativeError \leq \frac{\lambda_{reso}}{2}$$
$$WA = 0 \quad for \quad for \quad -\frac{\lambda_{reso}}{2} \geq MeanRelativeError \geq \frac{\lambda_{reso}}{2} \tag{5.5}$$

The results for the four levels of SNR are presented in Table 5.2 to Table 5.5. It summarises the accuracy of the two methods.

For this set of simulations, the performance of the *Temporal block* does not match the one of the cross-correlation. However for reasonable level of SNR, 10 dB and 0 dB, the *Temporal block* indicates ranges with an accuracy acceptable for ultrasonic systems. For the lower levels of SNR, -20 dB and -30 dB, the *Temporal block* is limited for practical applications.

Method	Range	RA (%)	WA (%)
BIRA	10 cm	94	0
	50 cm	98	0
	10 m	99.9	0
Cross-Correlation	10 cm	100	100
	50 cm	100	100
	10 m	100	100

Table 5.3: Range accuracy and Wavelength Accuracy evaluation for a level of SNR of 0 dB

Method	Range	RA (%)	WA (%)
BIRA	10 cm	100	100
	50 cm	N/A	N/A
	10 m	N/A	N/A
Cross-Correlation	10 cm	100	100
	50 cm	100	100
	10 m	N/A	N/A

Table 5.4: Range accuracy and Wavelength Accuracy evaluation for a level of SNR of -20 dB

Method	Range	RA (%)	WA (%)
BIRA	10 cm	100	100
	50 cm	N/A	N/A
	10 m	N/A	N/A
Cross-Correlation	10 cm	100	100
	50 cm	N/A	N/A
	10 m	N/A	N/A

Table 5.5: Range accuracy and Wavelength Accuracy evaluation for a level of SNR of -30 dB

By analysing the set of simulations, the two methods can be used to evaluate the presence of an echo buried in noise. Even at a level of SNR equal to -30 dB, Figure 5.24, the relative error of the *Temporal block* still contains a distinctive peak value, at a relative error of zero, of almost twice the value of other peaks (Figure 5.24(a)(c)(e)). Therefore, it may be sufficient for a bat to have a frequency representation of the noisy echo and the existence of an echo is determined simply by the level of energy combined with the time of occurrences. The precise range may not be required but rather the overall energy corresponding to the echo of an insect. This is what is done by the *Temporal block* by combining the frequency channels to determine the range.

5.6 Conclusion

This Chapter has presented the performance of the BIRA when applied to a more realistic environment. The performance has been quantified when air attenuation is introduced in the algorithm and has shown the sidelobes added to the output signal of the *Spectral block*. The *Temporal block* has been demonstrated to be robust with respect to the attenuation in air, to determine the range of a single echo.

The requirement for frequency bandwidth has been quantified. Independently, this evaluation showed that a FBW of at least 160 % is required to avoid the introduction of any significant spurious sidelobes. This information provides valuable information for the design of any ultrasonic transducer. It also indicates the frequency bandwidth requirement to broadcast bat like chirp signal.

The results of this investigation are extremely interesting. Under noise free conditions and assuming that the transducer system can generate and detect over the chirp bandwidth, the accuracy of the *Temporal block* is preserved. In other words, it is likely that the bat does possess high quality range finding ability in

the air environment and that this could be of potential use in other ultrasonic applications. However, the fact that the *Spectral block* is degraded significantly by frequency constraints imposed by absorption in the propagation channel and transducer limitations, poses some serious but interesting questions.

Firstly, unless the bat can compensate for attenuation in air, it is unlikely that the creature can resolve closely spaced targets. This is discussed in greater detail in Chapter 7. The applicability of the BIRA to practical ultrasonic systems is also open to question, especially as the algorithm is limited to only two successive reflections. This is discussed in more detail in Chapter 6, where a simplified, but realistic ultrasonic imaging system is considered in more detail.

Analysis of the BIRA as a range finding algorithm is also interesting. Provided that the chirp frequency data is preserved, the algorithm performs quite well in most practical noise environments-although is does not match the performance of classical cross-correlation methods at higher levels of noise. However, it is probably sufficient for the bat to determine target location. This is discussed further in Chapter 7.

Chapter 6

Evaluation of the BIRA on a simulated ultrasonic ranging system

6.1 Introduction

An analysis of the bat auditory system has led to the development of the BIRA. To examine whether the BIRA can be used for practical engineering applications, a further evaluation of the algorithm in an environment that includes realistic system behaviour is now performed.

This Chapter presents a software model that is representative of a situation occurring in ultrasonic engineering applications. This model is used to simulate the interaction between the transducer, the medium of propagation and the object under examination. It is used to compare the BIRA with the deconvolution processes, presented in Chapter 4, for improving the axial resolution.

Firstly, a description of the ultrasonic ranging system is provided. Then, the first set of simulations evaluates the algorithm performance for determining the time of arrival of a first echo. It is followed by a second set of simulations, used to quantify the resolution capability on multiple overlapping echoes. Finally, discussions on the results with conclusions are presented.

6.2 Ultrasonic ranging system

The ultrasonic ranging system was designed to create overlapping echoes from target structures that allow comparison between the deconvolution techniques and the BIRA. The ranging system simulated a piezo-electric transducer, the propagation medium and a straightforward planar target structure. The aim of this model was to create representative data of the reflection sequence in a standard imaging application.

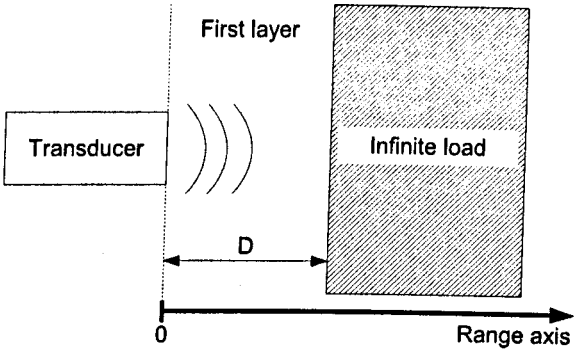

Figure 6.1: Ultrasonic ranging system.

6.2.1 Outline of the system

The ultrasonic ranging system was designed using PiezoCAD©, a commercial code capable of simulating accurately the response of an ultrasonic system. Although restricted to 1D plane wave propagation, the code is versatile, easy to use and presents an ideal basis for comparison of the different techniques on realistic ultrasonic data. It is intended primarily for the design of transducers and the measurement of performance in various propagation media. In this Section, it was used with the purpose of generating overlapping echoes for a set of representative transducers. The overall ultrasonic ranging system is illustrated on Figure 6.1.

The transducer generates acoustic waves that propagate along the range axis. When the wave reaches the boundary between two media such as air (First layer) and water (Infinite load), part of the wave is reflected back and another part is propagated into the medium. This phenomenon is repeated when the wave reaches the transducer front face. The acoustic waves bounce back and forward in the first layer creating successive echoes along the range axis. The resulting data corresponds to a succession of echoes located at the delay time proportional to the thickness of the layer, as illustrated on Figure 6.2.

In the software model, the type of material used in the first layer, the infinite load and the transducer characteristics, can be defined by the user. This

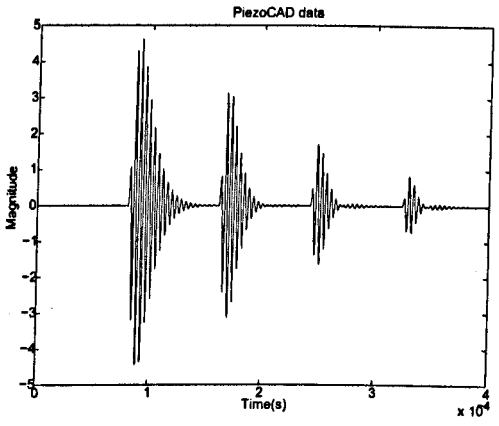

Figure 6.2: Example of data generated with PiezoCAD©.

rudimentary approach was sufficient to create the constraints introduced by the transducer and the effects of the medium. The parameters of the transducer were varied to cover a set of devices representative of real engineering applications.

6.2.2 Transducer Design

The design of the transducer was adjusted to cover a set of representative characteristics employed in the ultrasonic domain. A generic set of two transducer responses was created, corresponding to narrowband and wideband behaviour. These two types of transducers are commonly aimed for different type of applications. The narrowband transducer is generally used to generate a high energy output, for applications such as SONAR or occasionally structural testing. The wideband transducer is used where short pulse durations are required, such as in high-resolution biomedical systems. The characteristics of each of the transducers used for the simulations are illustrated in Figure 6.3. It shows the time and frequency responses of the narrowband and wideband devices.

The conditions for narrowband and wideband behaviour were generated by changing the design characteristics. The most straightforward method for bandwidth adjustment is to use a backing block, attached to the rear face of the transducer. This reduces internal reverberation within the device and is normally

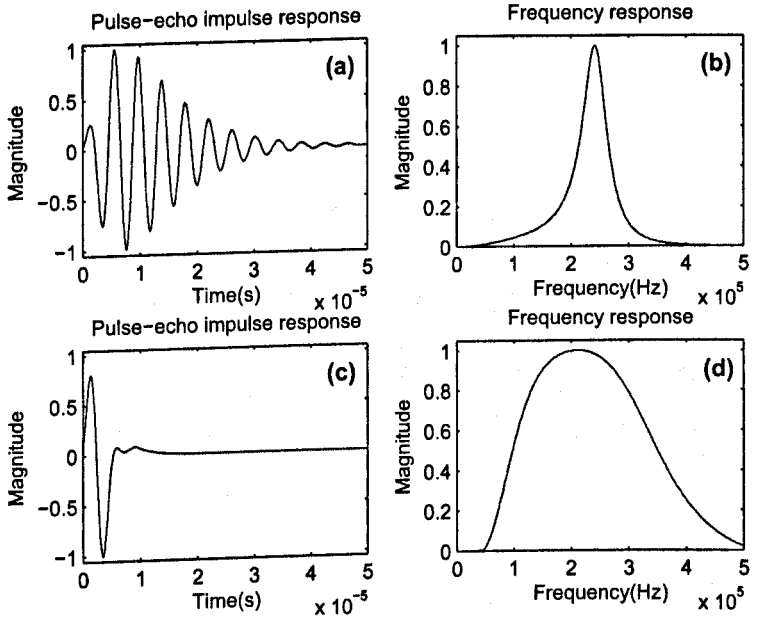

Figure 6.3: (a): Narrowband transducer pulse-echo impulse response. (b) Narrowband transducer frequency response. (c): Wideband transducer pulse-echo impulse response. (d) Wideband transducer frequency response.

very lossy, ensuring no mechanical energy is reflected back into the transducer. Although more sophisticated techniques are available, such as multiple matching layers at the front face, the use of a simple backing block allows sufficient bandwidth for the present purpose. Therefore, in order to generate narrowband and wideband transducer response profiles, the acoustic impedance of the backing material was changed. For the narrowband transducer, the acoustic impedance of the backing material was set to 0 $MRayl$ whereas the backing material for the wideband transducer was set to 25 $MRayl$. For both of the transducers, the centre frequency was set at $f_c = 250$ kHz as it is reasonably close to the bat spectrum. The detailed characteristic of the set of transducers is given in Table 6.1 that includes the type of material, the size of the elements and the associated acoustic properties.

For the purpose of comparison, it was required to introduce a way of quantifying the bandwidth of each transducer. The measurement of bandwidth is defined

Parameter	Value
Design center frequency F_d	250 kHz
Element size	100 mm disk
Thickness	8.8 mm
Material	EC-98
Longitudinal impedance	34.496 MRayls
Longitudinal velocity	4400.0 $m.sec^{-1}$
Acoustic faceplates	No faceplates/No backplates
Acoustic Load Impedance	Rear = 0 or 25 MRayl

Table 6.1: Characteristics of the transducer

by the FBW similar to Chapter 5 in Equation 5.3. It is a value of the relative bandwidth of a transducer in relation to the centre frequency. The FBW was measured for the narrowband and wideband devices of 21 % and 111 % respectively.

6.3 Simulations

The simulations presented in this Section compare the performance of the deconvolution techniques and the BIRA. The ultrasonic ranging system described previously was used to generate the ultrasonic data when it was driven by the narrowband or the wideband transducer.

Firstly, the simulations were done to determine the performance with regard to measure the time of arrival of the first echo in different materials. Secondly, a set of simulations evaluated the algorithm to separate multiple overlapping echoes. Finally, the noise robustness was examined. The software simulations have been implemented in Matlab©.

6.3.1 Resolution performance

The ultrasonic ranging system illustrated on Figure 6.1 was used to generate multiple overlapping echoes. To evaluate the BIRA in a range of representative ultrasonic signals, the structure of the layered system was altered by changing the

type of materials. Two structures were simulated, the first one was composed of a first layer of aluminium and an infinite load of water and the second structure was composed of a first layer of ice with an infinite load of water. With these two structures, the created echoes have significant different characteristics because of the changes in the acoutic impedance of the materials. For the structure of aluminium and water, the respective acoustic impedance is of $Z_{Aluminium} = 17$ $MRayl$ and $Z_{Water} = 1.5$ $MRayl$. As the difference in acoustic impedance is large, the returned echo to the transducer is strong. For the structure of ice and water, the acoustic impedance of the ice is of $Z_{Ice} = 2.95$ $MRayl$. Therefore, the returned echo is smaller as the difference in acoustic impedance is reduced.

For all the simulations, the transducer was driven by a Gaussian windowed LFM signal. The chirp signal was set to cover the spectrum of the transducer by starting at a frequency $f_{start} = 100$ kHz and ending at a frequency $f_{end} = 400$ kHz with a period of $T = 20$ μs. An illustration of the chirp excitation is shown on Figure 6.4. The Gaussian window applied on the chirp was used to reduce the Fresnel oscillations. To generate realistic data, the simulations were performed with a relatively low noise level, with a SNR = 100 dB, as any ultrasonic system must perform in the presence of some noise.

The BIRA computed the *Spectral block* in a range of frequency from 100 kHz to 400 kHz with the number of base vectors set to 101, by experiment. The *Temporal block* covered a frequency range from 100 kHz to 400 kHz with 51 chirplet filters.

As the aim of these simulations was to evaluate the resolution performance of the BIRA, the thickness of the first layer of the ultrasonic ranging system was set adequately. By definition, the theoretical axial resolution, i.e. the smallest time separation that any ultrasonic imaging system can resolve, is commonly set by the wavelength at the centre frequency of the transducer. Two sets of simulations were conducted with the thickness of the first layer respectively set to values of

λ and 2λ, where the wavelength λ was calculated at the centre frequency of the transducer, i.e. $f_d = 250\ kHz$. The value of λ is dependent on the medium of propagation, therefore the thickness of the first layer was changed with the material. For the structure of Aluminium-Water, the velocity in aluminium is of $c_{Aluminium} = 6320\ m/s$. Starting with the equation $\lambda = \frac{c}{f_d}$ where c is the velocity of the medium and f_d the centre frequency of the transducer, the wavelength in aluminium was calculated of 26 mm. Therefore, the thickness of the aluminium was set to either $\lambda = 26$ mm or $2\lambda = 52$ mm. The same calculation was done for the set of Ice-Water where the velocity in ice is of $c_{Ice} = 3980$ m/s. Therefore the thickness of the ice was set to $\lambda = 16$ mm and $2\lambda = 32$ mm.

With such a ranging system, the acoustic wave propagated in the first layer and bounced back and forward. This generated multiples echoes located at multiple of the time of travel of the acoustic signal in the first layer. The expected time of arrival of each echo is related to the thickness D of the first layer as shown on Figure 6.1. It is calculated from Equation 6.1.

$$t_{expected} = \frac{2D}{c} \tag{6.1}$$

where D is the thickness of the layer and c the velocity of sound in the material.

The expected time of travel of an acoustic wave for a thickness of 52 mm of aluminium with a velocity of $c_{Aluminium} = 6320\ m/s$ is, as the wave has to travel forward and back, of 16.46 μs. Therefore, it was expected to obtain an echo every 16.46 μs when the acoustic wave traveled in the first layer. The same method was applied for the thickness of $\lambda = 26\ mm$ of aluminium. The time separation between each echo was expected to be 8.23 μs, half the time of travel of a thickness of $2\lambda = 52\ mm$.

Similarly with the structure of Ice-Water, the expected time of arrival was determined by the velocity in ice of $c_{Ice} = 3980\ m/s$. For a thickness of 32 mm, it

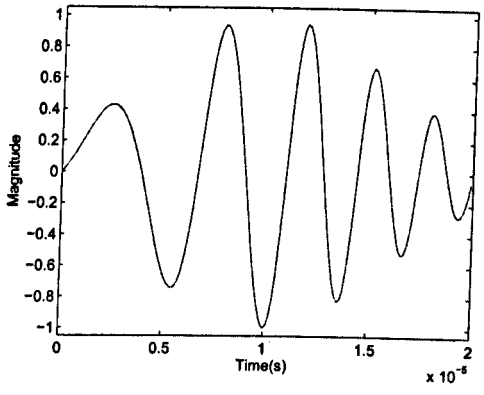

Figure 6.4: Chirp signal used to drive the transducer.

was expected to obtained an echo every 16.08 μs when the acoustic wave traveled in the first layer. For the thickness of 16 mm of ice, the expected time separation between each echo was of 8.04 μs.

With such an ultrasonic ranging system, it was proposed to firstly evaluate the performance of the BIRA to determine the time of arrival of the first echo and secondly to quantify the axial resolution, i.e. the smallest time separation that the BIRA can identify.

6.3.1.1 Performance to determine the time of arrival of the first echo

This set of simulations were performed to quantify the accuracy and robustness of the BIRA to determine the time of arrival of the first echo in a sum of overlapping echoes. For comparative assessment, the cross-correlation technique was employed. This method is standard for the determination of the time of arrival of a known reference signal in the presence of noise. It is the optimal method for a given level of SNR. The cross-correlation $g(k)$ of two signals $x(t)$ and $y(t)$ is as defined in Equation 6.2.

$$g(k) = \int x^*(t)y(k+t)dt \tag{6.2}$$

where $x(t)^*$ denotes the conjugate of $x(t)$.

The cross-correlation consists of an identification process of a reference signal, $y(t)$, contained in a measured signal, $x(t)$. The reference signal is shifted along the measured signal to determine the best match. The higher the similarities between the signals, the higher is the response from the cross-correlation. The best match is indicated in the cross-correlation output by the maximum peak value. In the purpose of these simulations, it corresponds to the time of arrival of the first echo.

The simulations comprised one of the two transducer models described previously, i.e. narrowband or wideband case with one of the two structures of Aluminium-Water or Ice-Water. The transducer was driven by the chirp excitation shown on Figure 6.4. The aim was to process the output signal of the ultrasonic ranging system with the cross-correlation and the BIRA when considering the two structures of Aluminium-Water and Ice-Water. Firstly, the simulations were performed on the Aluminium-Water structure for the narrowband and wideband case. Secondly, the same simulations were performed with the Ice-Water structure.

6.3.1.1.1 Structure of Aluminium-Water .

This first structure consisted of the first layer composed of aluminium and an infinite load of water. The thickness of the layer of aluminium was set to 52 mm, as stated before, it corresponds to a time of arrival of the first echo of a value of 16.46 μs.

For the case of the narrowband transducer, the results are shown on Figure 6.5. The output of the ultrasonic ranging system, as illustrated on Figure 6.5(a), shows the overlapping echoes generated by the layered structure. With such a signal, it is not straightforward to identify the time of arrival of the first echo. The same issue exits when the full wave rectified is considered, as shown on Figure 6.5(b). When the envelope of the cross-correlation function is considered, as shown on Figure 6.5(c), it clearly indicates the time of arrival of each echo with a significant peak

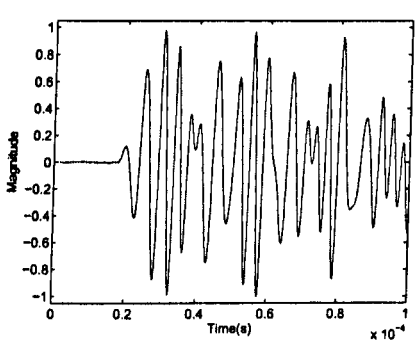

(a) Time response of the ultrasonic ranging system

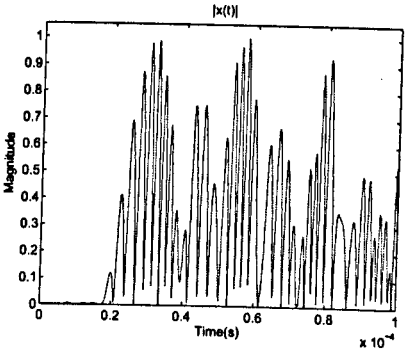

(b) Full wave rectified of the time response of the ultrasonic ranging system

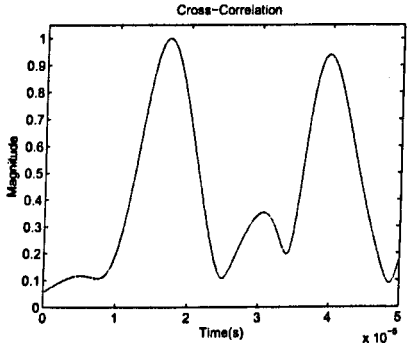

(c) Envelope of the cross-correlation response

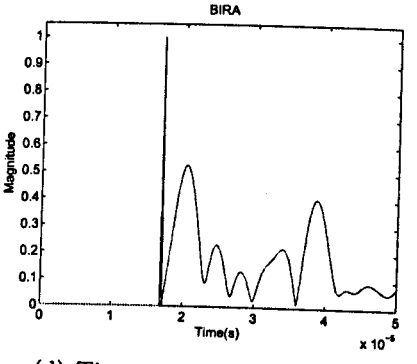

(d) Time response of the BIRA

Figure 6.5: Time responses to measure time of arrival of first echo with the narrowband transducer and the structure of Aluminium-Water.

value at a time of 17.08 μs. This value was measured on an accurate scale. The following peak values can be ignored at the moment as the purpose is to analyse the time of arrival of the first echo. It will be the purpose of a detailed analysis in the following Section. Then, the signal formed by the BIRA is shown on Figure 6.5(d), with the time of arrival of the first echo indicated by the short-pulse at a time of 17.10 μs.

The same structure of Aluminium-Water was then simulated with the case of the wideband transducer, as shown on Figure 6.6. With the increase in the bandwidth, it can be noticed that the pulse time durations have decreased, as illustrated on Figure 6.6(a)(b). However, as shown on Figure 6.6(a) and Figure 6.6(b), it is still not straithforward to identify the time of arrival of the first echo

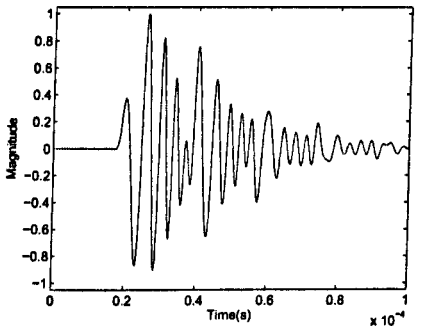

(a) Time response of the ultrasonic ranging system

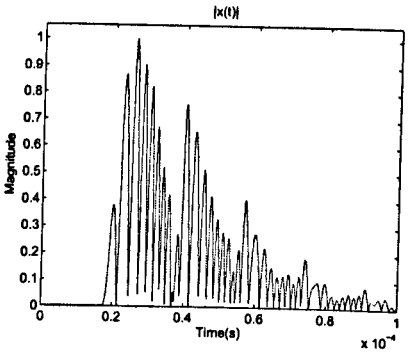

(b) Full wave rectified of the time response of the ultrasonic ranging system

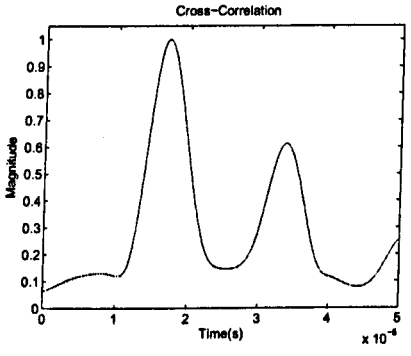

(c) Envelope of the cross-correlation response

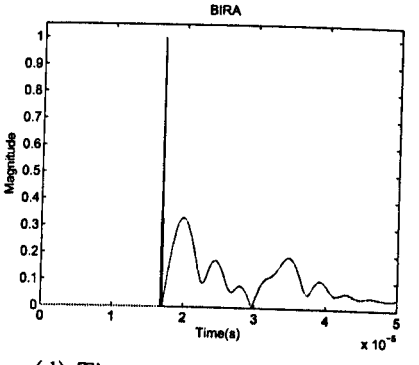

(d) Time response of the BIRA

Figure 6.6: Time responses to measure time of arrival of first echo with the wideband transducer and the structure of Aluminium-Water.

whereas with the envelope of the cross-correlation the time of arrival of the first echo is indicated by the first peak value at 16.98 μs, as shown on Figure 6.6(c). With the increase in the bandwidth, the determination of the time of arrival is improved due to the sharper response profiles. Finally, the output of the BIRA is shown on Figure 6.6(d) with the time of arrival of the first echo indicated by the short-pulse at a time of 16.90 μs. It can also be noticed that the level of sidelobes on the right hand side of the short-pulse has decreased when compared to the output of the BIRA on Figure 6.5(d), indicating an improved response of the *Spectral block*.

6.3.1.1.2 Struture of Ice-Water .

This second structure consisted of the first layer composed of ice and an infinite

load of water. The thickness of the layer of ice was set to 32 mm, as stated before, it corresponds to a time of arrival of the first echo of a value of 16.08 μs. The approach was similar to the structure of the Aluminium-Water with the two cases of a narrowband transducer and a wideband transducer.

The case of the narrowband transducer, is shown on Figure 6.7. The time response of the ultrasonic ranging system, illustrated on Figure 6.7(a), contains multiple overlapping echoes. The full wave rectified version is shown on Figure 6.7(b). For this case of the narrowband transducer, the time of arrival of the first echo is indicated by the first main peak value in the envelope of the cross-correlation as shown on Figure 6.7(c). The time of arrival of the first echo with the cross-correlation technique was measured on an accurate scale at 15.99 μs. The signal formed by the BIRA is shown on Figure 6.7(d) with the short-pulse located at a time of 15.98 μs, corresponding to the time of arrival of the first echo. The signal formed by the BIRA contains again spurious sidelobes on the right hand sidelobes of the short-pulse, revealing significant malfunction of the *Spectral block.*

The case of the wideband transducer for the structure of Ice-Water is shown on Figure 6.8 where the increase in the bandwidth has sharpened the time reponses. As illustrated on Figure 6.8(c), the increase in bandwidth, as narrowed down the signal of the cross-correlation technique as it clearly indicates the time of arrival of the first echo with the first main peak value at a time of 16.10 μs. The output from the BIRA, Figure 6.8(d), also shows the time of arrival of the first echo at a time of 16.10 μs with again the existence of sidelobes but with a lower level than the narrowband case.

6.3.1.1.3 Conclusion on the determination of the time of arrival of the first echo .

When considering the cross-correlation as an accurate assessor of the measure-

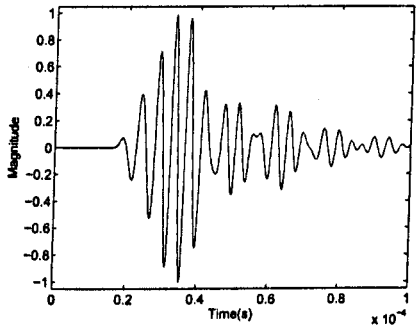

(a) Time response of the ultrasonic ranging system

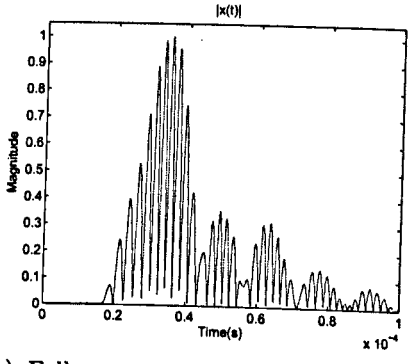

(b) Full wave rectified of the time response of the ultrasonic ranging system

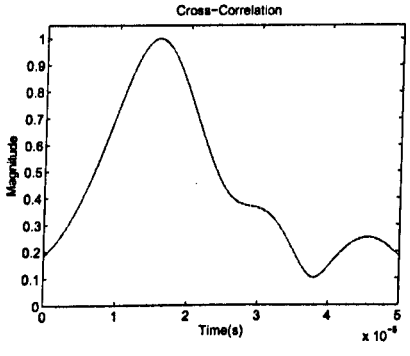

(c) Envelope of the cross-correlation response

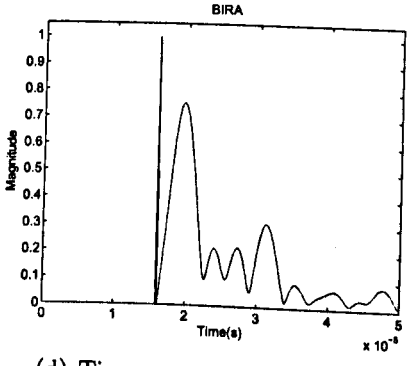

(d) Time response of the BIRA

Figure 6.7: Time responses to measure time of arrival of first echo with the narrowband transducer and the structure of Ice-Water.

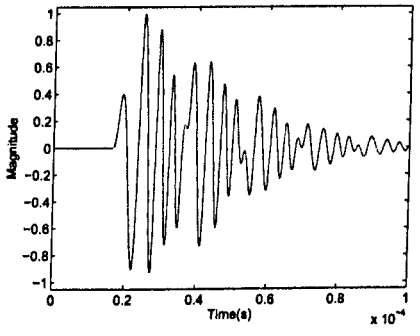

(a) Time response of the ultrasonic ranging system

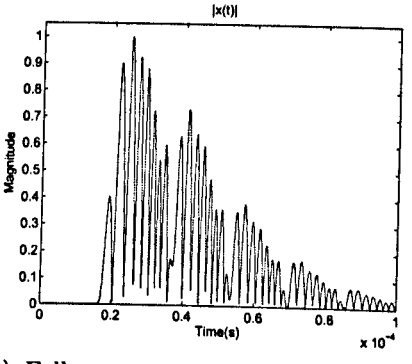

(b) Full wave rectified of the time response of the ultrasonic ranging system

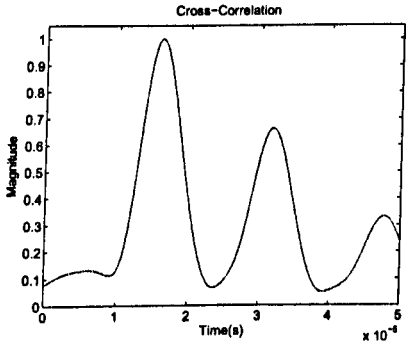

(c) Envelope of the cross-correlation response

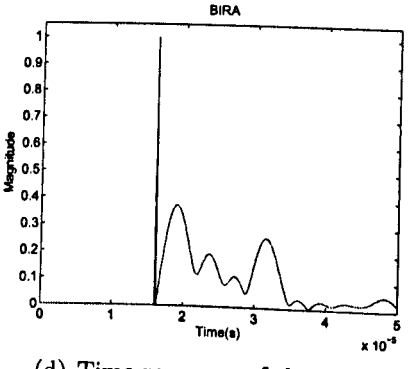

(d) Time response of the BIRA

Figure 6.8: Time responses to measure time of arrival of first echo with the wide-band transducer and the structure of Ice-Water.

Method	Transducer type	Measured time of arrival (μs) $t_{expected} = 16.46\ \mu s$	Relative Error (%)
BIRA	Narrowband	17.10	3.9
	Wideband	16.96	3
Cross-Correlation	Narrowband	17.08	3.8
	Wideband	16.96	3

Table 6.2: Results for the measurement of the time of arrival of the first echo with a structure of Aluminium-Water

Method	Transducer type	Measured time of arrival (μs) $t_{expected} = 16.08\ \mu s$	Relative Error (%)
BIRA	Narrowband	15.98	0.6
	Wideband	16.10	0.1
Cross-Correlation	Narrowband	15.98	0.6
	Wideband	16.10	0.1

Table 6.3: Results for the measurement of the time of arrival of the first echo with a structure of Ice-Water

ment of the time of arrival of the first echo, the relative error on the measured time of arrival was quantified for the two structures of Aluminium-Water and Ice-Water. The measurements of the time of arrival for the structure of Aluminium-Water is presented on Table 6.2. The relative error on the measurement of the time of arrival is also shown when considering the expected time of arrival to be of 16.46 μs. For the case of the narrowband transducer, the cross-correlation estimated the time of arrival of the first echo with a relative error of 3.8 %. BIRA dertermined the time of arrival of the first echo with a relative error of 3.9 %. For the case of the wideband transducer, the cross-correlation and the BIRA estimated the time of arrival with a relative error of 3 %.

The same calculations were done with the structure of Ice-Water as shown in Table 6.3. With such a structure, the relative error for the cross-correlation and the BIRA when considering the narrowband transducer was of 0.6 %. For the wideband transducer, the relative error decreased to a value of 0.1 %.

The results presented in this Section illustrated the accuracy of the BIRA

to determine the time of arrival of the first echo in comparison with the cross-correlation technique. The structures used in these simulations were representative of ultrasonic systems. The relative error to determine the time of arrival of the first echo for the BIRA and the cross-correlation were in the same order, validating the accuracy of the BIRA to determine the time of arrival of the first echo. When driven by a narrowband or wideband transducer, creating a significant change in bandwidth and signal characteristics, BIRA determined the expected time of arrival of the first echo as accurately as the cross-correlation. Furthermore, when the bandwidth was increased, it was shown that the level of the spurious lobe, in the signal formed by the BIRA, was decreased, as expected from the analysis in Chapter 5.

The other important result concerns the robustness of BIRA with changes in the acoustic properties of the medium. For the two structures of Aluminium-Water and Ice-Water with different acoustic properties that are met in practical applications, BIRA stayed as robust as the cross-correlation to determine the time of arrival of the first echo. The performance of the BIRA was comparable to the one obtained with the cross-correlation technique, which is known as the optimal receiver for a given level of SNR. These results support the adequacy of the BIRA to determine the time of arrival of the first echo in conditions similar to practical engineering applications.

6.3.1.2 Performance with multiple echoes

The next set of the simulations consisted of evaluating the discrimination capability of the BIRA in comparison to some established deconvolution algorithms. Two techniques, named as Spectral Division and Oldenburg, have been described in Chapter 4 and were implemented in that Section. Again, the ultrasonic ranging system illustrated on Figure 6.1 was used to generate multiple overlapping echoes in the same conditions as the previous simulations.

The aim of the simulations was to evaluate the discrimination performance. Therefore, the thickness of the first layer was set to a value of 2λ for a first set a simulations and then to a value of λ. Those two thicknesses were adequate to evaluate the discrimination performance as they correspond to the theoretical axial resolution. The two structures of Aluminium-Water and Ice-Water were used for the simulations and they were driven either by the narrowband transducer or the wideband transducer.

The techniques of Spectral Division and Oldenburg were applied to deconvolve both the response from the transducer and the chirp excitation driving the transducer. A model of the ultrasonic ranging system driven by a chirp signal can be represented by Equation 6.3 as below:

$$x(t) = w(t) * c(t) * u(t) * h(t) \tag{6.3}$$

where $x(t)$ is the measured signal, $w(t)$ is the transmitted impulse response of the transducer, $c(t)$ the chirp signal, $u(t)$ the system response and $h(t)$ the received impulse response of the transducer. The deconvolution techniques were used to calculate an inverse solution of the quantity $w(t)*c(t)*h(t)$ to extract the response of the system $u(t)$. For this purpose, the response of the ultrasonic ranging system with no layer was measured corresponding to the quantity of $m(t) = w(t) * c(t) * h(t)$. This response, $m(t)$, was used for the implementation of the deconvolution techniques in the calculation of the inverse solution as detailed in Chapter 4.

6.3.1.2.1 Structure of Aluminium-Water

The first case concerned the narrowband transducer with the structure of Aluminium-Water where the thickness of the aluminium was set firstly to $2\lambda = 52$ mm and secondly to $\lambda = 26$ mm.

For the thickness of aluminium of $\lambda = 52$ mm, it was expected to observe an echo every 16.46 μs as demonstrated previously. The time response obtained

from the ultrasonic ranging system is as illustrated on Figure 6.9(a) with the full wave rectified signal shown on Figure 6.9(b). On both of these plots, it is not straightforward to identify the time of arrival of each echo. However the envelope of the cross-correlation function indicates the time of arrival of each by a maximum value, as shown on Figure 6.9(c). The strongest peak values are numbered and represent the time of arrival of each echo. The corresponding values for each numbered echo are summarised in Table 6.4 and were measured on a accurate scale. Peak values are indicated by the cross-correlation as individual echoes, but clearly some are erroneous as, it was expected to obtain a peak value every 16.46 μs. The shape of the signals generated by the deconvolution techniques contain more accurate structural information but some are also erroneous, as illustrated in Figure 6.9(d)(e). They demonstrate shorter pulses that are also characteristic of deconvolution methods. When compared to the cross-correlation, the time of arrival of each echo is in the same order, as summarised in Table 6.4. The use of deconvolution should help improve discrimination capability. For the case of the Oldenburg technique, it can be observed that the peak value number 2 is at a time of 37.99 μs, which is close to the theoretical time value of 32.92 μs (Any peak value that is not a time multiple of 16.46 μs, is considered as a spurious peak). Although the Oldenburg algorithm is extracting features of the structure as accurately as cross-correlation does, the system response and the insufficient transducer bandwidth created errors. Similar results are obtained with the Spectral Division technique, with the time of arrival of each echo is as illustrated on Figure 6.9(e) and summarised in Table 6.4. The output generated by the BIRA is shown on Figure 6.9(f) where the time of arrival for the first echo is indicated at a time of 16.46 μs as shown on Table 6.4. The characteristic of the BIRA signal is different from the deconvolution techniques as the feature of the signal of the BIRA is composed of two main peak values at 16.96 μs and 38.55 μs. The peak value, arising between the echo number 1 and the echo number 2, is a

Method	1^{st} echo (1) (μs) $t_{expected}$ = 16.46 μs	2^{nd} echo (2) (μs) $t_{expected}$ = 32.92 μs	3^{rd} echo (3) (μs) $t_{expected}$ = 49.38 μs	4^{th} echo (4) (μs) $t_{expected}$ = 65.84 μs
Cross-correlation	16.96	39.65	62.34	76.25
Oldenburg	17.01	37.99	55.19	76.30
Spectral Division	16.96	38.31	55.27	76.37
BIRA	16.96	38.55	55.02	N/A

Table 6.4: Times of arrival of the echoes for a structure of Aluminium-Water with a narrowband transducer and a thickness of aluminium of 52 mm

spurious lobe created by the underlying processes in the BIRA. However, BIRA still indicates the following echo at an approximate time of 55.02 μs - a similar error as the other methods.

To further evaluate the performance of the BIRA in term of axial resolution, the thickness of the aluminium was decreased to a value of $\lambda = 26\ mm$. For that case, it was expected to observe an echo every 8.23 μs as demonstrated previously. The output signal from the ultrasonic ranging system is shown on Figure 6.10(a)(b). The response obtained from the cross-correlation contains a higher number of peak values where the first four peak values are numbered and presented in Table 6.5. It can be noticed that the peak values do not correspond to the theoretical times as it was expected to be at 8.23 μs, 16.46 μs, 24.69 μs and 32.92 μs. For the case of the Oldenburg technique, the signal contains more features, with the most significant peak values being numbered and presented in Table 6.5. Some of the peak values are inappropriate as they do not correspond to any expected time of arrival of an individual echo. For the case of the Spectral Division technique, the same errors occur, as shown from the values listed in Table 6.5. Finally, the BIRA estimates the time of arrival of the echoes as shown on Table 6.5. The spurious lobe between the echo number 1 and number 2 is still present.

From the two thickness of 2λ and λ, the case of the narrowband data was further evaluated by measuring the time separation between the first and second

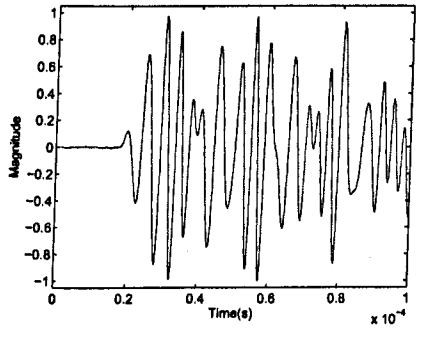

(a) Time response of the ultrasonic ranging system

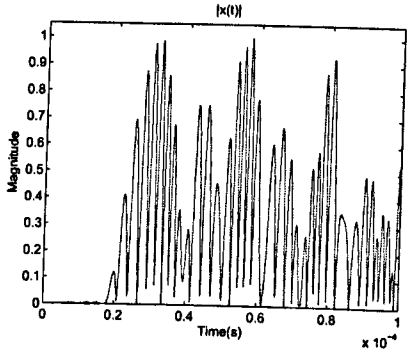

(b) Full wave rectified of the time response of the ultrasonic ranging system

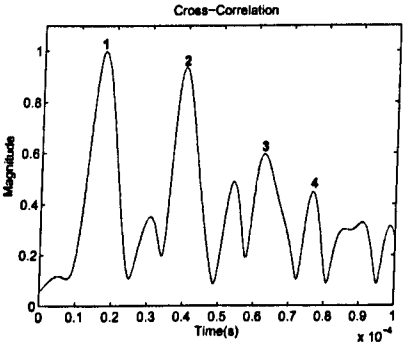

(c) Envelope of the cross-correlation response

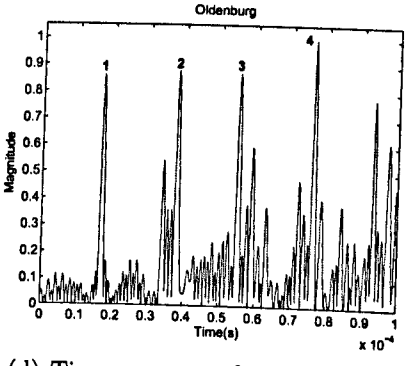

(d) Time response of the Oldenburg

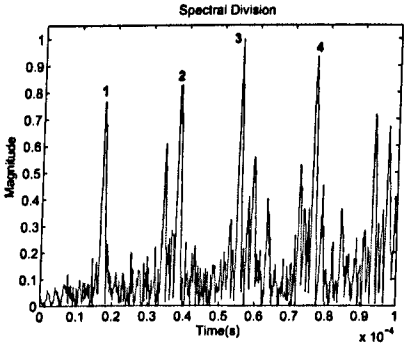

(e) Time response of the Spectral Division

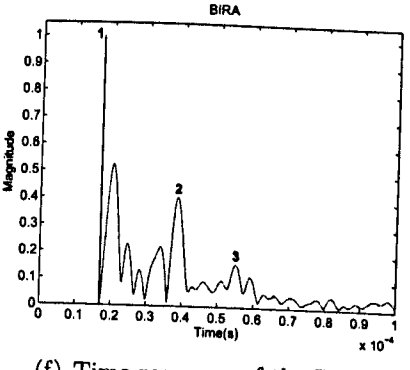

(f) Time response of the BIRA

Figure 6.9: Time responses with narrowband transducer with a structure of Aluminium-Water and a thickness of aluminium of 52 mm.

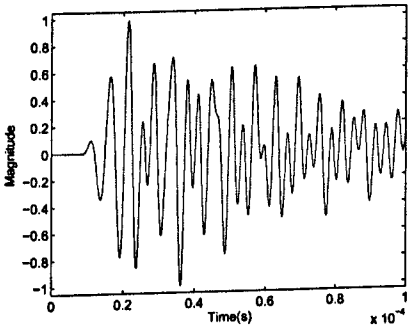

(a) Time response of the ultrasonic ranging system

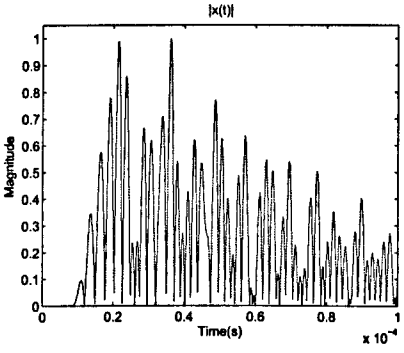

(b) Full wave rectified of the time response of the ultrasonic ranging system

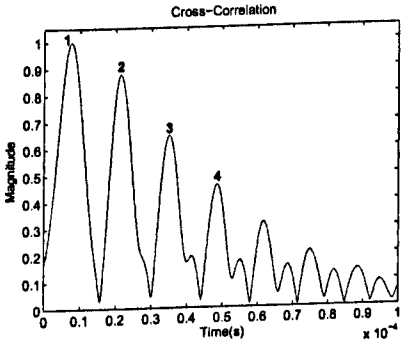

(c) Envelope of the cross-correlation response

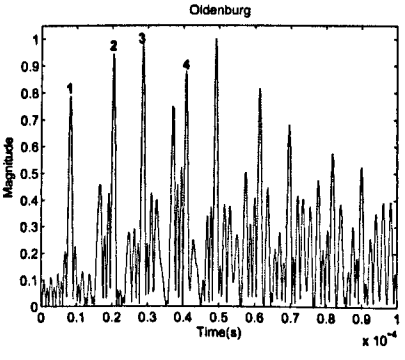

(d) Time response of the Oldenburg

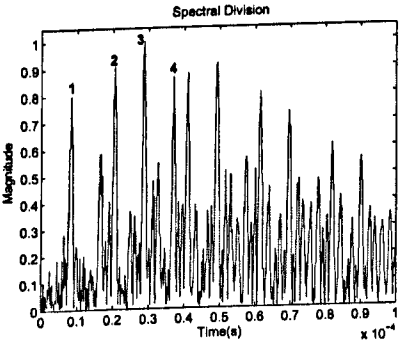

(e) Time response of the Spectral Division

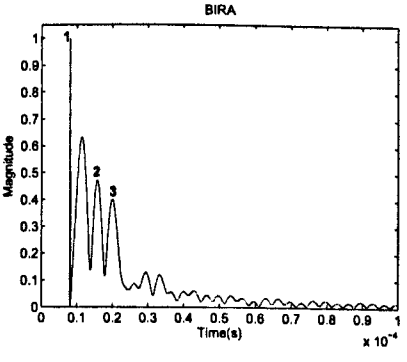

(f) Time response of the BIRA

Figure 6.10: Time responses with narrowband transducer with a structure of Aluminium-Water and a thickness of aluminium of 26 mm.

Method	1^{st} echo (1) (μs) $t_{expected}$ = 8.23 μs	2^{nd} echo (2) (μs) $t_{expected}$ = 16.46 μs	3^{rd} echo (3) (μs) $t_{expected}$ = 24.69 μs	4^{th} echo (4) (μs) $t_{expected}$ = 32.92 μs
Cross-correlation	7.56	21.35	35.01	48.43
Oldenburg	8.10	20.30	28.60	40.68
Spectral Division	8.30	20.50	28.80	36.97
BIRA	8.05	15.74	19.88	N/A

Table 6.5: Times of arrival of the echoes for a structure of Aluminium-Water with a narrowband transducer and a thickness of aluminium of 26 mm

Method	Measured time separation between 1^{st} echo and 2^{nd} echo $t_{expected}$ = 16.46 μs	Relative error (%)
Cross-correlation	22.69	37.85
Oldenburg	20.98	27.46
Spectral Division	21.35	29.71
BIRA	21.59	31.17

Table 6.6: Time separations and relative errors between the first and second echo for a structure of Aluminium-Water with a narrowband transducer and a thickness of aluminium of 52 mm

echo. It is a valuable indicator of the performance of the algorithms. For a thickness of 52 *mm* of aluminium, it was expected to obtain a time separation of 16.46 μs whereas a thickness 26 *mm* corresponded to time separation of 8.23 μs. The relative error for each case was calculated as shown in Equation 6.4.

$$Relative\ error = \frac{|t_2 - t_1|}{t_{expected}} \times 100 \tag{6.4}$$

where t_2 is the time of arrival of the second echo, t_1 is the time of arrival of the first echo and $t_{expected}$ is the expected time separation between the two echoes.

For a thickness of 52 *mm* of aluminium, the results are shown on Table 6.6. The time separations were calculated from Table 6.4. It shows that the relative error is large for any algorithms. For such data, the algorithms performed poorly due to the limited transducer bandwith. BIRA performed as well as the other methods. For a thickness of 26 *mm* of aluminium, the relative error results are

Method	Measured time separation between 1^{st} echo and 2^{nd} echo $t_{expected} = 8.23\ \mu s$	Relative error (%)
Cross-correlation	13.79	67.56
Oldenburg	12.20	48.24
Spectral Division	12.20	48.24
BIRA	7.69	6.56

Table 6.7: Time separations and relative errors between the first and second echo for a structure of Aluminium-Water with a narrowband transducer and a thickness of aluminium of 26 mm

shown on Table 6.7. The time separations were calculated from Table 6.5. The error value is also significant for the three conventional techniques, which was also due to the restricted transducer bandwidth.

Overall, the performance of the techniques with the narrowband data was mostly restrained to the determination of the time of arrival of the first echo. Some of the following echoes were obtained but in most cases with an incorrect time. The main reason of the restricted performance was the limited bandwidth of the transducer and better performance were expected with the wideband transducer.

The following case concerns the use of the wideband transducer on the same structure of Aluminium-Water with the same thicknesses. Firstly, the thickness of the aluminium was set to $2\lambda = 52\ mm$. For such a thickness of aluminium, it was expected to obtain an echo every 16.46 μs, i.e. at the time sequence of 16.46 μs, 32.92 μs, 49.38 μs, etc... For the output of the cross-correlation, as shown on Figure 6.11(c), the method estimated the time of arrival of the first three echoes, with the corresponding time values listed in Table 6.8. These values were read on an accurate scale. The increase in the bandwidth reduced the presence of spurious peak values when compared to the narrowband case shown on Figure 6.9(c). The improvement in discrimination performance was also obtained for the case of the Oldenburg technique and the Spectral Division technique, as shown on Figure 6.11(d)(e) with the three distinctive peak values being numbered. The corresponding time values are shown in Table 6.8. For the case of the BIRA, the

Method	1^{st} echo (1) (μs) $t_{expected}$ = 16.46 μs	2^{nd} echo (2) (μs) $t_{expected}$ = 32.92 μs	3^{rd} echo (3) (μs) $t_{expected}$ = 49.38 μs
Cross-correlation	17.08	34.21	51.29
Oldenburg	17.60	34.21	51.24
Spectral Division	17.02	34.16	51.24
BIRA	16.96	34.65	N/A

Table 6.8: Times of arrival of the echo for a structure of Aluminium-Water with a wideband transducer and a thickness of aluminium of 52 mm

time of arrival of two echoes were estimated when the spurious lobe was ignored as indicated on Figure 6.11(f). Any other peak values, correspond to spurious or unwanted lobes. When compared to the narrowband case, the spurious lobe of BIRA has a lower amplitude.

The performance of the BIRA in term of axial resolution was further evaluated by reducing the thickness of the aluminium to a value of $\lambda = 26\ mm$. With such a thickness, it was expected to observe an echo sequence at time of 8.23 μs, 16.46μs, 24.69 μs, etc... The cross-correlation output estimated the time of arrival of the first echoes as indicated on Figure 6.12(c) with the corresponding time values listed in Table 6.9. For the Oldenburg technique and Spectral block technique, the respective time values are also presented in Table 6.9 in relation to Figure 6.12(d)(e). It shows that the three techniques perform better when there was an increase in the bandwidth as the spurious peak values had significantly reduced. For the case of the BIRA, the time estimates are shown on Figure 6.12(f) with the corresponding time values listed in Table 6.9. The spurious lobe still existed in the BIRA positioned between the two echoes.

In the same way as the narrowband data, the wideband data were used to calculate the time separation between the first and second echo. The relative error for each technique was also quantified. For a thickness of 52 mm, the results from the time separation and the relative error are shown in Table 6.10. These values were calculated from Table 6.8. The Oldenburg method appears to perform better

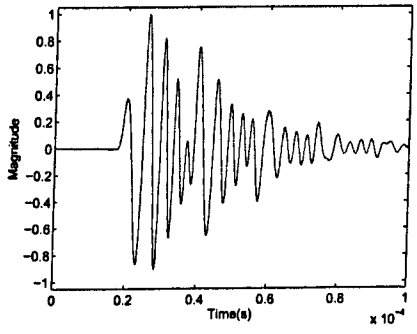

(a) Time response of the ultrasonic ranging system

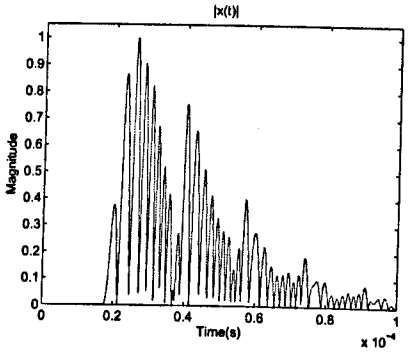

(b) Full wave rectified of the time response of the ultrasonic ranging system

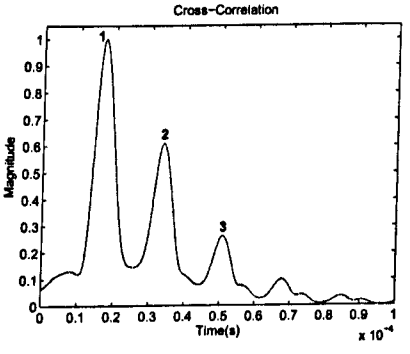

(c) Envelope of the cross-correlation response

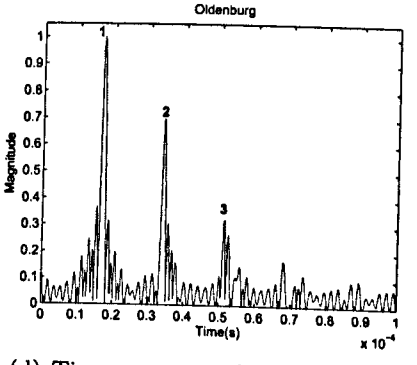

(d) Time response of the Oldenburg

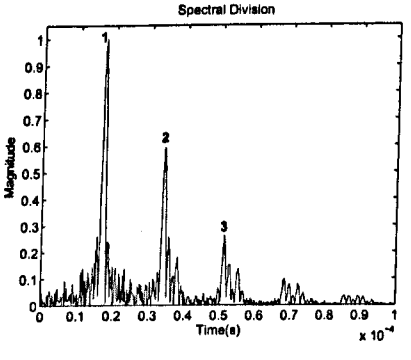

(e) Time response of the Spectral Division

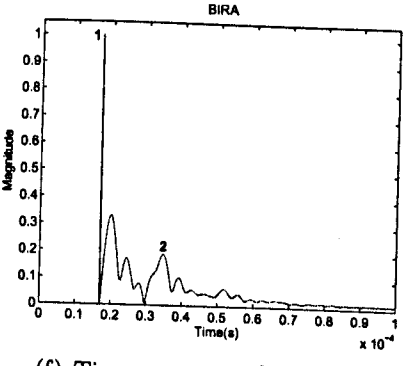

(f) Time response of the BIRA

Figure 6.11: Time responses with wideband transducer with a structure of Aluminium-Water and a thickness of aluminium of 52 mm.

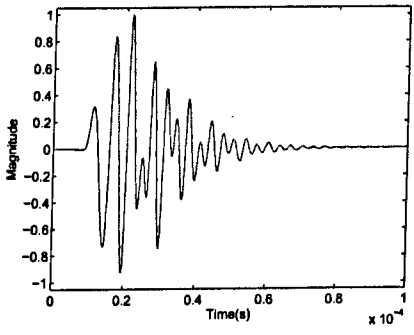

(a) Time response of the ultrasonic ranging system

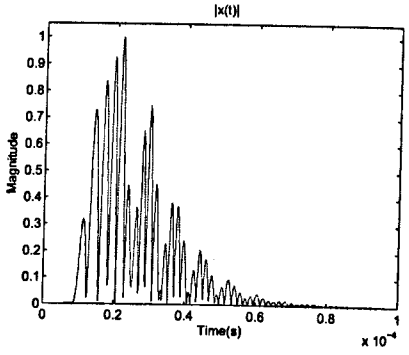

(b) Full wave rectified of the time response of the ultrasonic ranging system

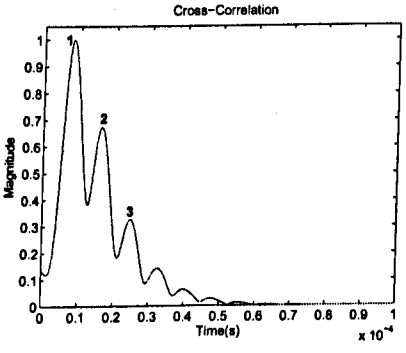

(c) Envelope of the cross-correlation response

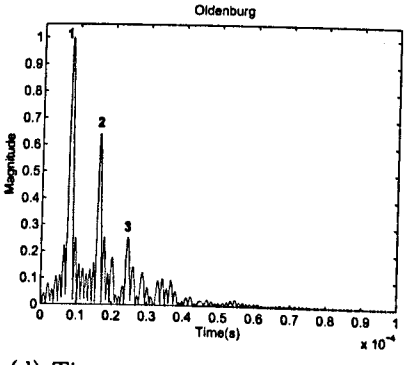

(d) Time response of the Oldenburg

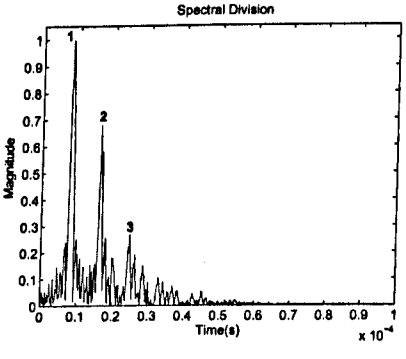

(e) Time response of the Spectral Division

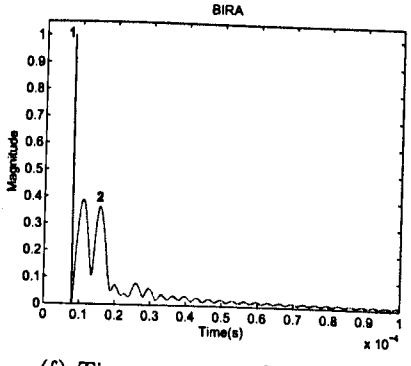

(f) Time response of the BIRA

Figure 6.12: Time responses with wideband transducer with a structure of Aluminium-Water and a thickness of aluminium of 26 mm.

Method	1^{st} echo (1) (μs) $t_{expected}$ = 8.23 μs	2^{nd} echo (2) (μs) $t_{expected}$ = 16.46 μs	3^{rd} echo (3) (μs) $t_{expected}$ = 24.69 μs
Cross-correlation	8.05	16.20	24.64
Oldenburg	8.10	16.28	24.45
Spectral Division	8.17	16.35	24.77
BIRA	7.93	15.74	N/A

Table 6.9: Times of arrival of the echo for a structure of Aluminium-Water with a wideband transducer and a thickness of aluminium of 26 mm

Method	Measured time separation between 1^{st} echo and 2^{nd} echo $t_{expected}$ = 16.46 μs	Relative error (%)
Cross-correlation	17.13	4.07
Oldenburg	16.61	0.94
Spectral Division	16.96	3.04
BIRA	17.69	7.47

Table 6.10: Time separations and relative errors between the first and second echo for a structure of Aluminium-Water with a wideband transducer and a thickness of aluminium of 52 mm

when compared the Spectral Division method and the cross-correlation. BIRA was the less accurate technique with a relative error of 7.47 %.

For a thickness of 26 *mm* of aluminium, the time separation are shown on Table 6.11. The time separations were calculated from the values in Table 6.9. With this thickness of the first layer, the relative error of the three techniques of Cross-correlation, Oldenburg and Spectral Division performed with an accuracy below 1 %. BIRA is the algorithm that is the less accurate with a relative error of 5.1 %.

This Section presented the results of the accuracy of the BIRA to estimate the time of arrival of multiple echoes and the time separation corresponding to the time of travel in the first layer. The relative error to estimate the time separation for the structure of Aluminium-Water is summarised in Table 6.12.

For such a structure, BIRA did not outperform any other techniques except for the case of the narrowband data with a thickness of 26 *mm* of aluminium. This

Method	Measured time separation between 1^{st} echo and 2^{nd} echo $t_{expected} = 8.23\ \mu s$	Relative error (%)
Cross-correlation	8.15	0.97
Oldenburg	8.18	0.61
Spectral Division	8.18	0.61
BIRA	7.81	5.10

Table 6.11: Time separations and relative errors between the first and second echo for a structure of Aluminium-Water with a wideband transducer and a thickness of aluminium of 26 mm

Thickness (mm)	Transducer type	Cross correlation	Oldenburg	Spectral Division	BIRA
52 mm = 2 × λ	narrowband	37.85 %	27.46 %	29.71 %	31.17 %
	wideband	4.07 %	0.91 %	3.04 %	7.47 %
26 mm = λ	narrowband	67.56 %	48.24 %	48.24 %	6.56 %
	wideband	0.97 %	0.61 %	0.61 %	5.1 %

Table 6.12: Summary of relative error of each technique on the measurement of the thickness of the first layer for the structure of Aluminium-Water

result of the BIRA was obtained as the spurious lobe in the BIRA was ignored. For any other cases, BIRA was at the best, as accurate as the cross-correlation.

Moreover, BIRA appeared limited to estimate the time of arrival of more than two echoes as no significant peak values were obtained for the output of the *Spectral block*. As expected from the analysis in Chapter 5, a spurious lobe was also noticed in the signal formed by the BIRA. However, BIRA never had a significant relative error in comparison to the others techniques. To further evaluate the performance, similar simulations were pursued on a structure of Ice-Water.

6.3.1.2.2 Struture of Ice-Water

The second case concerned the structure of Ice-Water as the acoustic characteristics were different from the structure of Aluminium-Water. The first set of simulations was pursued with the narrowband transducer and the structure of Ice-Water where the thickness of the ice was set firstly to $2\lambda = 32\ mm$ and then

Method	1^{st} echo (1) (μs) $t_{expected}$ = 16.08 μs	2^{nd} echo (2) (μs) $t_{expected}$ = 32.16 μs	3^{rd} echo (3) (μs) $t_{expected}$ = 48.24 μs
Cross-correlation	15.62	45.51	N/A
Oldenburg	17.13	33.11	49.22
Spectral Division	15.98	32.09	48.07
BIRA	15.98	31.23	N/A

Table 6.13: Times of arrival of the echoes for a structure of Ice-Water with a narrowband transducer and a thickness of ice of 32 mm

to a thickness of $\lambda = 16\ mm$.

For a thickness of ice of 32 mm, it was expected to observe an echo every 16.08 μs as demonstrated previously. The output of the ultrasonic ranging system is shown on Figure 6.13(a)(b). The cross-correlation estimated the time of arrival of each numbered echo as listed in Table 6.13. For such a thickness, it was expected to obtain peak values at time of 16.08 μs, 32.16 μs, 48.24 μs, etc... The cross-correlation only clearly indicated the time of arrival of the first echo, as shown on Figure 6.13(c). Then the Oldenburg technique estimated the time of arrival of the first three echoes with the times listed in Table 6.13 corresponding to the peak values numbered on Figure 6.13(d). For the case of the Spectral Division technique, the first three echoes were estimated with the introduction of some spurious peaks. For the case of the BIRA, a spurious lobe was introduced between the first and second echo.

For a thickness of ice if $\lambda = 16\ mm$, the performance of the techniques was similar, as shown on Figure 6.14. The cross-correlation method was limited to clearly estimate the time of arrival of the first echo, Figure 6.14(c), whereas the Oldenburg and Spectral Division techniques accurately indicated the first three echoes as illustrated on Figure 6.14(d)(e). The corresponding time values are listed in Table 6.14. Finally the BIRA estimated the time of arrival of the first echo and the second echo when the spurious lobe was ignored, as shown on Figure 6.14(f).

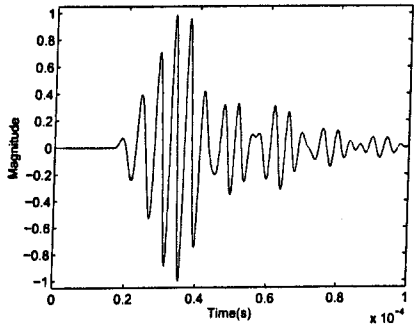

(a) Time response of the ultrasonic ranging system

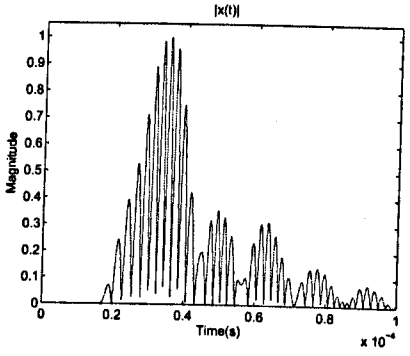

(b) Full wave rectified of the time response of the ultrasonic ranging system

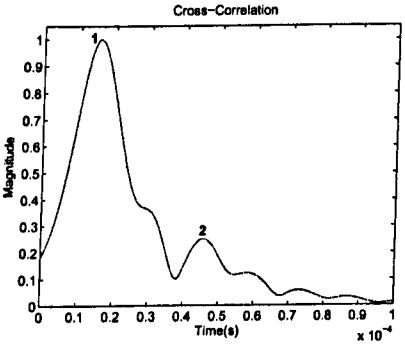

(c) Envelope of the cross-correlation response

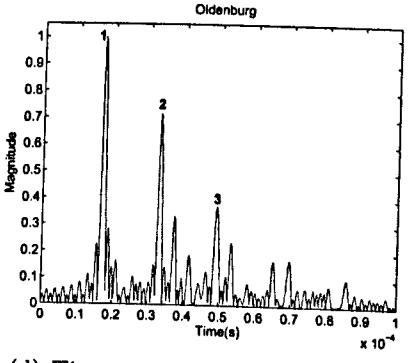

(d) Time response of the Oldenburg

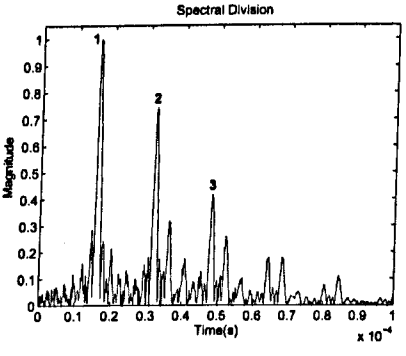

(e) Time response of the Spectral Division

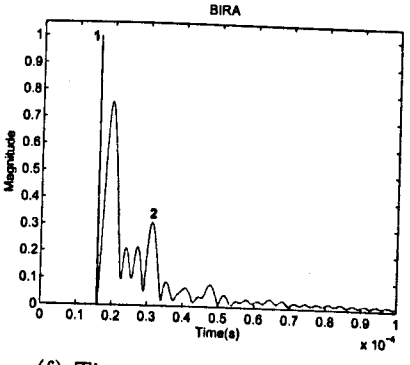

(f) Time response of the BIRA

Figure 6.13: Time responses with narrowband transducer with a structure of Ice-Water and a thickness of ice of 32 mm.

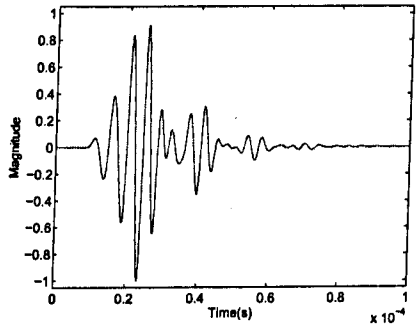

(a) Time response of the ultrasonic ranging system

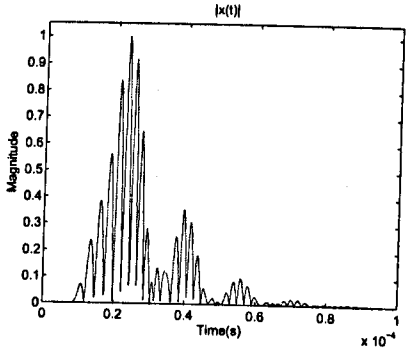

(b) Full wave rectified of the time response of the ultrasonic ranging system

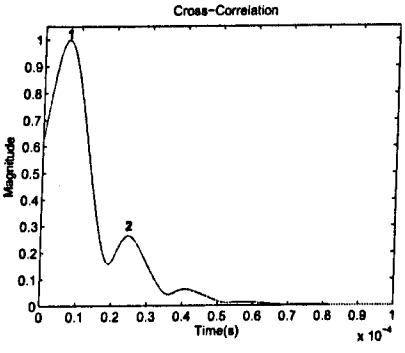

(c) Envelope of the cross-correlation response

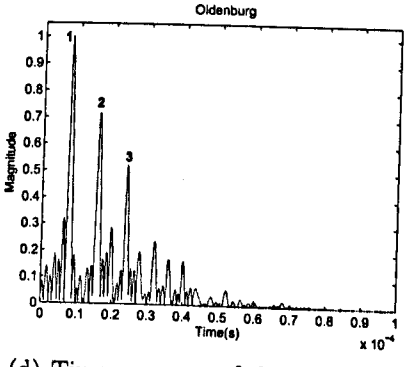

(d) Time response of the Oldenburg

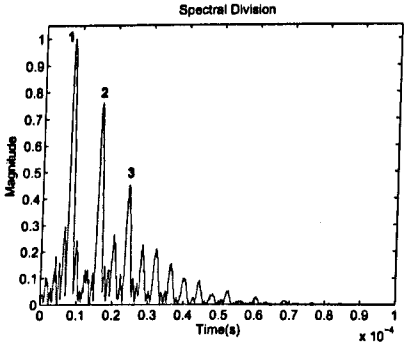

(e) Time response of the Spectral Division

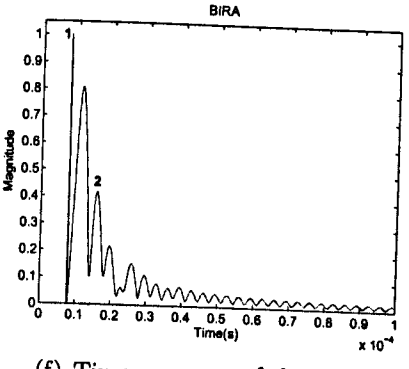

(f) Time response of the BIRA

Figure 6.14: Time responses with narrowband transducer with a structure of Ice-Water and a thickness of ice of 16 mm.

Method	1^{st} echo (1) (μs) $t_{expected}$ = 8.04 μs	2^{nd} echo (2) (μs) $t_{expected}$ = 16.08 μs	3^{rd} echo (3) (μs) $t_{expected}$ = 24.12 μs
Cross-correlation	6.71	24.40	N/A
Oldenburg	7.74	15.91	23.96
Spectral Division	7.93	16.11	24.16
BIRA	7.81	15.74	N/A

Table 6.14: Times of arrival of the echoes for a structure of Ice-Water with a narrowband transducer and a thickness of ice of 16 mm

Method	Measured time separation between 1^{st} echo and 2^{nd} echo $t_{expected}$ = 16.08 μs	Relative error (%)
Cross-correlation	29.89	85.88
Oldenburg	15.98	0.62
Spectral Division	16.11	0.18
BIRA	15.25	5.16

Table 6.15: Time separations and relative errors between the first and second echo for a structure of Ice-Water with a narrowband transducer and a thickness of ice of 32 mm

For these two thicknesses, the time separation for the narrowband data was also quantified. The relative error on the estimated time of arrival for the two thicknesses are shown Table 6.15 and Table 6.16. As the frequency bandwidth was restricted, the cross-correlation did not perform accurately as the second echo was never estimated, leading to a large error value, as shown on Table 6.15 and Table 6.16. BIRA performed as accurately as the deconvolution techniques.

Method	Measured time separation between 1^{st} echo and 2^{nd} echo $t_{expected}$ = 8.04 μs	Relative error (%)
Cross-correlation	17.69	120.02
Oldenburg	8.17	1.62
Spectral Division	8.18	1.74
BIRA	7.93	1.37

Table 6.16: Time separations and relative errors between the first and second echo for a structure of Ice-Water with a narrowband transducer and a thickness of ice of 16 mm

Method	1^{st} echo (1) (μs) $t_{expected}$ = 16.08 μs	2^{nd} echo (2) (μs) $t_{expected}$ = 32.16 μs	3^{rd} echo (3) (μs) $t_{expected}$ = 48.24 μs	4^{th} echo (4) (μs) $t_{expected}$ = 62.32 μs
Cross-correlation	16.11	31.84	47.70	63.68
Oldenburg	16.15	32.01	48.12	64.22
Spectral Division	16.23	32.21	48.07	64.42
BIRA	16.10	31.48	N/A	N/A

Table 6.17: Times of arrival of the echoes for a structure of Ice-Water with a wideband transducer and a thickness of ice of 32 mm

The following case concerned the use of the wideband transducer on the same structure of Ice-Water with the same thicknesses. As previously done, with the increase in bandwidth, the resolution performance of the cross-correlation and the deconvolution techniques were superior to the narrowband case. Figure 6.15 and Figure 6.16 show the two cases with a respective thickness of ice of 32 *mm* and 16 *mm*. For the case of a thickness of ice of 32 *mm*, Figure 6.15, the corresponding time values of the cross-correlation (Figure 6.15(c)), Oldenburg (Figure 6.15(d)) and Spectral Division (Figure 6.15(e)), are shown on Table 6.17. BIRA estimated the time of arrival of the first and second echo at the respective times shown on Figure 6.15(f).

When the thickness of ice was of 16 *mm*, as shown on Figure 6.16, the Oldenburg method (Figure 6.16(d)) and the Spectral Division method (Figure 6.16(e)) appeared to perform better than the cross-correlation technique (Figure 6.16(c)) as the signals were sharper. BIRA still determined the time of arrival of the first and second echo but by ignoring the spurious lobe, as shown on Figure 6.16(f). The time values are shown in Table 6.18.

Again the time separation for the wideband data was quantified. The relative error on the estimated time of arrival for the two thicknesses are shown on Table 6.19 and Table 6.20. With the increase in bandwidth, the accuracy of the techniques significantly improved. BIRA did not outperform the other techniques but the relative error was in the same order as the other methods.

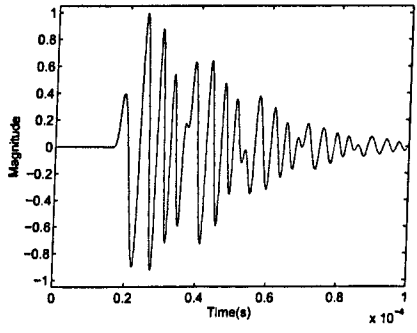

(a) Time response of the ultrasonic ranging system

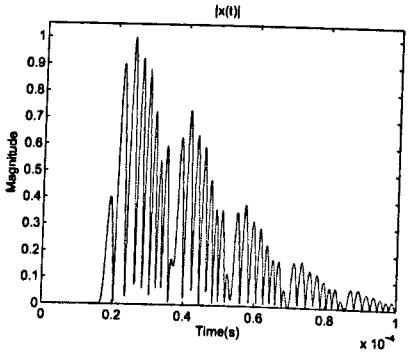

(b) Full wave rectified of the time response of the ultrasonic ranging system

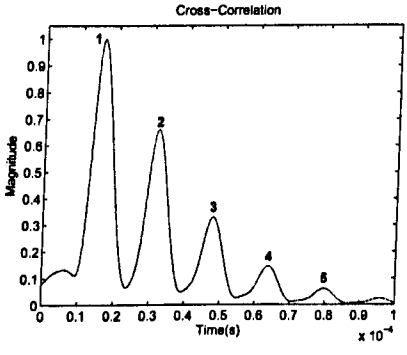

(c) Envelope of the cross-correlation response

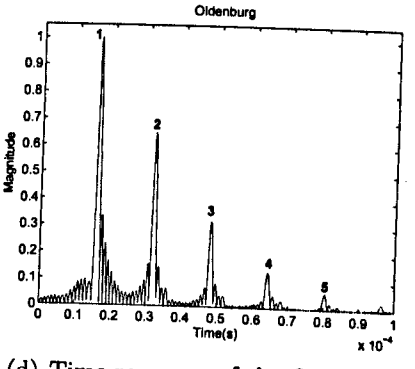

(d) Time response of the Oldenburg

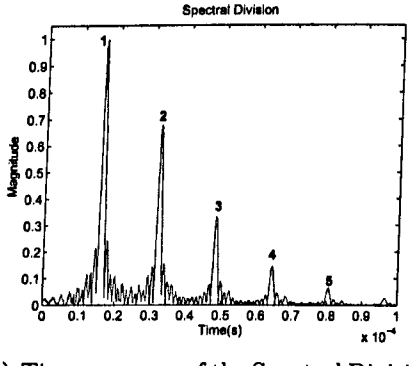

(e) Time response of the Spectral Division

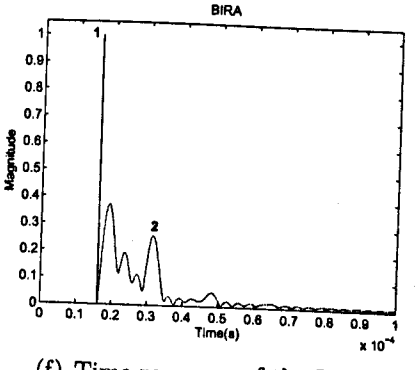

(f) Time response of the BIRA

Figure 6.15: Time responses with wideband transducer with a structure of Ice-Water and a thickness of ice of 32 mm.

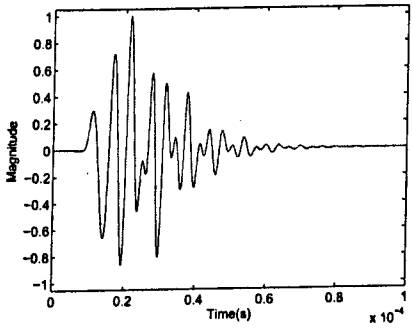

(a) Time response of the ultrasonic ranging system

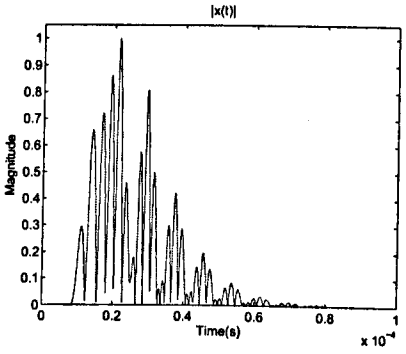

(b) Full wave rectified of the time response of the ultrasonic ranging system

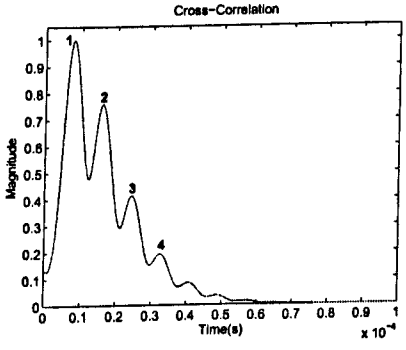

(c) Envelope of the cross-correlation response

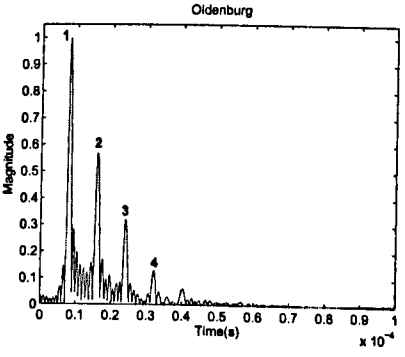

(d) Time response of the Oldenburg

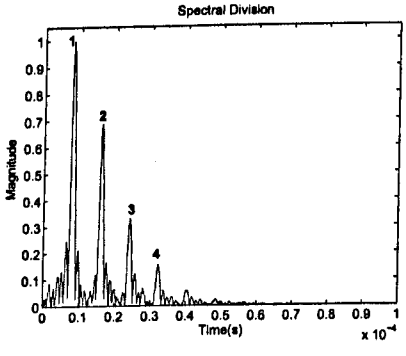

(e) Time response of the Spectral Division

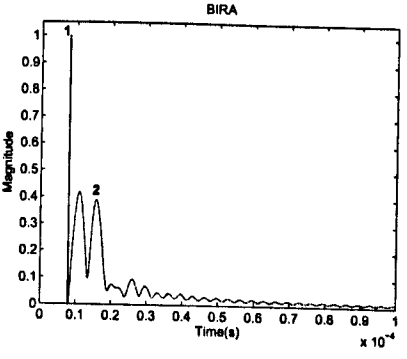

(f) Time response of the BIRA

Figure 6.16: Time responses with wideband transducer with a structure of Ice-Water and a thickness of ice of 16 mm.

Method	1^{st} echo (1) (μs) $t_{expected}$ = 8.04 μs	2^{nd} echo (2) (μs) $t_{expected}$ = 16.08 μs	3^{rd} echo (3) (μs) $t_{expected}$ = 24.12 μs	4^{th} echo (4) (μs) $t_{expected}$ = 32.16 μs
Cross-correlation	7.81	15.98	24.40	32.57
Oldenburg	7.98	16.03	23.96	32.01
Spectral Division	7.93	16.10	24.16	32.21
BIRA	7.93	15.74	N/A	N/A

Table 6.18: Times of arrival of the echoes for a structure of Ice-Water with a wideband transducer and a thickness of ice of 16 mm

Method	Measured time separation between 1^{st} echo and 2^{nd} echo $t_{expected}$ = 16.08 μs	Relative error (%)
Cross-correlation	15.73	2.18
Oldenburg	15.86	1.37
Spectral Division	15.98	0.62
BIRA	15.38	4.35

Table 6.19: Time separations and relative errors between the first and second echo for a structure of Ice-Water with a wideband transducer and a thickness of ice of 32 mm

Method	Measured time separation between 1^{st} echo and 2^{nd} echo $t_{expected}$ = 8.04 μs	Relative error (%)
Cross-correlation	8.17	1.62
Oldenburg	8.05	0.12
Spectral Division	8.17	1.61
BIRA	7.81	2.86

Table 6.20: Time separations and relative errors between the first and second echo for a structure of Ice-Water with a wideband transducer and a thickness of ice of 16 mm

Thickness (mm)	Transducer type	Cross correlation	Oldenburg	Spectral Division	BIRA
32 mm = 2 × λ	narrowband	85.88 %	0.62 %	0.18 %	5.16 %
	wideband	2.18 %	1.37 %	0.62 %	4.35 %
16 mm = λ	narrowband	120.02 %	1.62 %	1.74 %	1.37 %
	wideband	1.62 %	0.12 %	1.61 %	2.86 %

Table 6.21: Summary of relative error of each technique on the measurement of the thickness of the first layer for the structure of Ice-Water

6.3.1.2.3 Conclusion on the axial resolution

The axial resolution performance of the BIRA was compared with alternative techniques. The use of cross-correlation was a good assessor of the axial resolution as it matches the theoretical axial resolution, as it has been demonstrated with these results.

An improvement in axial resolution was gained when deconvolution techniques such as Spectral Division and Oldenburg are implemented, as they led to a sharper image than with the cross-correlation technique. BIRA was shown to perform well to determine the time of arrival of the first echo but appeared to be very limited to estimate any other time of arrival, due to the presence of the spurious lobe in the *Spectral block*. The cause of this spurious lobe is detailed in Chapter 5. BIRA did not overcome the theoretical limit of the axial resolution, set at a wavelength λ, calculated at the centre frequency of the transducer. In most cases, it appeared to be unable to offer any axial resolution improvement for practical engineering applications. The next Section will further evaluate the BIRA in the presence of noise.

6.3.2 Noise robustness

For the purpose of any engineering applications, it was required to evaluate the robustness to noise of the BIRA. The ultrasonic ranging system was used with the wideband transducer and a structure of Ice-Water with a thickness of ice of 32 *mm* to generate the signals for the simulations. As the transducer has a wider bandwidth, it is more sensitive to noise and more suitable to the study of noise robustness of the BIRA. The noise was created with a contaminative Gaussian distribution, added to the signal before being passed through the BIRA, the Oldenburg method, the Spectral Division method and the cross-correlation technique. The robustness to noise for four levels of SNR of 60 dB, 30 dB, 15 dB and -20 dB was quantified. As a reference, the cross-correlation was used as it

Method	1^{st} echo (1) (μs) $t_{expected}$ = 16.08 μs	2^{nd} echo (2) (μs) $t_{expected}$ = 32.16 μs	3^{rd} echo (3) (μs) $t_{expected}$ = 48.24 μs
Cross-correlation	16.1	31.84	47.7
Oldenburg	16.03	32.01	48.12
Spectral Division	16.23	32.21	48.19
BIRA	16.1	31.48	N/A

Table 6.22: Times of arrival of the echoes for a level of SNR of 60 dB

Method	Measured time separation between 1^{st} echo and 2^{nd} echo $t_{expected} = 16.08\ \mu s$	Relative error (%)
Cross-correlation	15.74	2.11
Oldenburg	15.98	0.62
Spectral Division	15.98	0.62
BIRA	15.38	4.35

Table 6.23: Time separations and relative errors between the first and second echo for a level of SNR of 60 dB

is a suitable assessor for noise robustness. It is the optimal technique for a given level of noise. The deconvolution techniques were also used for comparison. The robustness to noise was quantified by comparing the performance of the algorithms to evaluate the time separation of a signal containing multiple echoes generated with the ultrasonic ranging system used in the previous Section.

For a high level of SNR of 60 dB, the outputs from the ultrasonic ranging system were not significantly altered by the noise level, as shown on Figure 6.17(a)(b). The corresponding times of arrival are shown in Table 6.22. When the various techniques were applied to such signals, they all performed well, as the time separations were accurately estimated either for the cross-correlation technique as shown on Figure 6.17(c), the Oldenburg method as illustrated on Figure 6.17(d) and the Spectral Division method as shown on Figure 6.17(e). The relative errors are shown on Table 6.23. The relative error for BIRA was close to the other techniques but it did not outperform the other algorithms.

When the level of SNR was decreased to 30 dB, it can be noticed the intro-

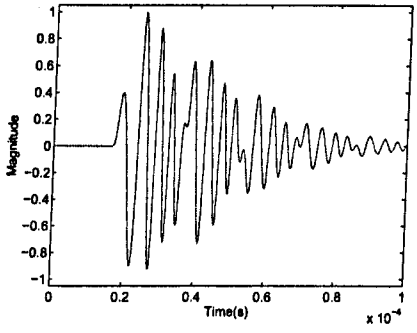

(a) Time response of the ultrasonic ranging system

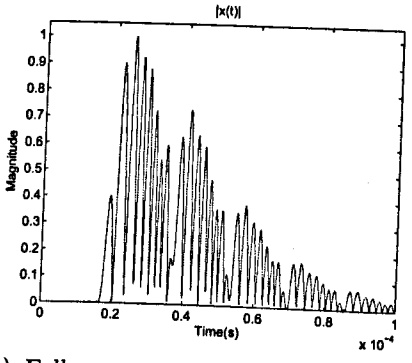

(b) Full wave rectified of the time response of the ultrasonic ranging system

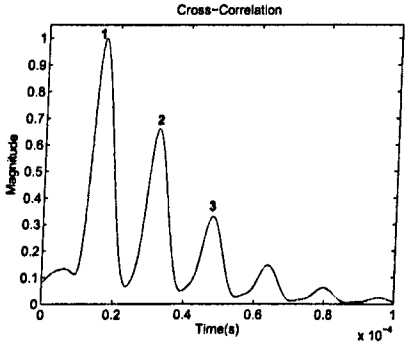

(c) Envelope of the cross-correlation response

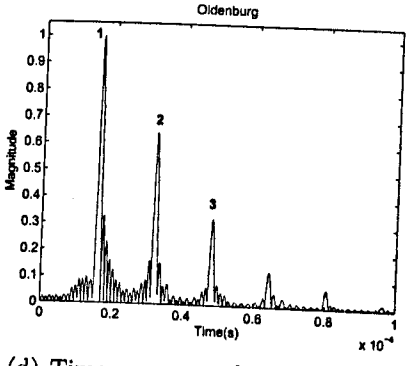

(d) Time response of the Oldenburg

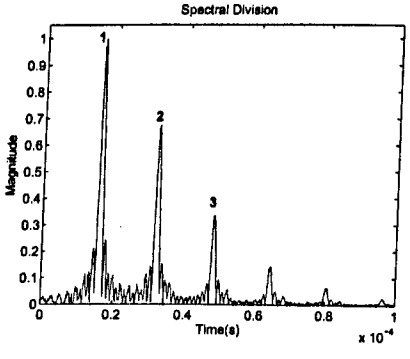

(e) Time response of the Spectral Division

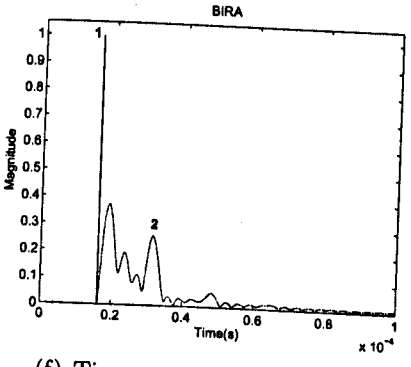

(f) Time response of the BIRA

Figure 6.17: Time responses with wideband transducer with a structure of Ice-Water for a SNR level of 60 dB.

Method	1^{st} echo (1) (μs) $t_{expected}$ = 16.08 μs	2^{nd} echo (2) (μs) $t_{expected}$ = 32.16 μs	3^{rd} echo (3) (μs) $t_{expected}$ = 48.24 μs
Cross-correlation	16.1	31.84	47.7
Oldenburg	16.03	32.01	48.12
Spectral Division	16.23	32.21	48.31
BIRA	16.1	31.35	N/A

Table 6.24: Times of arrival of the echoes for a level of SNR of 30 dB

Method	Measured time separation between 1^{st} echo and 2^{nd} echo $t_{expected}$ = 16.08 μs	Relative error (%)
Cross-correlation	15.74	2.11
Oldenburg	15.98	0.62
Spectral Division	15.98	0.62
BIRA	15.25	5.16

Table 6.25: Time separations and relative errors between the first and second echo for a level of SNR of 30 dB

duction at the start of the signal from the ultrasonic ranging system of a low level of noise signal, as illustrated on Figure 6.18(a)(b). With such a level of SNR, the signal of the cross-correlation technique was unchanged as illustrated on Figure 6.18(c). However, with the deconvolution techniques, it can be noticed that they started to break down as the sharpness of the deconvoled signal was decreased on Figure 6.18(d)(e), when compared to Figure 6.17(d)(e). However, the time of arrival of each echo was preserved as shown from the values in Table 6.24. The relative error on the time separation was similar to the case of a level of SNR of 60 dB, as shown on Table 6.25. The performance of BIRA was not altered for such a level of SNR and performed as well as for a level of SNR of 60 dB (Figure 6.18(f)).

A level of SNR of 15 dB introduced visible changes to the signal created by the ultrasonic ranging system as shown on Figure 6.19(a)(b). With such a level of SNR, the cross-correlation stayed robust, as shown on Figure 6.19(c). BIRA appeared also to be robust to this level of noise, as the signal was not altered

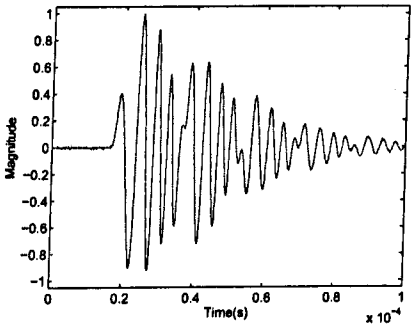

(a) Time response of the ultrasonic ranging system

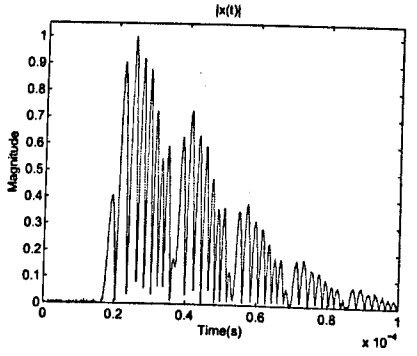

(b) Full wave rectified of the time response of the ultrasonic ranging system

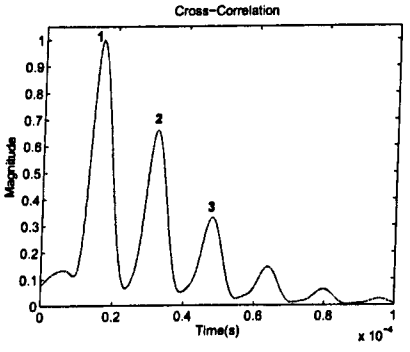

(c) Envelope of the cross-correlation response

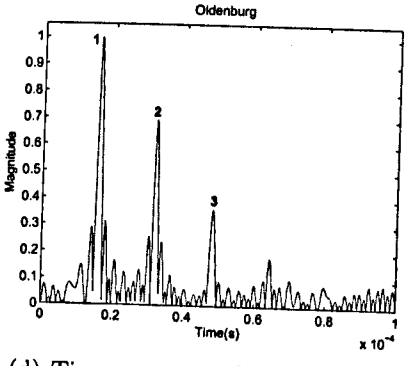

(d) Time response of the Oldenburg

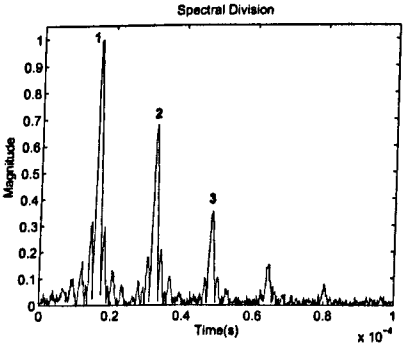

(e) Time response of the Spectral Division

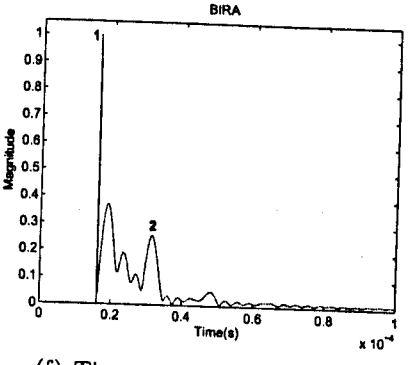

(f) Time response of the BIRA

Figure 6.18: Time responses with wideband transducer with a structure of Ice-Water for a SNR level of 30 dB.

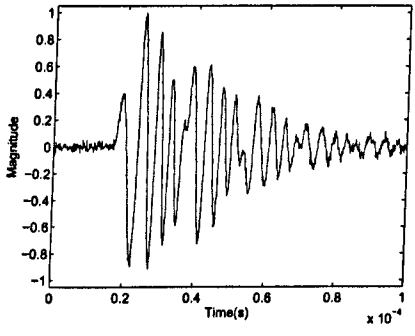

(a) Time response of the ultrasonic ranging system

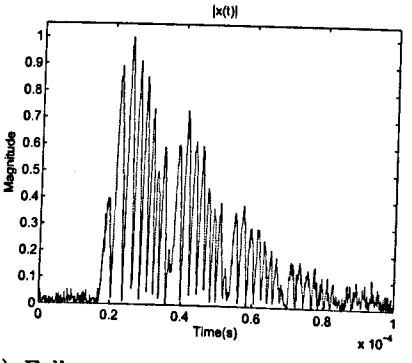

(b) Full wave rectified of the time response of the ultrasonic ranging system

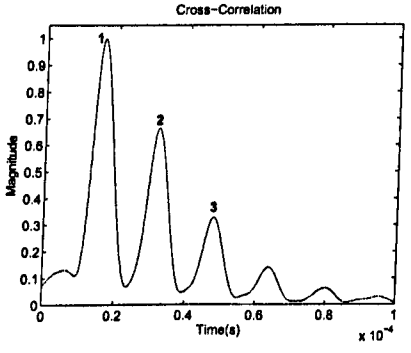

(c) Envelope of the cross-correlation response

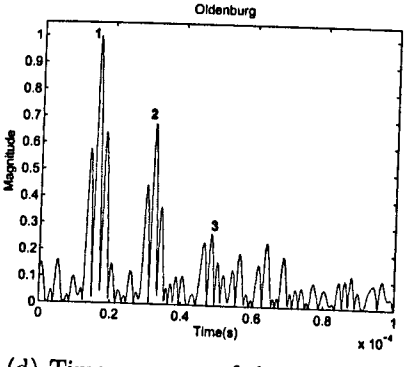

(d) Time response of the Oldenburg

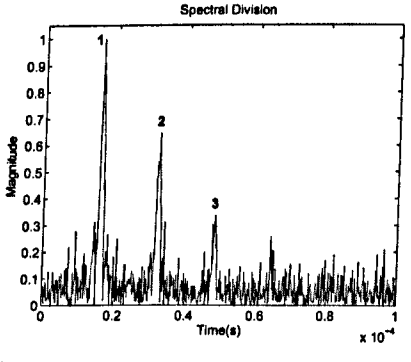

(e) Time response of the Spectral Division

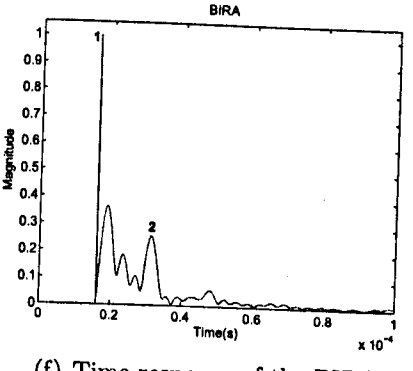

(f) Time response of the BIRA

Figure 6.19: Time responses with wideband transducer with a structure of Ice-Water for a SNR level of 15db.

Method	1^{st} echo (1) (μs) $t_{expected}$ = 16.08 μs	2^{nd} echo (2) (μs) $t_{expected}$ = 32.16 μs	3^{rd} echo (3) (μs) $t_{expected}$ = 48.24 μs
Cross-correlation	16.1	31.84	47.7
Oldenburg	16.15	32.01	48.24
Spectral Division	15.98	32.33	48.19
BIRA	16.1	31.35	N/A

Table 6.26: Times of arrival of the echoes for a level of SNR of 15 dB

Method	Measured time separation between 1^{st} echo and 2^{nd} echo $t_{expected}$ = 16.08 μs	Relative error (%)
Cross-correlation	15.74	2.11
Oldenburg	15.86	1.37
Spectral Division	16.35	1.68
BIRA	15.25	5.16

Table 6.27: Time separations and relative errors between the first and second echo for a level of SNR of 15 dB

Method	1^{st} echo (1) (μs)	Relative error (%)
Cross-correlation	15.73	2.18
BIRA	16.97	5.53

Table 6.28: Times of arrival of the first echo for a level of SNR of -20 dB with the relative error

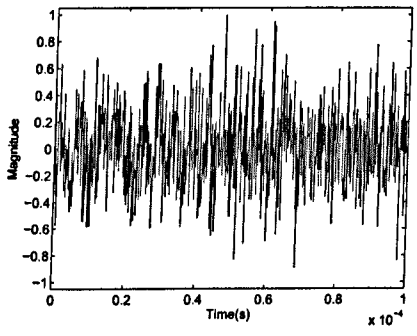

(a) Time response of the ultrasonic ranging system

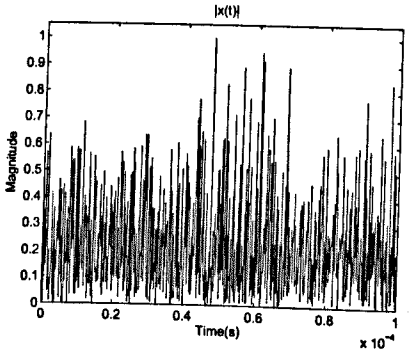

(b) Full wave rectified of the time response of the ultrasonic ranging system

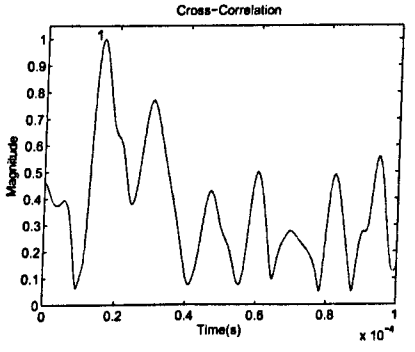

(c) Envelope of the cross-correlation response

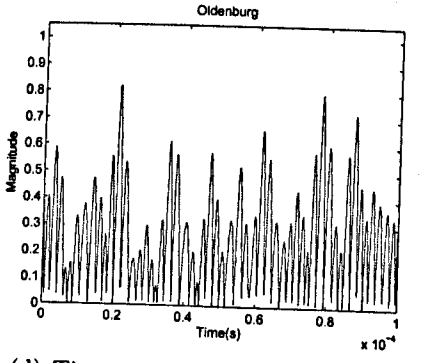

(d) Time response of the Oldenburg

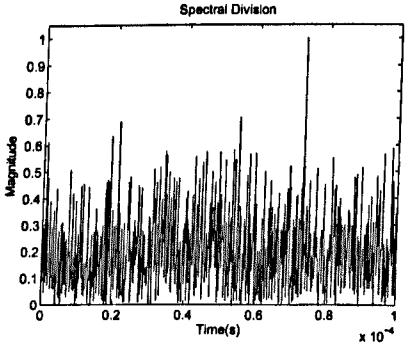

(e) Time response of the Spectral Division

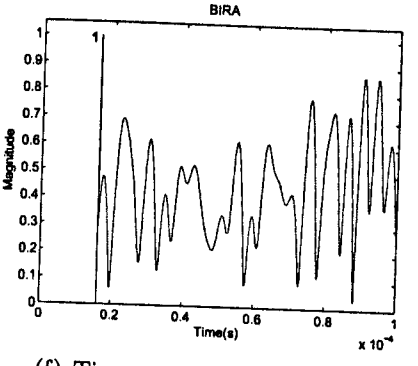

(f) Time response of the BIRA

Figure 6.20: Time responses with wideband transducer with a structure of Ice-Water for a SNR level of -20db.

(Figure 6.19(f)). The measurements of the time of arrival for each technique are shown in Table 6.26. It was also shown that the relative error for the cross-correlation technique and the BIRA stayed at the same level as the level of SNR of 30 dB as shown in Table 6.27. For the deconvolution techniques, it can be noticed a loss in performance as illustrated on Figure 6.19(d)(e). With this level of SNR, the peak values were wider and spurious peak values started to appear when the signals were compared to the higher level of SNR such as illustrated on Figure 6.17(d)(e) or Figure 6.18(d)(e).

Then, the level of SNR was decreased to evaluate the robustness to very high levels of noise. A level of SNR of $-20\ dB$ was reached and the results are shown on Figure 6.20. With such a level of noise, the ultrasonic ranging system signal was buried into the noise level as shown on Figure 6.20(a)(b). The deconvolution techniques did not estimate the time of arrival of any echoes as shown on Figure 6.20(d)(e). However, the cross-correlation stayed robust to the noise level but it was limited to determine the time of arrival of the first echo, as illustrated on Figure 6.20(c). The corresponding times of arrival of arrival are shown in Table 6.28. The signal formed by the BIRA also indicated the time of arrival of the first echo but there was a significant level of sidelobes indicating the breakdown of the technique (Figure 6.20(f)).

When the level of SNR was progressively decreased, the techniques started to broke down. For a higher level of SNR of 60 dB, all the techniques performed well as the relative error was small. Similar performance were obtained for a level of SNR of 30 dB. When the level of SNR was of 15 dB, the deconvolution techniques started to break down as the output signal that were formed lose in sharpness and structural information. However, the relative error to quantify the time separation stayed relatively small as shown in Table 6.27. For the lower level of SNR of -20 dB, the deconvolution techniques broke down as it was not possible to determine the time of arrival of any echo. However, the cross-correlation technique and

BIRA determined the time of arrival of the first echo with a relative error of less than 6 %, as shown in Table 6.28. Therefore, the results presented in that Section indicates that BIRA stayed as robust as the cross-correlation to noise contamination to determine accurately the time of arrival of the first echo. The results support the abilility of the bats to only determine the time of arrival of the first echo instead of forming fine range-profile image.

6.4 Discussions and Conclusions

This Chapter has studied the BIRA in conditions similar to the one encountered in practical engineering applications, by emulating an ultrasonic ranging system creating multiple overlapping echoes. Variation in the transducer frequency response, the medium of propagation and the target structure has been simulated to quantify the performance of the BIRA when compared to relative straightforward deconvolution methods and the cross-correlation technique.

The results have shown that the BIRA performed as accurately as the other techniques to determine the time of arrival of the first echo. The performance was similar to the cross-correlation, which is an optimal receiver for a given level of noise, and also it was as accurate as the Oldenburg and Spectral Division techniques. However, the BIRA failed to separate multiple overlapping echoes as a spurious lobe was introduced in the signal formed by the BIRA that further reduced the discrimination capability. Moreover, even when the spurious lobe was ignored, the discrimination capability did not overcome the other techniques. Therefore no improvement in the axial resolution was obtained. The deconvolution techniques offered better axial resolution, for reasonable levels of noise, than the cross-correlation and the BIRA.

For high level of SNR, BIRA did not outperform the other techniques to determine the time separation between the first and second echo. However, it

was robust to determine the time of arrival of the first echo for significant noise contamination (SNR = -20 dB).

Overall, the BIRA appeared to not be suitable to separate multiple echoes as it was thought to be done by bats, but rather to be robust to only determine the time of arrival of the first echo. Therefore, the results presented here question the ability of the bats to form detailed acoustic range-profile images using similar underlying processes that are implemented in the BIRA. Chapter 7 will discuss in greater detail this conclusion.

Chapter 7

Conclusions and Further Work

7.1 Introduction

The objective of the work presented in this thesis was to develop a novel and original approach for ultrasonic imaging systems by investigating the current knowledge of the bat auditory system. The resulting contributions are:

- The development of the BIRA reproducing the known underlying processes involved in the bat auditory system.
- The evaluation of the performance of the BIRA under conditions met in practical engineering applications.
- The simulation results that support the assertion that bats do not form detailed range-profile images.

First, this thesis provided a review of the current knowledge of the bat echolocation system and the known underlying processes involved in the bat auditory system in Chapter 2. Chapter 3 presented a review of the various modelling approaches to mimic bat behaviour. Chapter 4 introduced the new BIRA and standard deconvolution techniques designed to improve the axial resolution. Chapter 5 evaluated the performance of the BIRA. Finally, Chapter 6 quantified the performance of the BIRA in a practical engineering applications environment and compared the performance with more conventional signal processing methods.

7.2 Achievements

The work presented here has been successful in investigating areas of biology, signal processing and ultrasound to create an innovative biologically inspired imaging technique for ultrasonic applications.

The first contribution was the development of a biologically inspired imaging technique, named BIRA, derived from studies of the bat auditory system. It iden-

tified the underlying processes involved in the bat auditory system and developed modelling techniques to mimic them.

The second contribution is in the design of a simulation environment to quantify the performance in similar conditions met in practical engineering applications and also by the bats when hunting for flying prey. It highlighted the limitations of the BIRA and demonstrated the reasons for the loss in performance.

The main contribution of this work was to question the ability of bat to form a detailed acoustic range-profile image. This concept was developed from the work by [Simmons, 1989] and based on the experiment of [Simmons et al., 1998]. The results presented in this thesis demonstrate or suggest that the current way of modelling the bat auditory system fails to reconstruct fine range-profile imaging because of the limited information contained in the frequency domain necessary to an efficient way of reforming image with the *Spectral block*. When the BIRA was implemented in similar conditions met by the bats, i.e. considering the influence of air attenuation, the BIRA failed to form a detailed range-profile image and also introduced spurious sidelobes that impaired the resolution discrimination. If bats do use similar techniques than in the BIRA, they will have to cope with such conditions and therefore may be limited in their ability to form detailed range-profile images, to identify an insect in their surroundings. Moreover, the echo returned by a flying insect has been shown to be really complex, containing information on the size and the type of the insect [Kober and Schintzler, 1990]. Bats may detect other effects occurring in the returned echo to identify an insect, such as the wing flutter [Bell and Fenton, 1984]. With a straightforward fluttering model, [Bell and Fenton, 1984] showed that the echolocation calls used by the bats can identify a fluttering object from a standing one. Passive listening has also been shown to be used by the bats to detect a fluttering moth [Anderson and Racey, 1993]. All of these processes may be sufficient for the bats to identify an insect without requiring to form detailed range-profile images. From the results

presented in that thesis, it is believed that bats do not form detailed range-profile using BIRA techniques.

However the techniques in the BIRA offer the significant advantage of being extremely robust for determination of the time of arrival of the first echo, with performance similar to that achieved through cross-correlation. It is of specific interest to highlight the fact that such performance was achieved with the BIRA without any a-priori knowledge on the emitter/receiver device being used, whereas the deconvolution techniques did require such information. Therefore, it is versatile and straightforward to implement for such task in any practical engineering applications. It is especially advantagous when parallel processing is implemented.

7.3 Future Work

The study of the animal kingdom could provide many new concepts for the design of improved imaging systems. The work in this thesis has only covered the aspect of fine resolution, however bats are using complex acoustic signals.

The first work of interest is to study the advantage of the echolocation calls used by the bats. This problem can be analysed in two distinctive parts. The first one concerns the nature of the signal used by the bats and the advantages of such signals, as bats are using non-linear chirp signals. The second aspect concerns the presence of harmonic components in the signal used by bats. Those two aspects are of great interest for ultrasonic applications as current systems do not use signals with such harmonic complexity.

Concerning the nature of the chirp signal used by bats, it has been demonstrated that the non-linearity offers Doppler tolerance properties [Altes and Titlebaum, 1970] [Altes, 1995] that could be used where Doppler Effect has to be ignored. An analysis of the advantages of using non-linear chirp signals for ultrasonic applications may be of interest [Masters et al., 1991]. The use of non-linear

chirp signal has already demonstrated to have wide range of applications [Hossack, 2005].

The harmonic components in the bat echolocation calls are too important to be ignored by the bats; it would be of interest to understand what the advantages of harmonic components are. The bats may perform multiple measurements with a single call by extracting different type of information from each harmonic. All current systems used in SONAR, biomedecine and Non Destructive Evaluation (NDE) only use a single chirp without significant harmonic content. Combining a set of chirp signals could be used to realise multiple measurements simultaneously, such as Doppler shift evaluation and range estimation, for example by combining a LFM chirp for range estimation and CF component for Doppler shift measurement. The use of combined chirp signals has already shown possible practical applications, such as in Doppler measurement by using a combination of LFM chirp signal [Iwashita et al., 2003].

For the development of engineering systems, the study of the bat auditory system and the neuron processes is of significant interest. The bat brain is of a small size and contains hundreds millions of neurons [Horiuchi, 2005]. This is a relatively small number to accomplish their tasks of identifying and catching a prey. The size of their processing unit and the underlying processes are of interest for the design of new hardware and software processing system for practical applications.

Current imaging systems use a straightforward LFM chirp signals that are not altered over a sequence of emissions. Bats change their acoustic emission depending on the task that they want to achieve, for either detecting a prey or catching it. The adaptation of their emission may be of interest for imaging systems with a similar methodology to optimise the signal used to improve the performance.

Finally, the ear of a bat has an important role in the bat echolocation system.

It has been shown that the tragus and the pinna, as shown on Figure 2.7, interact with the incident acoustic waves. The connection between the angle of incidence of an acoustic wave and the modifications occurring in the ear because of the tragus and pinna have been demonstrated [Wotton et al., 1996] and modelled [Matsuo et al., 2001]. It may have an interest for the design of transducer and beamforming techniques. By adding an elevation dependent module on the front face on a transducer, it would be possible to identify the angle of incidence of a wave with a single element rather than with using an array.

Bibliography

Altes, R. A. (1995). Signal processing for target recognition in biosonar. *Neural Networks*, 8(7-8):1275–1295.

Altes, R. A. and Titlebaum, E. L. (1970). Bat signals as optimally doppler tolerant waveforms. *J. Acoust. Soc. Am.*, 48(4B):1014–1020.

Altringham, J. D. (1996). *Bats.* Harvard University Press.

Anderson, M. E. and Racey, P. A. (1993). Discrimination between fluttering and non-fluttering moths by brown long-eared bats, plecotus auritus. *Animal Behaviour*, 46(6):1151–1155.

Au, W. W. (2004). Echolocation signals of wild dolphins. *Acoustical Physics*, 50(4):454–462.

Barton, D. K. (1997). *Radar technology encyclopedia.* Artech House, Boston.

Bass, H. E., Sutherland, L. C., and Evans, L. (1972). Atmospheric absorption of sound: Theoretical predictions. *J. Acoust. Soc. Am.*, 51(5B):1565–1572.

Bell, G. P. and Fenton, M. B. (1984). The use of doppler-shifted echoes as a flutter detection and clutter rejection system: the echolocation and feeding behavior of hipposideros ruber (chiroptera: Hipposideridae). *Behavioral Ecology and Sociobiology*, 15(2):109–114.

Benny, G. and Hayward, G. (2000). Beam profile measurements and simulations for ultrasonic transducers operating in air. *J. Acoust. Soc. Am.*, 107(4):2089–2100.

Boonman, A. M., Parsons, S., and Jones, G. (2003). The influence of flight speed on the ranging performance of bats using frequency modulated echolocation pulses. *J. Acoust. Soc. Am.*, 113(1):613–628.

Carmena, J. M. and Hallam, J. C. T. (2000). Estimating doppler shift with a coarse cochlear filterbank. In *Intelligent Robots and Systems, 2000. (IROS 2000). Proceedings. 2000 IEEE/RSJ International Conference on*, volume 1, pages 221–226.

Cheely, M. and Horiuchi, T. (2003). A vlsi model of range-tuned neurons in the bat echolocation system. *ISCAS'03 Proceeding of the 2003 International Symposium on Circuits and Systems*, 4:872–875.

Chittajallu, S. K., Palakal, M., and Kohrt, K. (1994). Computational model of signal-encoding in the mammalian peripheral auditory system. In *Systems, Man, and Cybernetics, 1994. 'Humans, Information and Technology'., 1994 IEEE International Conference on*, volume 2, pages 1303–1307.

Dawson, S. M. (1991). Clicks and communication - the behavioral and social contexts of hector dolphin vocalizations. *Ethology*, 88(4):265–276.

Dror, I. E., Zagaeski, M., and Moss, C. E. (1995). Three-dimensional target recognition via sonar: A neural network model. *Neural Networks*, 8(1):149–160.

Dubrovsky, N. A. (2004). Echolocation system of the bottlenose dolphin. *Acoustical Physics*, 50(3):305–317.

Erwin, H. R., Wilson, W. W., and Moss, C. F. (2001). A computational sensorimotor model of bat echolocation. *J. Acoust. Soc. Am.*, 110(3):1176–1187.

Feng, A. S., Condon, C. J., and White, K. R. (1994). Stroboscopic hearing as a mechanism for prey discrimination in frequency-modulated bats. *J. Acoust. Soc. Am.*, 95(5):2736–2744.

Fenton, M. B. (1984). Echolocation - implications for ecology and evolution of bats. *Quarterly Review of Biology*, 59(1):33–53.

Fenton, M. B. (1995). *Natural history and biosonar signals in "Hearing by bats"*. Springer-Verlag.

Fiorillo, A. S. and D'Angelo, G. (2002). Echo signals processing with neural network in bat-like sonars based on pvdf. In *Ultrasonics Symposium, 2002. Proceedings. 2002 IEEE*, volume 1, pages 781–784.

Griffin, D. R. (1958). *Listening in the dark: The acoustic orientation of bats and men.* New Haven : Yale University Press.

Grossetete, A. and Moss, C. (1998). Target flutter rate discrimination by bats using frequency-modulated sonar sounds: Behavior and signal processing models. *J. Acoust. Soc. Am.*, 103(4):2167–2176.

Grunwald, J., Schornich, S., and Wiegrebe, L. (2005). Classification of natural textures in echolocation. *PNAS*, 101(15):5670–5674.

Heffner, R. S. and Koay, G. (2001). Audiograms of five species of rodents: implications for the evolution of hearing and the perception of pitch. *Hearing Research*, 157(1-2):138–152.

Hickling, R. and Brown, R. L. (2002). Acoustic communication by ants. *J. Acoust. Soc. Am.*, 112(5):2336–2336.

Hill, J. E. and Smith, J. D. (1984). *Bats-A natural history.* University of Texas Press, Austin.

Holy, T. E. and Guo, Z. (2005). Ultrasonic songs of male mice. *Public Library of Science Biology*, 3(12):2177–2186.

Horiuchi, T. and Hynna, K. (2001). Spike-based modeling of the ild system in the echolocating bat. *Neural Networks*, 14:755–762.

Horiuchi, T. K. (2005). "seeing" in the dark: Neuromorphic vlsi modeling of bat echolocation. *IEEE Signal Processing Magazine*, pages 134–139.

Hossack, J. A. (2005). Introduction to the special issue on coded waveforms. *IEEE Trans. Ultrason. Ferroelec. Freq. Cont.*, 52(2):158–159.

Ifukube, T., Sasaki, T., and Peng, C. (1991). A blind mobility aid modeled after echolocation of bats. *IEEE Transactions on Biomedical Engineering*, 38(5):461–465.

Inoue, S., Kimyou, M., Kashimori, Y., and Kambara, T. (1999). A neural mechanism for detecting target distance independently of target velocity in echolocation of bat. In IEEE, editor, *6th International Conference on Neural Information Processing*, volume 2, pages 477–482.

Iwashita, K., Moriya, T., and ans M. Yoshizawa, N. T. (2003). Doppler measurement using a pair of fm-chirp signals. *IEEE Ultrasonics Symposium*, 2:1219–1222.

Koay, G., Heffner, H. E., and Heffner, R. S. (1997). Audiogram of the big brown bat(eptisucus fuscus). *Hearing Research*, 105(3):202–210.

Kober, R. and Schintzler, H. (1990). Information in sonar echoes of fluttering insects available for echolocations bats. *J. Acoust. Soc. Am.*, 87(2):882–896.

Krautkramer, J. and Krautkramer, H. (1990). *Ultrasonic Testing of Materials.* Springer-Verlag, 4th fullly revised edition edition.

Kroodsma (1983). *Acoustic Communication in Birds.* Academic Press.

Kuc, R. (1993). Three dimensional tracking using qualitative sonar. *Robotics and Autonomous Systems*, 11:213–219.

Kuc, R. (1994). Sensorimotor model of bat echolocation and prey capture. *J. Acoust. Soc. Am.*, 96(4):1965–1978.

Kuc, R. (1997). Biomimetic sonar recognizes objects using binaural information. *J. Acoust. Soc. Am.*, 102(2):689–696.

Lewis, J. E. (1987). *A study of the one-dimensional inverse problem in ultrasonic systems.* PhD thesis, University of Strathclyde, Department of Electrical and Electronic Engineering, Andersonian Library.

Lin, Z. B., Chittajallu, S. K., Kayalar, S., Wong, D., and Yurtseven, H. O. (1991). Modeling constant best delay-sensitive neurons and tracking neurons in the auditory cortex of the fm bat with a back-propagation neural network. In *IEEE Conference on Neural Networks for Ocean Engineering*, pages 123–132.

Masters, W. M., Jacobs, S. C., and Simmons, J. A. (1991). The structure of echolocation sounds by big brown bat eptesicus fuscus: Some consequences for echo processing. *J. Acoust. Soc. Am.*, 89(3):1402–1413.

Matsuo, I., Kunugiyama, K., and Yano, M. (2004). An echolocation model for range discrimination of multiple closely spaced objects: Transformation of spectrogram into reflected intensity distribution. *J. Acoust. Soc. Am.*, 115(2):920–928.

Matsuo, I., Tani, J., and Yano, M. (2001). A model of echolocation of multiple targets in 3d space from a single emission. *J. Acoust. Soc. Am.*, 110(1):607–624.

Matsuo, I. and Yano, M. (2004). An echolocation model for the restoration of an echolocation of an acoustic image from a single-emission echo. *J. Acoust. Soc. Am.*, 116(6):3782–3788.

Mergell, P., Fitch, W. T., and Herzel, H. (1999). Modeling the role of nonhuman vocal membranes in phonation. *J. Acoust. Soc. Am.*, 105:2020–2028.

Miller, L. A. and Pedersen, S. B. (1988). *Animal Sonar: Processes and performance*, chapter Echoes from insects processed using Time Delayed Spectrometry (TDS), pages 803–807. Plenum, New York.

Moss, C. F. and Surlykke, A. (2001). Auditory scene analysis by echolocation in bats. *The Journal of the Acoustical Society of America*, 110(4):2207–2226.

Muller, R. (2001). A synthetic biosonar-observer. In Elsner, N. and Kreutzberg, G. W., editors, *IEEE International Conference on Robotics and Automation*, volume II, page 1040. IEEE.

Oppenheim, A. V. and Schafer, R. W. (1989). *Discrete-Time Signal Processing.* Prentice-Hall.

Peremans, H. and Hallam, J. (1998). The spectrogram correlation and transformation receiver, revisited. *J. Acoust. Soc. Am.*, 104(2):1101–1110.

Peremans, H. and Muller, R. (2003). A comprehensive robotic model for neural & acoustic signal processing in bats. In *Neural Engineering, 2003. Conference Proceedings. First International IEEE EMBS Conference on*, pages 458–461.

Peremans, H., Walker, V. A., and Hallam, J. C. T. (1998). 3d object localisation with a binaural sonarhead, inspirations from biology. *IEEE International Conference on Robotics and Automation*, 4:2795–2800.

Popper, A. N. and Fay, R. R., editors (1995). *Hearing by bats*, volume 5 of *Springer Handbook of Auditory Research.* New York ; London : Springer-Verlag.

Reese, S. S. and Kenney, J. B. (1994). Ultra-high resolution, biologically inspired sonar. In *Autonomous Underwater Vehicle Technology, 1994. AUV '94., Proceedings of the 1994 Symposium on*, pages 456–461.

Saillant, P. A., Simmons, J. A., Dear, P., and McMullen, T. A. (1993). A computational model of echo processing and acoustic imaging in frequency-modulated echolocating bats: The spectrogram correlation and transformation receiver. *J. Acoust. Soc. Am.*, 94(5):2691–2712.

Schmidt, S. (1988). Evidence for a spectral basis of texture perception in bat sonar. *Nature*, 331(18):617–619.

Schmidt, S. (1992). Perception of structured phantom targets in the echolocating bat, megaderma lyra. *J. Acoust. Soc. Am.*, 91(4):2203–2223.

Selesnick, I. W. and Burrus, C. S. (1998). Generalized digital butterworth filter design. *IEEE Transactions on Signal Processing [see also Acoustics, Speech, and Signal Processing]*, 46(6):1688–1694.

Shi, R. Z. and Horiuchi, T. K. (2004). A vlsi model of the bat lateral superior olive for azimuthal echolocation. *ISCAS'04 Proceeding of the 2004 International Symposium on Circuits and Systems*, 4:900–9003.

Shi, R. Z. and Horiuchi, T. K. (2005). A vlsi model of the bat dorsal nucleus of the lateral lemniscus for azimuthal echolocation. *ISCAS'05 Proceeding of the 2005 International Symposium on Circuits and Systems*, 5:4217–4220.

Simmons, J. A. (1973). The resolution of target range by echolocating bats. *J. Acoust. Soc. Am.*, 54:157–173.

Simmons, J. A. (1989). A view of the world through the bat's ear: The formation of acoustic images in echolocation. *Cognition*, 33:155–199.

Simmons, J. A. and Chen, L. (1989). The acoustic basis for target discrimination by fm echolocating bats. *J. Acoust. Soc. Am.*, 86:1333–1350.

Simmons, J. A., Ferragamo, M. J., and Moss, C. F. (1998). Echo-delay resolution in sonar images of the big brown bat, eptesicus fuscus. *Proc. Natl. Acad. Sci. U.S.A.*, 95:12647–12652.

Streicher, A., Muller, R., Peremans, H., and Lerch, R. (2003). Broadband ultrasonic transducer for a artificial bat head. In *Ultrasonics, 2003 IEEE Symposium on*, volume 2, pages 1364–1367.

Suga, N. (1984). *Dynaminc Aspects of Neocortical Function*, chapter The extend to which biosonar information is represented in the bat auditory cortex. John Wiley Sons.

Suga, N. (1990). Biosonar and neural computation in bats. *Scientific American*, pages 34–41.

Suga, N. and Ma, X. (2003). Multiparametric corticofugal modulation and plasticity in the auditory system. *Nature Reviews, Neuroscience*, 4:783–793.

Suthers, R. A. (2004). Vocal mechanisms in birds and bats: a comparative view. *Anais da Academia Brasileira de Cincias*, 76(2):247–252.

Wotton, J. M., Haresign, T., Ferragamo, M. J., and Simmons, J. A. (1996). Sound source elevation and external ear cues influence the discrimination of spectral notches by the big brown bat, eptesicus fuscus. *J. Acoust. Soc. Am.*, 100(3):1764–1776.

Wotton, J. M., Haresign, T., and Simmons, J. A. (1995). Spatially dependent acoustic cues generated by the external ear of the big brown bat, eptesicus fuscus. *J. Acoust. Soc. Am.*, 98(3):1423–1445.

Wotton, J. M. and Simmons, J. A. (2000). Spectral cues and perception of the vertical position of targets by the big brown bat, eptesicus fuscus. *J. Acoust. Soc. Am.*, 107(2):1034–1041.